UNIVERSIDADE DE LISBOA
FACULDADE DE CIÊNCIAS
DEPARTAMENTO DE BIOLOGIA ANIMAL

Assessing gut precursors asymmetric cell behaviours in the zebrafish embryo

Catarina Marta Gonçalves Bota

Mestrado em Biologia Evolutiva e do Desenvolvimento

Dissertação orientada por:
Susana Lopes | Chronic Diseases Research Centre, Universidade Nova de Lisboa
Gabriela Rodrigues | Faculdade de Ciências da Universidade de Lisboa

2018

Acknowledgements

Em primeiro lugar, o meu agradecimento é destinado aos meus orientadores Susana Lopes e Gabriel Martins (que não pode aparecer na capa, burocracias...), que me apoiaram ao longo de todo este processo. À Susana pela oportunidade de participar neste projeto e partilhar comigo o seu contagiante interesse por este estudo, por sempre me desafiar a estabelecer novas metas, por ouvir as minhas dúvidas e apoiar as minhas sugestões. Ao Gabriel por me ter recebido e deixado 'acampar' na microscopia, por tudo o que me ensinou nesta área, pela constante boa disposição e contagiante entusiasmo ao ajudar-me a encontrar soluções para todos os problemas que lhe apresentava, mesmo que às vezes tivesse de pensar em metodologias mais 'alternativas' e por todos os conselhos que partilhou.

O meu mais sincero agradecimento aos dois por terem confiado no meu trabalho, pela paciência e disponibilidade que sempre demonstraram e principalmente por todo o conhecimento que partilharam comigo!

Agradeço também à professora Gabriela Rodrigues, enquanto orientadora interna e por ser uma excelente professora. Mesmo que no início eu tenha revelado alguma teimosia em relação à embriologia, aqui estou eu a estudar embriões de peixe-zebra!

Tenho também a agradecer a todo o grupo Cilia Regulation and Disease lab, a Raquel, o Pedro, a Mónica, a Sara, a Inês, a Margarida e o Filipe. Que sempre estiveram dispostos a ajudar-me com qualquer dúvida, pelas críticas sempre construtivas que me ajudaram a olhar para este trabalho de uma forma mais meticulosa e pelo convívio às segundas-feiras.

Agradeço a todas as pessoas que me ajudaram no IGC, em particular a Cristina Borges que no início foi quase mais uma orientadora e me ajudou nos primeiros passos no IGC e sempre esteve disponível para quaisquer dúvidas e demonstrou um grande interesse pelos progressos do meu trabalho. Agradeço também aos membros da fish facility que sempre estiveram prontas a ajudar-me com quaisquer problemas e dúvidas. Sem esquecer o Nuno Pimpão Martins e o Hugo Pereira da microscopia que estiveram sempre dispostos a ajudar-me com qualquer questão e a esclarecer dúvidas, em particular agradeço ao Nuno pela macro do ImageJ que fez para o meu trabalho.

A todos os meus amigos que estiveram presentes, mesmo que de uma 'maneira digital', obrigada pelo apoio! Em especial aos pollitos, que mesmo longe, estavam à distância de uma mensagem amiga ou para discutir problemas nos nossos trabalhos. Sem esquecer a Joana, que sempre acompanhou esta tese com todo o interesse, e ainda contribuiu com as suas *skills* de engenheira ao ajudar-me a escrever um script em MATLAB que foi crucial no meu trabalho.

Um especial agradecimento vai para o Daniel, por toda a paciência e vontade em ajudar mesmo nas mais pequenas situações que fizeram toda a diferença. Obrigada por tudo!

Em último lugar, o meu agradecimento vai para os meus pais, Paula e Rogério, que foram a base para todo o meu percurso. Obrigada por todo o apoio incondicional nas minhas escolhas e por me terem ouvido e motivado sempre que o caminho se tornou mais difícil.

Resumo

Externamente, o corpo dos vertebrados é simétrico bilateralmente, no entanto, órgãos como o coração, intestino, pâncreas e fígado, pulmões e a vasculatura apresentam uma assimetria relativamente ao eixo Esquerda-Direita (ED), no que diz respeito ao seu posicionamento e/ou morfologia, numa disposição conservada denominada de *situs solitus*. O estabelecimento do eixo ED ocorre durante a embriogénese num processo coordenado após o estabelecimento dos eixos Antero-Posterior (AP) e Dorso-Ventral (DV). Quando ocorrem anomalias durante o estabelecimento do eixo ED, vários quadros clínicos afetando a posição e morfologia destes órgãos podem surgir. Tais casos incluem *situs inversus,* que corresponde a uma completa inversão na disposição dos mesmos, ou heterotaxia, um espectro descrito por vários possíveis desarranjos no posicionamento, em que alguns órgãos podem apresentar normal assimetria ED e outros não.

Nos vertebrados, a assimetria é estabelecida com a expressão assimétrica de Nodal, uma proteína da família TGFβ, do lado esquerdo da placa mesodérmica lateral (PML). O conhecimento atual demonstra que esta quebra na simetria, na maioria dos vertebrados, ocorre numa estrutura chamada de organizador ED, dotada de cílios móveis que promovem um fluxo assimétrico do fluido que enche esta cavidade, impulsando a quebra da simetria. No peixe-zebra, este organizador é a vesícula de Kupffer (KV), formada a partir de um grupo de células localizadas numa zona adjacente ao escudo embrionário, as *dorsal forerunner cells*. Durante o processo de formação, esta estrutura sofre vários rearranjos, apresentando no final uma distribuição dos cílios assimétrica, com uma maior densidade na região antero-dorsal. Esta arquitetura produz um fluxo no sentido anti-horário que promove o aumento de Ca^{2+} intracelular nas células mais à esquerda na KV, via mecanismos envolvendo o complexo Pkd1l1-Pkd2 e a CaMK-II.

Em peixe zebra há três ligandos Nodal, Cyclops, Squint e Southpaw. Southpaw (Spaw) é o ligando Nodal envolvido na quebra e transmissão de assimetria ED no peixe-zebra. A expressão de *southpaw* (*spaw*) apresenta uma forma bilateralmente simétrica em torno da KV aos 4-6 sómitos (ss). Por volta dos 10-12 ss, a expressão de *spaw* torna-se assimétrica na PML do lado esquerdo. Pensa-se que Dand5, uma proteína da família DAN, possa estar ativamente envolvida na formação da assimetria de *spaw* na PML. Aos 8 ss, *dand5* apresenta uma expressão assimétrica, dependente do fluxo, mais forte do lado direito, sendo o primeiro gene assimétrico na KV. Como antagonista de Spaw, Dand5 liga-se a Spaw alegadamente mais no lado direito da KV, postulando-se que promove assim que Spaw difunda da região perto da KV em direção ao lado esquerdo da PML para lá estimular a expressão de *spaw* mRNA. Através de um feedback positivo, a sua expressão é amplificada na PML até aos 22 ss. Spaw também estimula a expressão de *pitx2* no lado esquerdo da PML por volta dos 13 ss, e embora a sua expressão seja dependente da sinalização Nodal, em peixe zebra foi demonstrado que Pitx2 não é necessário para normal lateralização do coração e órgãos digestivos como no ratinho e outros vertebrados. Foi então sugerido que um outro gene, *elovl6*, expresso também no lado esquerdo da PML poderá estar envolvido no estabelecimento da assimetria dos referidos órgãos em peixe zebra. Adicionalmente, Spaw também vai levar à ativação dos seus próprios reguladores negativos, os genes *lefty1 e lefty2,* ficando estes restringidos à linha mediana e lado esquerdo do campo do coração, respetivamente.

Adicionalmente à mesoderme, o ligando Nodal também afeta o processo de especificação e desenvolvimento da endoderme. Este envolve uma complexa e sucessiva interação de vias de sinalização e fatores de transcrição. A endoderme sofre complexos processos morfogenéticos, primeiro após a gastrulação, converge em torno da linha mediana cobrindo todo o eixo AP. O primórdio do tubo

digestivo é formado pelo rearranjo das células precursoras, que polarizam e formam um lúmen por volta das 20 horas pós-fertilização (hpf) que se estende até às 42 hpf. Este tubo dará origem aos órgãos como o fígado, pâncreas e bexiga natatória. Um processo, chamado de *looping* do tubo digestivo, ocorre entre 26-30 hpf, no qual porções do mesmo são deslocadas da linha mediana para a esquerda da mesma. A PML foi envolvida neste processo devido às suas assimetrias migratórias que impõem o deslocamento da endoderme. O primeiro primórdio pancreático emerge também por volta das 24 hpf, o primórdio dorsal, que dará apenas origem ao tecido endócrino. O segundo primórdio, aparece bastante mais tarde, por volta das 40 hpf, o primórdio ventral que dá origem tanto a tecido endócrino como exócrino, assim como os ductos pancreáticos. O primórdio do fígado emerge entre as 24 e 28 hpf, estendendo-se da linha axial para a esquerda sobre o saco vitelínico.

Tendo em conta que Nodal afeta a taxa de migração das células, nomeadamente as da endoderme e que a expressão assimétrica de *dand5* muito provavelmente é responsável pela expressão assimétrica de *spaw* nas células da PML, neste projeto de tese, propusemos que as células migratórias da endoderme e precursoras do tubo digestivo possam ser afetadas pela sinalização Nodal (Spaw). Consequentemente, estas células podem migrar mais rápido no lado esquerdo que no lado direito, onde Spaw é supostamente inibido por Dand5. Sabendo que estas células apresentam um comportamento migratório antes da difusão da expressão assimétrica de *spaw* e *elovl6*, propomos um papel ativo para estas células. Sugerimos testar se os sinais ED, imediatamente após a quebra da simetria na KV podem afetar a padronização ED das células migratórias da endoderme. Também propomos a hipótese destas células integrarem o tubo digestivo, em formação durante estes estadios, e poderem contribuir para a formação dos órgãos assimétricos como o fígado e pâncreas. Assim, o nosso objetivo secundário, foi estudar o destino destas células da endoderme com comportamento migratório.

Utilizando uma linha repórter *Tg(sox17:GFP)*, procedemos ao estudo do comportamento migratório das células endodérmicas com captação de imagens ao vivo e análise paralela de embriões fixados. Sox17 é um marcador da endoderme permitindo visualizar as células que queremos estudar assim como a KV, o tubo digestivo e órgãos derivados do mesmo. Reportamos então neste estudo a formação de um agregado de células *sox17:GFP*$^{+}$, não reportado anteriormente, o qual chamámos de '*cluster*', localizado numa região posterior à KV aos 10 ss. Observámos que é a partir deste agregado que as células *sox17:GFP*$^{+}$ começam a migrar em direção ao lado anterior do embrião aquando da passagem da KV sobre o mesmo devido ao crescimento da cauda. Este resultado levanta a questão de porque é que estas células formam este agregado posterior e não se intercalam formando o tubo digestivo como as outras *sox17:GFP*$^{+}$. Os estudos de captação de imagens ao vivo não produziram resultados com diferenças significativas entre a ED. A falta de significância estatística foi justificada pelo tamanho sub-ótimo da amostra. Por outro lado, os estudos com embriões fixados, foram robustos em número de embriões e permitiram uma resolução excelente em profundidade. Observámos assim diferenças significativas entre ED, nomeadamente no número de células migratórias, maior no lado esquerdo aos 13 e 14 ss, assim como denotamos uma maior dispersão e distância à KV aos 14 ss. Para averiguar o destino destas células de posicionamento assimétrico, realizámos um estudo com Kaede, uma proteína fotoconvertível por UV, pelo que fotoconvertemos as células do agregado a 8ss bem como os dois grupos de células migratórias de cada lado da KV a 14 ss. No entanto, após varias tentativas os resultados obtidos não nos permitiram concluir se as células alvo incorporam o tubo digestivo. Pensamos que a proliferação celular dilui a Kaede fotoconvertida, não permitindo esta observação.

Em conclusão, conseguimos caracterizar o padrão de migração das células *sox17:GFP*$^{+}$, tendo sido observadas algumas assimetrias ED em análises temporais. Desta forma, este trabalho valida a nossa hipótese inicial em que a migração das células endodérmicas seria afetada assimetricamente em relação

ao eixo ED. Propomos então um mecanismo alternativo no qual sinais ED assimétricos, ocorrentes nas células da KV podem estar a afetar o comportamento migratório da endoderme. Para tal, o próximo passo é a manipulação destes sinais assimétricos para testar se o comportamento das células *sox17:GFP*$^{+}$ observado é alterado. Também sugerimos a continuação de estudos complementares de captação de imagens ao vivo com vista a determinar o destino das células alvo.

Palavras chave: Assimetria Esquerda-Direita, peixe-zebra, *sox17*, Sinalização Nodal, Migração Celular

Abstract

The establishment of the left-right (LR) axis is fundamental for the correct position of visceral organs. In vertebrates, asymmetry is established with the expression of *nodal*, *southpaw (spaw)* in zebrafish, only in the left Lateral Plate Mesoderm (LPM). Current knowledge shows that in most vertebrates the symmetry breaking event occurs in a specialized structure called the LR organizer (LRO), where biophysical interactions determine the first asymmetric clues. In zebrafish, the LRO is called Kupffer's vesicle (KV), a transient fluid-filled, monociliated organ, which appears during the early segmentation period at the posterior end of the notochord. In zebrafish, *spaw* expression is bilaterally symmetric in the cells surrounding the KV at 4-6 ss becoming asymmetrical in the left LPM around 10–12 ss. Motile cilia inside the KV ensure a counter-clockwise fluid flow that is important to establish the first asymmetric gene expression of *dand5* at 8 ss. Dand5 is a secreted protein shown to be a potent Nodal inhibitor. The exclusive left sided *southpaw (spaw)* expression at the lateral plate mesoderm is thought to be the result of the earlier Dand5-Spaw inhibition near the KV. Previous data have shown a possible migration of endodermal gut precursor cells very close to the KV and other studies have demonstrated that Nodal affects cell migratory speed, namely in endodermal cells. So, we hypothesized that endodermal cells on the left side of the KV being exposed to more Spaw will migrate faster than the ones on the right side where Spaw is inhibited by Dand5. To characterize the migratory behaviour of these gut precursor cells we used the *Tg(sox17:GFP)* reporter line using two photon live-imaging as well as complementary time-course fixed samples. We observed that endodermal cells form a cluster at the posterior midline that is disassembled by cell migration triggered by the KV passing over it. Additionally, even though live studies did not show significant differences in measurements such as migration speed and track displacement, perhaps due to our small sample size, differences in the pattern of cell migration on the Left versus Right sides were observed in fixed embryos. These included differences in several parameters, such as the number of cells, distance to KV centroid, distance between cells. To understand if the migratory *sox17:GFP*$^{+}$ cells were indeed incorporating the gut tube and where, we performed photoconversion experiments using Kaede. However, the results did not allow us to take such conclusions, mainly due to the fact that cell proliferation dilutes photoconverted Kaede. Still, in this study we showed that there is asymmetric positioning of migratory endodermal cells in a LR manner. We thus propose an alternative mechanism in which LR asymmetric cues that take place in the KV cells can affect endodermal migratory behaviours. Therefore, the next step will be to manipulate LR signals within the KV in order to test if the observed asymmetries are indeed originated from R>L *dand5* asymmetric expression. We also suggest performing more live imaging studies in order to determine the fate of the migratory endodermal cells.

Keywords: Left-Right Asymmetry, zebrafish, *sox17*, Nodal Signalling, Cell Migration

Index

List of Figures

List of Abbreviations

LR - Left-Right
AP - Antero-Posterior
DV - Dorso-Ventral
e.g. – for example
LPM - Lateral plate mesoderm
LRO - Left-right organizer
KV - Kupffer's Vesicle
PCD – Primary ciliary dyskinesia
DFC - Dorsal forerunner cells
ss - somite stage
ECM - Extracellular matrix
spaw - *southpaw* (gene)
Spaw - Southpaw (protein)
lft1 - *lefty1* (gene)
Oep – One-eyed pinhead (protein)
hpf – hours post-fertilization
cp - *ceruloplasmin* (gene)
WT - wild type
E3 - embryonic medium
PTU - 1-phenyl-2-thiourea
TUNEL - terminal deoxynucleotidyl transferase dUTP nick end labelling
PFA - paraformaldehyde
DAPI - 4',6-diamidino-2-phenylindole
PCNA - Proliferating Cell Nuclear Antigen
i.e. – That is
LMA - low-melting agarose
NA - Numerical aperture
ROI - Region of interest
FRAP - fluorescence recovery after photobleaching
2p - two-photon
3D - three-dimensional
4D – four-dimensional
N - sample size

1. Introduction

1.1 - LR Asymmetry

Symmetry is defined as the quality of exact similarity of parts around an axis and it may seem as the predominant pattern in nature. However, morphological asymmetries are present within the body structures of several organisms regarding the left-right (LR) axis. In higher organisms, the establishment of the body shape occurs during embryogenesis, this process implicates development and coordination of Anterior-Posterior (AP), Dorsal-Ventral (DV) and LR axes **[1]**.

The external body plan of vertebrates is bilaterally symmetric, however visceral organs and vasculature exhibit LR asymmetry regarding their position and pattern. These asymmetries are evident in heart positioning, which loops asymmetrically during development and lastly acquires a leftward position in the chest cavity. Also, the gut coils asymmetrically and the stomach and pancreas are placed on the left side and the liver on the right in the abdomen. The number of lobes is different in each right and left lung and some morphological and functional asymmetries are present in the brain **[1]**. The normal organ positioning is named as *situs solitus* (Fig. 1.1 (A)) and is the one characteristically present in the vertebrate body **[1–3]**. Possible evolutionary reasons for this LR asymmetry have been hypothesized such as optimization of gastrointestinal organ package due to its length and compartmentalization **[4]** blood flow dynamics **[5,6]** and maximizing the surface area of the tubes **[7]**.

When anomalies are present during LR axis determination this can lead to a spectrum of congenital disorders that affect the arrangement and morphology of the visceral organs. Regarding the position of the organs, these LR anomalies are classified as *situs inversus* (Fig. 1.1 (D)), when all organs are arranged in a perfect mirror-image inversion with respect to the other two body axes, and *situs ambiguous*, also termed heterotaxy, which is described by abnormal arrangement with discordance in LR asymmetry as some thoracic and/or abdominal organs develop normal LR asymmetry and others do not. This disorder may include isomerism, in which organs develop symmetrically (*e.g.* left or right atrial isomerism (Fig. 1.1 (B-C)), this condition is highly linked with health problems and prenatal death. In humans, it is estimated that heterotaxy is prevalent in 1 per 10000 total births **[8]** and it is associated to significant foetal and perinatal lethality in humans and other vertebrates too, mostly due to its implications in complex cardiovascular malformations. *Situs inversus* is associated with rather less mortality, and individuals may not present health problems. Nevertheless, as defects in cilia are usually associated with this condition, affected individuals may suffer from respiratory, kidney and reproductive functions **[1,3,9]**.

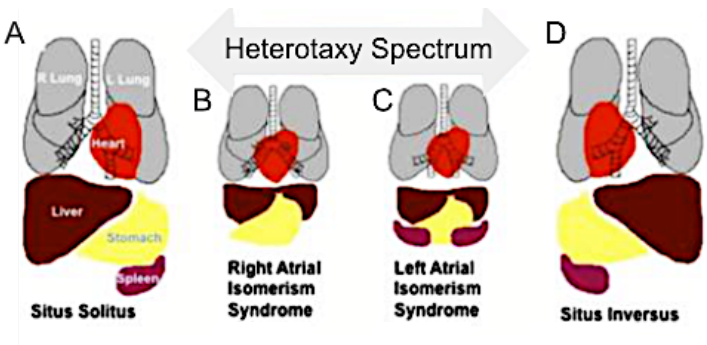

Figure 1.1 – Human anatomy of situs disorders. (A) *Situs solitus*. The cardiac apex is oriented leftward, the right lung is trilobed, the left bilobed, the liver is on the right, and the stomach and spleen are on the left. (**B-C**): Heterotaxy. **(B)** Right atrial isomerism. Both lungs are trilobed, the liver is midline, asplenia is present (spleen malfunction) and heart apex orientation is random. **(C)** Left atrial isomerism. Both lungs are bilobed, the liver is midline, presence of multiple spleens and heart apex orientation is random too. **(D)** *Situs inversus*. Exact mirror-image of *situs solitus*: the cardiac apex is rightward, the right lung is bilobed, the left trilobed, the liver is on the left, and the stomach and spleen are on the right. Adapted from **[10]**.

1.2 – The LR Organizer, Cilia and Symmetry Breaking

In vertebrates, asymmetry is established with the expression of Nodal only in the left Lateral Plate Mesoderm (LPM), the predominant model states that the symmetry breaking event occurs in a specialized structure called the LR organizer (LRO) in most vertebrates, enabled by polarized cilia which produce an asymmetric fluid flow, perceived as the driving force in this defining event.

These LROs are known as the node (Fig. 1.2 (A)) in amniotes **[11,12]**, gastrocoel roof plate (Fig. 1.2 (B)) **[13**] in amphibians and Kupffer's vesicle (KV) (Fig. 1.2 (C)) in teleost fish **[14,15]**.

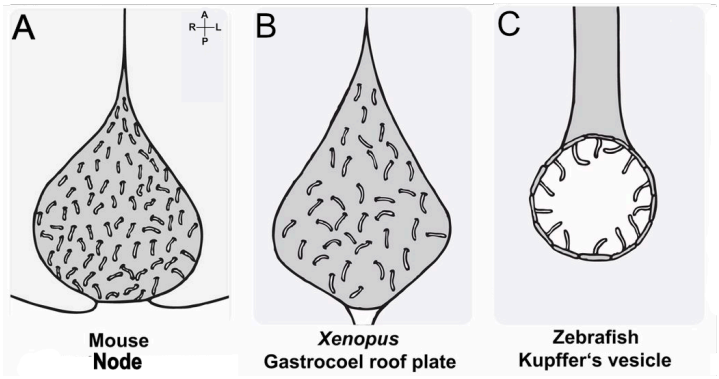

Figure 1.2 – Graphic representation of LROs in the vertebrate modal organisms. (A) The LRO in mouse, the node. An indentation at the distal tip of the egg cylinder. **(B)** The gastrocoel roof plate, LRO in *Xenopus*. A flat triangular to diamond-shaped epithelium. **(C)** KV, an epithelial and spherical structure that is the LRO in zebrafish. In all models, LRO is positioned at the posterior pole of the notochord (gray). Axes are indicated: A, anterior; P, posterior; L, left; R, right. Adapted from **[4]**.

Even though the asymmetric Nodal expression is conserved, the upstream defining event is not completely conserved among vertebrates **[16]**. In chicken, mutants with cilia defects develop normal LR asymmetry **[17–19]** and asymmetric cell movements responsible for asymmetric signalling were identified around Hensen's node **[20].** The LRO in the pig embryo also lacks cilia and extraembryonic fluid exposure **[16,20]** plus the cow LRO shows absence of an exposure to the embryonic fluid as well **[16]**. Thus, a cilia-independent mechanism to establish LR asymmetry is suggested for some vertebrates namely the ion-flux model **[21]**. A conceivable explanation for the vertebrate exceptions to this model resides in the possibility of early developmental events generating LR positional information to later guide ciliated cells during the formation of LROs. In some vertebrates, where cilia were lost, this LR positional information could bypass the requirement for cilia in a novel rather than ancestral mechanism for symmetry breaking **[4,22]**.

In fact, the first link between LR patterning and motile cilia was provided in humans by studying a rare genetic disorder called primary ciliary dyskinesia (PCD). PCD is characterized by respiratory dysfunction and male infertility and it was discovered that those conditions were due to loss of cilia motility **[23,24]**. Respiratory defects are consistent with loss of cilia movement since in airways, motile cilia beat to promote mucociliary clearance of debris and pathogens. Similarly, infertility is explained by the loss of motility of flagella, which are structures related to cilia that control sperm movement **[9]**. Additionally, half of the individuals with PCD present *situs inversus* and heterotaxy was also found in PCD patients with cilia motility defects **[25,26]**, indicating that cilia are involved in establishing normal LR and loss of cilia can result in either reversed or ambiguous laterality **[27]**. Studies in patients with laterality defects revealed mutations in numerous genes responsible for proper cilia motility **[28,29]**.

1.2.1 – Kupffer's vesicle

The zebrafish LRO, KV, is a transient fluid-filled, monociliated, epithelial and spherical structure and appears during the early segmentation period at the posterior end of the notochord **[15,30]** (Fig. 1.3). KV is derived from a cluster of superficial cells in the region adjacent to the embryonic shield, named the dorsal forerunner cells (DFC) **[31]**, this cluster results from the association and ingression of a group of 20 to 30 dorsal surface epithelial cells controlled by Nodal signalling. The DFC cluster then migrates towards the vegetal pole, in a collective cell migration process **[15,30,32–35]**. Subsequently, DFCs become polarized in a bottle-shaped structure by compaction to later form rosette-like structure, and at around 4-6 somite stage (ss) the lumen is formed **[32]**. Lumen expansion by fluid influx occurs simultaneously with ciliogenesis, in which a single cilium forms and elongates from the apical surface of each KV cell to extend into the lumen **[15,36–40]**.

Simultaneously, regional cell shape is altered by both the notochord and cytoskeletal rearrangements leading to an increase of extracellular matrix (ECM), and imposing an asymmetric distribution of cilia within the KV, which are more abundantly distributed on the anterior-dorsal region **[40–43]**.

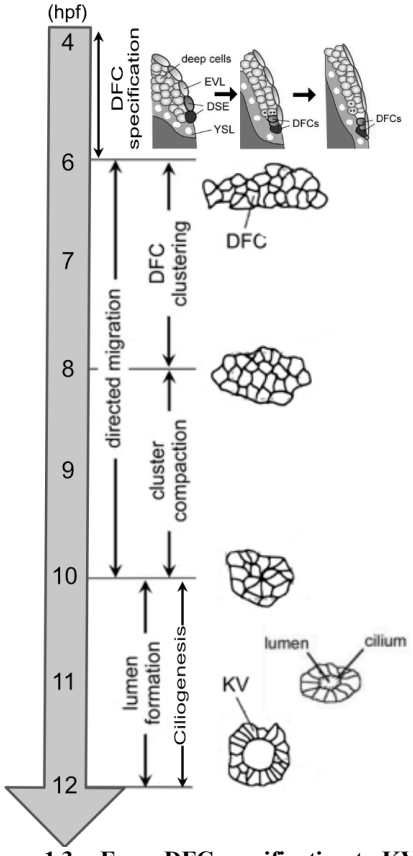

Figure 1.3 – From DFC specification to KV organogenesis. This process comprises ingression of surface epithelial cells and specification of the DFCs precursors. DFC cells form a cluster through adherens junctions that then becomes compact. During this process, the cluster migrates with a defined migration path, in a collective migration manner. Later, the internal lumen is formed and undergoes expansion and ciliogenesis. Adapted from **[32,33].**

1.2.2. – Cilia in the zebrafish KV

The mouse node was where the first studies were performed providing evidence for the importance of cilia in LR patterning **[44–46]**.

In the zebrafish LRO, as in the mouse node, a directional fluid flow is produced, but in this case in a counterclockwise direction **[47]**. This directional flow is generated by motile cilia (Fig. 1.4 (C-E), (G-H)), performing a rotational movement in a tilted manner regarding the posterior and dorsal axes. Additionally, due to KV regional cell shape modifications, cilia become asymmetrically distributed, with a higher distribution in the anterior-dorsal region (Fig. 1.4 (G-H)) **[40]** which is extremely important for the flow dynamics that will follow the same pattern: stronger flow anteriorly than posteriorly **[48]**.

As well as in the node, KV harbours immotile cilia (Fig. 1.4 (D), (F), (G-H)) besides the motile ones that generate the flow **[49,50]**. Moreover, the balance between the number of motile and immotile cilia was demonstrated to be crucial for an effective flow capable of translating into an asymmetric *dand5* expression and consequently correct LR patterning **[50]**. Contrasting with the mouse node where only two motile are necessary for a functional LR patterning **[51]**, in zebrafish KV, a minimum of about thirty motile cilia are required **[49,50]**. This dissimilarity is thought to be due to differences in organ morphology and cilia number and distribution, the node is a flatter shaped structure where all motile

cilia are on the floor and the KV is an ovoid closed organ with cilia all around (Fig. 1.4 (A-B)), where ventral pole cilia generate flow antagonistic to the desired flow **[48]**. Additionally, KV cilia length was found to be a determining feature for functional flow generation **[35,52,53]**.

Likewise in the mouse LRO, no consensus was yet established in whether the asymmetric flow is detected in a mechanical sensing way by the immotile cilia (Fig. 1.4 (J)) **[49,50]** or in a chemical sensing manner by detection of molecules that are transported by the flow to the left side (Fig. 1.4 (I)) **[54]**.

The generated flow in the zebrafish seems to promote the intracellular $Ca2^{+}$ increase on the left-sided cells of the KV via phosphorylation of the $Ca2^{+}$/Calmodulin-dependent protein kinase II (CaMK-II) **[55,56]**. The $Ca2^{+}$ channel Pkd2 was also demonstrated to be crucial in zebrafish **[57,58]**. The mechanism of calcium signalling is still under debate but it has been described as first detected as intraciliary calcium oscillations that are then transmitted to the cytosol and later to KV adjacent cells **[59]**.

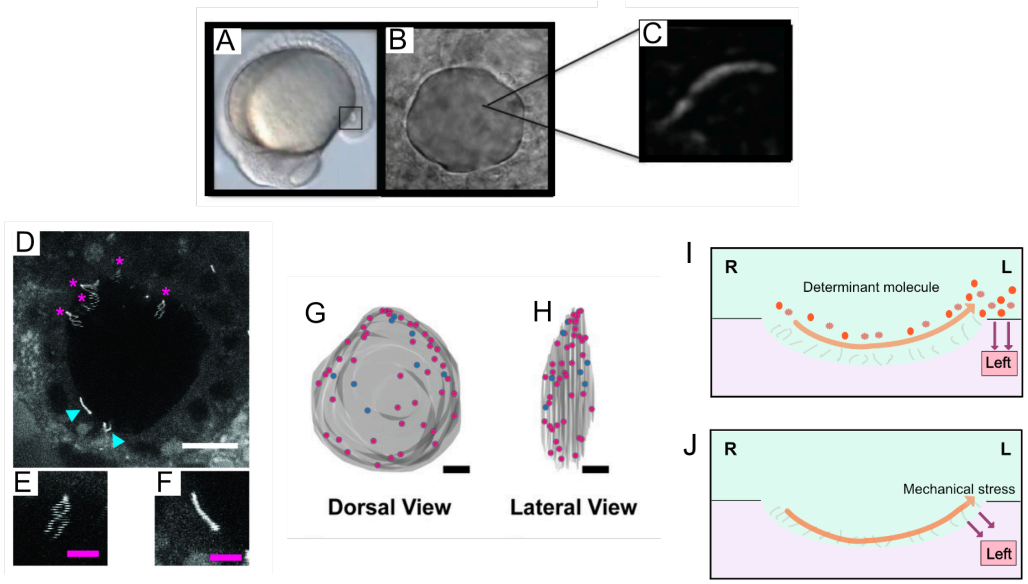

Figure 1.4 – Cilia in zebrafish LRO. (A) KV localization (square region) in a 14hpf zebrafish embryo. **(B)** Snapshot of a KV in a live embryo filmed. **(C)** Snapshot of a beating cilium in a live embryo KV. **(D)** Snapshot of a slow scanned KV from an embryo injected with arl13b-GFP mRNA at 1 cell stage. Blue arrowheads: immotile cilia; Magenta arrowheads: motile cilia. Scale bar= 20 µm. **(E-F)**: Details of a motile **(E)** and immotile cilia **(F)**. Scale bar= 5 µm. **(G-H)**: 3D projections of representative KVs showing the position of motile (magenta dots) and immotile cilia (blue dots) in a dorsal **(G)** and lateral **(H)** view. **(I-J)** Two different models on how cilia sense the flow. **(I)** Cilia sense the flow by chemical molecules being transported by the flow for the left side. **(J)** Generation and sensing of mechanical stress by leftward node flow at the cilia. Scale bar= 20 µm. Adapted from **[49,50,60]**.

1.3 – The Nodal Signalling Pathway in LR Asymmetry

The Nodal Signalling Pathway is considered quite conserved and it is known to be present in both protostomes, deuterostomes and possibly in their last common ancestor, the Urbilateria **[4]**.

Currently, it is known that TGFβ family ligands function in both symmetry breaking and the transmission of this information to adjacent tissues **[61]**. The pathway is both genetically and biochemically well characterized (Fig.6.1). In short, LR asymmetry establishment in vertebrates is controlled by Nodal auto-induction when it expands to the left LPM, inhibition by antagonists Cerberus and Lefty, the latter activated by nodal expression and the activation of the transcription factor Pitx2 (extensively reviewed in **[2,61–63]**).

1.3.1 – The Nodal Signalling Pathway in LR Asymmetry: Zebrafish

In zebrafish, only one of the three nodal genes, *southpaw* (*spaw*) is involved in breaking and transducing LR asymmetry **[64]**. In contrast to the mouse model, the expression of *spaw* occurs in a symmetric bilateral shape in the cells surrounding the KV at 4-6 ss (Fig. 1.5 (A-B)) **[64]**. Later on, around 10-12 ss *spaw* expression becomes asymmetrical in the left LPM [**64]**. This Spaw asymmetric pattern in the LPM might be an outcome of the activity of the positive feedback loop of $Ca2^{+}$ signals perhaps promoting the processing/secretion of Spaw protein only in the left side of the KV by the mechanisms referred in section 1.2.2.

Dand5 formerly known as Charon, a member of the Dan family which are Cerberus-like proteins, therefore a nodal antagonist, is thought to be actively involved in generating this asymmetry in the zebrafish LPM **[53,64,65]**. The expression of *dand5* in the KV is initially symmetric at 5-7 ss, however this changes around 8 ss when it starts exhibiting a right-sided asymmetric pattern in a fluid flow-dependent way, being the first asymmetrically expressed gene in the KV (Fig. 1.5 (B)) **[53]**. Nevertheless, it is still not clear if this switch is due to an upregulation of the *dand5* levels on the right side or a downregulation on the left side of the KV **[49,53]**. As a nodal antagonist, Dand5 binds to Spaw allegedly more on the right side, inhibiting it from stimulating expression of *spaw* mRNA at the right side of the LPM (Fig. 1.5 (C)) **[65]**. Although not fully demonstrated because antibodies for Spaw or Dand5 are not efficient, the absence of an antagonist on the left side seems to allow Spaw to diffuse from the region near the KV towards the left LPM and stimulate its own expression in this area (Fig. 1.5 (D)). The underlying mechanism is still not well understood, however it was found that Dvr1, a member of the TGFβ family and zebrafish Vg1 orthologue, facilitates the transfer of *spaw* expression from the peri-KV region to the left LPM and its ability to enhance the Nodal response pathway was also demonstrated **[66]**.

At the left LPM, Spaw will induce a positive feedback on itself and amplify its own expression beginning at 12 ss in the posterior end of the LPM and then spreading along the AP axis in a posterior-to-anterior direction covering the whole left side of the LPM, in a very defined stripe of expression, until 22 ss (Fig. 1.5 (C-D)) **[67]**. Pitx2, a conserved homeodomain transcription factor, is a target of the nodal signalling **[68]** hence Spaw also stimulates *pitx2* expression at the left LPM in an overlapping region with its own expression. *pitx2* expression at the left LPM starts around 13 ss and propagates along the AP axis in the same way as *spaw* (Fig. 1.5 (E-F)) **[67]**. Even though zebrafish *pitx2* is expressed on the left LPM in a Nodal dependent way it was found that in zebrafish *pitx2* is not required for normal heart and gut laterality **[69]** opposing to other vertebrates, such as the mouse in which its expression translates into the proper orientation of asymmetric organs **[70–72]**. The authors Ji *et* al., 2016 **[69]**, suggest that *elovl6*, a fatty acid elongase, is involved in organ laterality establishment in zebrafish instead of *pitx2*. It is an adjacent gene to *pitx2* on chromosome 14, and is asymmetrically expressed alongside *pitx2* at the LPM around 18 ss and normal left-sided *elovl6* expression depends on KV function and Nodal signalling **[69]**. However, we still do not know if mutants for Elov16 have LR problems.

Moreover, Spaw will activate the expression of its own regulators that restrict the extent of Nodal signalling, the *lefty* genes concurrently with *pitx2.* Lefty is thought to repress Spaw signals by physically associating with both Spaw itself as well as with EGF-CFC coreceptors, in zebrafish One-eyed pinhead (Oep) **[73–75]**. *lefty1* (*lft1*) is expressed in the midline around 10 ss, before *spaw* expression in the left LPM and starts propagating anteriorly at 15 ss reaching the anterior end of the midline around 20-22 ss (Fig. 1.5 (D-F)) **[67]**. The expression of *lft1* is activated by Spaw once it propagates anteriorly and by BMP signalling **[67,76,77]**. Therefore, the midline act as a barrier confining the domain of *spaw* expression to the left LPM. In the absence of *lft1,* restricted *spaw* expression to the left LPM begins normally, however Spaw later leaks to the right side stimulating its own expression in the right LPM **[67,77]**. Also, an 'anterior barrier' and 'posterior barrier' have been described in the zebrafish embryo. Contrasting to other vertebrates, which express *lefty2* throughout the left LPM **[78,79]**, in zebrafish *lefty2* is only expressed in the left cardiac field (Fig. 1.5 (F')) **[64]** preventing *spaw* expression from propagating across the region anterior to the notochord, into the right LPM and then spreading to the posterior region. Additionally, BMP signalling was found to be involved in preventing the propagation of *spaw* to the right LPM across the ventral mesoderm underlying the tail bud **[80]**. Besides acting as

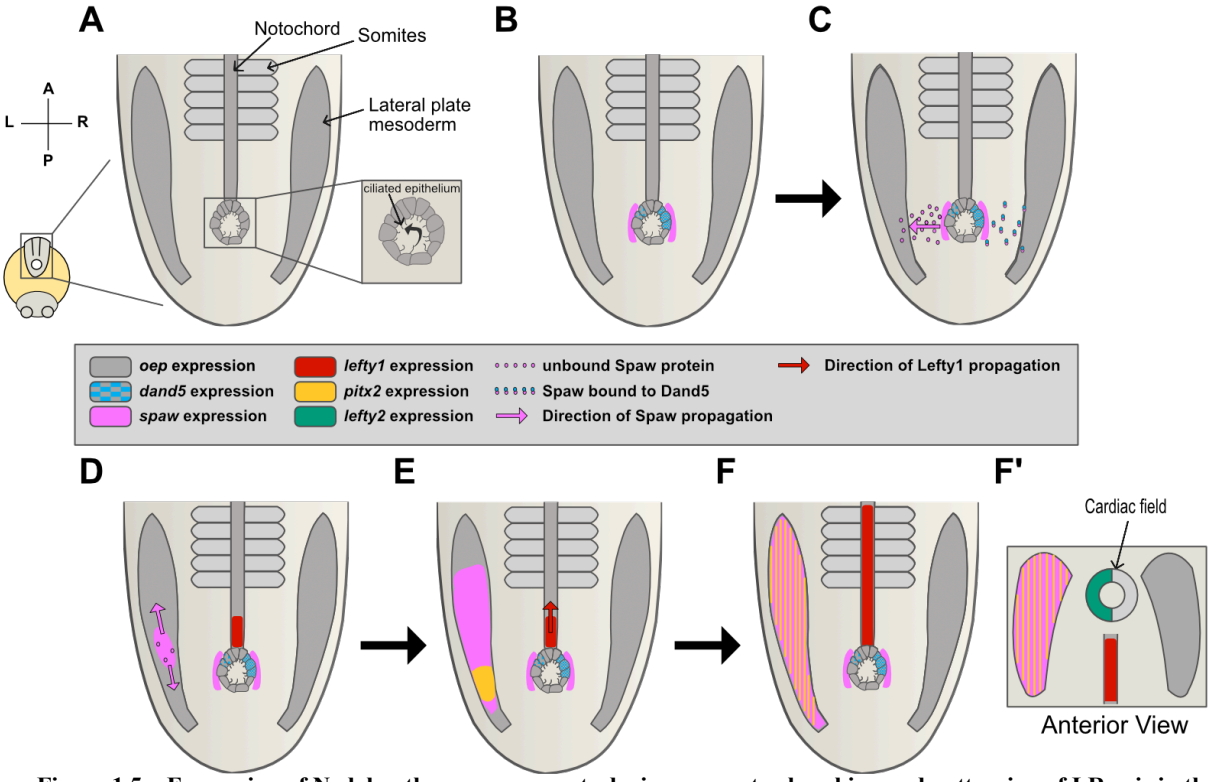

Figure 1.5 – Expression of Nodal pathway components during symmetry breaking and patterning of LR axis in the zebrafish embryo. (A) Structures involved in LR patterning as the KV, with a close-up showing cilia distribution and the flow leftward direction; LPM and the notochord. Also, the structures close as the somites. **(B-C)** Symmetry breaking. **(B)** *spaw* is first symmetrical expressed in the around the KV. **(C)** *dand5* is the first asymmetric gene expressed at the KV. Dand5, a Spaw inhibitor, will bind to Spaw and avoid its diffusion to the right LPM. **(D-F)** Asymmetric expression of Spaw and downstream targets. **(D)** Spaw will induce its own expression within the left LPM and its antagonist, *lefty1,* which is already expressed at the posterior part of the notochord. *spaw* expression propagates first to the posterior side and then to the anterior side of the LPM. **(E)** *spaw* propagation throughout the LPM taking place as well as *lefty1* to the anterior side of the notochord. *pitx2* starts being expressed in the left LPM. **(F)** *spaw* and *pitx2* are expressed all over the LPM and *left1* at the notochord. **(F')** *lefty2* is expressed in the left cardiac field in the zebrafish embryo. Both *lefty1* and *lefty2* will act as barriers, to avoid Spaw leaking to the right LPM. Adapted from **[62,80]**.

barrier, a novel role for the midline was proposed, where Oep represses the *lft1* expressed in the notochord, thus decreasing the threshold for Spaw and promoting the activation of the Nodal cascade in the LPM **[81]**.

Recently, a new study showed that the *prrx1* gene is asymmetrically right-sided expressed in a transient manner in the LPM of the zebrafish embryo. Prrx1, like Pitx2, is a paired-like homeobox transcription factor, and an epithelial-mesenchymal transition inducer in embryos and cancer cells. The study provides evidence that Prrx1 may repress *pitx2* and can be involved in directing cardiac progenitors to the posterior pole asymmetrically **[82]**.

1.4 – Gut formation and its asymmetric patterning in the zebrafish embryo

The zebrafish gut is an endoderm derived structure and, as in other vertebrates, it is divided in pharynx, oesophagus, liver, pancreas, intestinal bulb, and a posterior intestine **[83]**.

The endoderm corresponds to the cells of the blastoderm that are mostly located in the dorsal half of the zebrafish mid-blastula margin, and are subjected to inductive signals (TGFβ signalling) **[84]**. Fate mapping studies have shown a correlation between the cell position along the dorso-ventral axis before gastrulation and its future location regarding the AP axis, with the cells located most dorsally giving rise to the anterior endoderm, and the most ventral cells developing into the posterior portions of the gastrointestinal tract **[84,85]**.

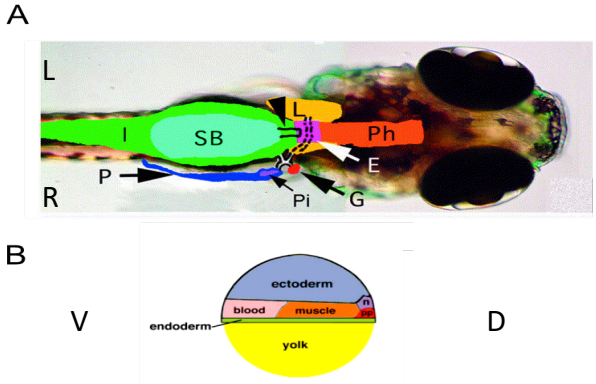

Figure 1.6 – **Zebrafish larval digestive system anatomy and embryo fate map. (A)** Dorsal view of a 5dpf larva. Overlay outlines the pharynx (Ph), esophagus (E), liver (L), pancreas (P) with solitary islet (Pi), gallbladder (G), swimbladder (SB), and intestine (I). Broken and solid lines depict ducts of the liver, pancreas, and gallbladder. **(B)** Fate map of an WT embryo; (n) cells fated to become notochord and (pp) prechordal plate. Axes are indicated: A, anterior; P, posterior; L, left; R, right.; V, ventral; D, dorsal. Adapted from **[86,87]**.

1.4.1 – Endoderm specification and morphogenetic movements

The process of endoderm specification and development is managed by a complex successive interaction of signalling pathways and transcription factors **[88]**. Nodal signalling is involved in regulating both endoderm and mesoderm, and the zebrafish nodal ligands, Squint and Cyclops, expressed at the vegetal margin of the blastoderm and antagonized by Lefty family members, are the ones involved in this process **[89]**. Sox32 is crucial in endoderm development **[90]** and induces the final endoderm determinant *sox17*.

Firstly, endoderm undergoes complex morphogenetic processes during gastrulation and then as it converges towards the midline and extends to cover the entire AP axis extent of the embryo.
During gastrulation, the endodermal digestive organ progenitors involute and migrate to the embryonic midline. This medial migration of gut endoderm is completed at around 18 ss **[84]**, which is considered a late developmental stage compared to the mammalian endoderm, completing migration through the primitive streak as gastrulation ends **[87]**. These medially displayed gut precursors form an endodermal

rod, rearrange, polarize and form a lumen **[91]**. By 20 hours post fertilization (hpf), a solid multicellular midline rod has formed and a clear lumen can be seen throughout most of the endoderm by 42 hpf **[83]**. The rod will give rise to the components of the digestive tube and the connected organs such as the liver, gall bladder, pancreas and swim bladder (Fig. 1.6 (A)). This early gut is divided in foregut, midgut, and hindgut, and an asymmetry emerges with the displacement of gut portions from the midline in a process called gut looping. This occurs at developmental stages ranging from 26-30 hpf in a particular region regarding the AP axis extent that will give rise to the liver and intestinal bulbs, which moves to the left of the midline. It was demonstrated that the LPM is involved in this event, cells of the LPM flanking the endoderm present morphological as well as migratory asymmetries that are imposed to the endoderm in a mechanism of pushing it to the left (Fig. 1.7 (A), (B)) **[92]**. ECM remodelling occurring downstream of the Nodal-Pitx2 pathway is responsible for that asymmetric migratory cell behaviour, comprising Laminin depletion regulated by HAND2 transcription factor **[93]**.

Although this looping movements establish asymmetries in gut tube disposition, the liver which is displayed on the left side and pancreas on the right of this tube, start emerging as buds from the tube before it even starts, and their progenitor cells are already committed to their fate long before it **[83]**.

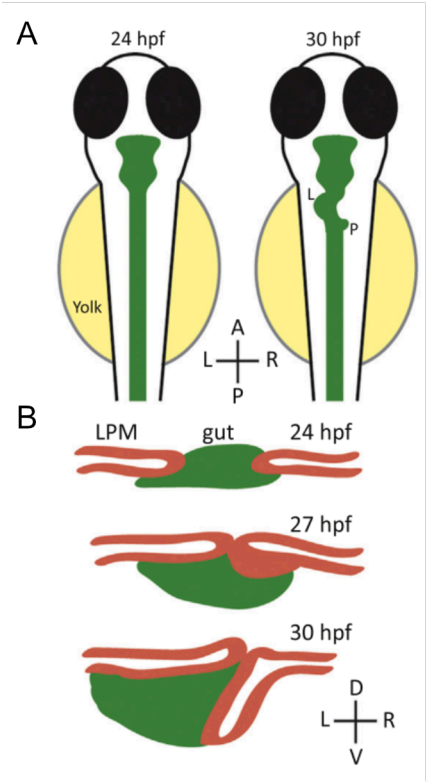

Figure 1.7 – Timing of zebrafish gut looping. (A) The gut endoderm (green) undergoes looping between 24 and 30 hpf. By 30 hpf, the liver (L) and pancreatic (P) buds have emerged and the intestine has looped asymmetrically. **(B)** At 24 hpf, the gut presents itself as a central rod surrounded by LPM. LMP (orange) then migrates medially towards the endodermal rod, the left LPM migrating dorsally and the right LPM migrating ventrolateral. Around 30 hpf, the gut presents a shift to the left because of the LPM migrations. Axes are indicated: A, anterior; P, posterior; L, left; R, right. Adapted from **[3].**

In this dissertation, I am only focused on the emergence of the buds from the gut tube and not in the complete gut organogenesis.

1.4.2. – Pancreas and liver budding

The zebrafish pancreas as in other vertebrates, presents an exocrine duct and an endocrine one **[94,95]** which present a separated origin from two contiguous areas of the gut, emerging as two different buds **[95,86]**. The first pancreatic bud emerges at around 24 hpf, the dorsal bud (Fig. 1.8 (A)). Contrasting to mammals, this first pancreatic bud only gives rise to endocrine tissue expressing the main pancreatic hormones **[86]**. The movements occurring during the gut looping dislocate this dorsal bud to a more right-sided position and the first islet will be organized by 48 hpf (Fig. 1.8 (B)).
The ventral bud emerges later, after 30 hpf (Fig. 1.8 (B)) and grows in a posterior direction towards the dorsal bud gradually surrounding it (Fig. 1.8 (C)) **[86,96,97]**. This second bud gives rise to both exocrine tissue, pancreatic ducts and later to a small portion of endocrine cells that differentiate adjacent to the duct **[86]**.

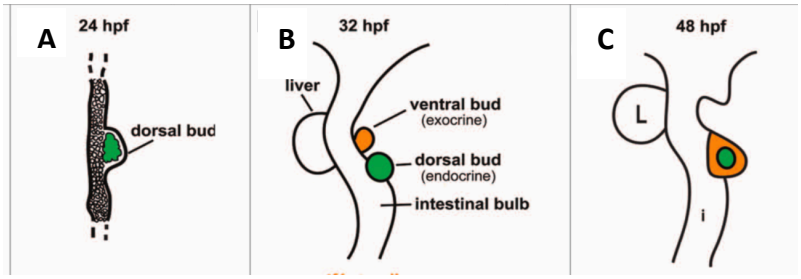

Figure 1.8 – Embryonic pancreas development in zebrafish. (A) Endocrine cells cluster and the dorsal bud emerges at 24hpf. The rest of the endoderm compacts into the primitive gut tube. **(B)** The ventral bud emerges much later around 40 hpf. **(C)** The second pancreatic bud grows in a posterior direction towards the dorsal bud surrounding it. Adapted from **[98].**

The liver bud emerges between 24 and 28 hpf extending to the left from the midline over the yolk sac (Fig. 1.9 (B)) **[86]**. Becoming restricted in this region the expression of some hepatic markers specified from the endoderm between 22 and 26 hpf. In the beginning of the budding stage, the endoderm cells posterior to the pharyngeal region aggregate to form the endoderm rod at 24 hpf. Later, at around 26-28 hpf the endoderm segment positioned under the first somite begins to thicken and this is when the liver morphogenesis first starts. After 28 hpf, this anterior thickening starts to grow and bends to the left side during the gut looping process **[92]** covering the outer curvature of intestinal bulb by 30 hpf. Around 34 hpf a groove is formed between the liver bud and the adjacent oesophagus, also later markers of hepatic

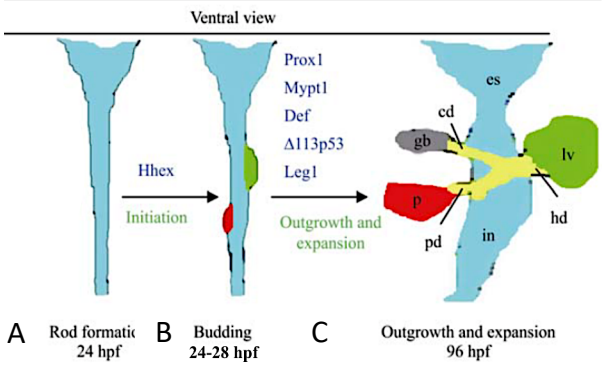

Figure 1.9 – Ventral view of the stages of embryonic liver development in zebrafish. (A-B) Liver budding is promoted by Hhex and hepatoblast migration by Prox1. **(C)** Mypt1 mediates the BMP-producing cells directly abutting the liver primordia to promote liver bud growth. v: liver, green; p: pancreas, red; in: intestine, cyan; gb: gall bladder, gray; es: esophagus, cyan; hd: hepatic duct, yellow; pd: pancreatic duct, yellow; cd: cystic duct, yellow. Adapted from **[99]**.

development are expressed, such as *ceruloplasmin* (*cp*). Later, this bud undergoes dramatic increase in liver size (Fig. 1.9 (C)) **[99]**.

1.5 – Nodal and cell migration

It was demonstrated that disruption of Nodal signalling reduces the speed and directional movement of zebrafish cardiomyocytes and disrupts the leftward morphogenesis plus the rotation of the cardiac cone. Establishing another role for Nodal in generating LR asymmetry by regulating the speed and direction of cardiomyocyte movement **[100]**. Later studies confirmed this influence of Nodal signalling in directing migration of the left atrial cells during the cone stage as well as identified target transcription factors **[101,102].**

The role of Nodal regulating endodermal cell movement was first proposed by pioneer studies in *Xenopus* and zebrafish **[103,104]**. Nevertheless, the mechanisms by which it could affect cell motility remained unknown until Woo *et al.,* (2012) **[105]** demonstrated that by inhibiting Nodal signalling the velocity of cell migration was slowed but also migration persistence was increased. This study demonstrated that Nodal signalling affects actin dynamics in endodermal cell migration mediated by Rac1 and induces expression of Rac activator Prex1 as a Nodal signalling target.

1.6 – Are LR signals from KV directly reaching gut precursors?

In summary, we have just reviewed here that it is known that Nodal affects cell migratory rates, namely in endodermal cells. We have also reviewed earlier that the asymmetric expression of *dand5* is very likely responsible for the asymmetric expression of *spaw* in cells surrounding the KV and later in the LPM (Fig. 1.10 (B-D)). Thus, we hypothesize here in this thesis that the populations of migratory endodermal gut precursor cells, that are near the KV might be affected by the asymmetric presence of Spaw. So, we envisage that endodermal cells on the left side of the KV, being exposed to more Spaw will migrate faster than the ones on the right side where Spaw is inhibited by Dand5 (Fig. 1.10 (B-D)). In case we are correct, we go even further and question if those same cells that would be migrating faster on the left side or slower on the right side will integrate the arising gut and be part of any asymmetric buds.

The migratory behaviour of the endodermal gut precursors is observed much earlier than the Nodal asymmetric expression diffusion to the LPM. At 10 hpf (bud stage) these cells are already migrating towards the midline while asymmetric expression of mRNAs for *spaw* and *elovl6* appear at the LPM at 12 ss and 18 ss, respectively. Thus, we predict that endodermal cells are migrating before the classical Nodal cascade at the LPM, known to specify organ lateralization, is fully running. So, that the cells passing closer to the KV around 8-10 ss could be experiencing the Nodal influence exerted on the left side and lack of it on the right, influencing their migratory rates prior to the organ laterality specification by the LPM (Fig. 1.10 (C-D)).

The gut endodermal cells we are referring to are localized between the LRO and the LPM, and studies in the mouse have demonstrated a passive role for the endodermal cells by mediating the transfer of signals from the organizer to the LPM via gap junction coupling across the endoderm **[106,107]**. We are not disregarding this passive role, which might be present in the zebrafish as well, however, we are proposing an additional possible active role for endoderm cells in gut LR patterning.

In summary, we are proposing an alternative mechanism in which these initial LR signals, immediately after symmetry breakage, could affect LR patterning of accessory organs of the digestive system in the zebrafish embryo, without limiting this patterning only to Nodal-(Pitx2)-Elovl6 pathway in the LPM specification.

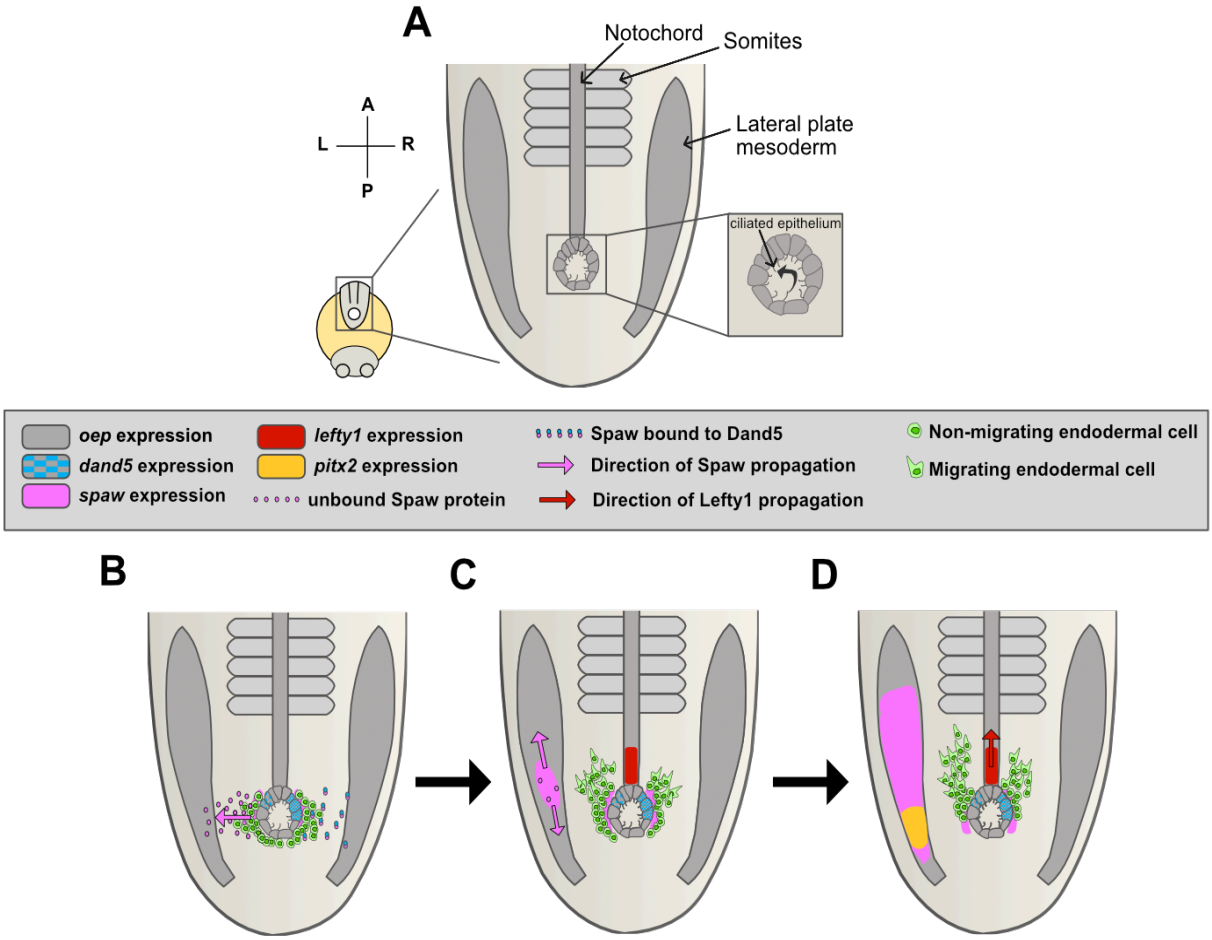

Figure 1.10 – Our hypothesis: hypothetical asymmetrical migration of gut endoderm cells and expression of Nodal pathway components during symmetry breaking and patterning of LR axis in the zebrafish embryo. (A) Structures involved in LR patterning as the KV, with a close-up showing cilia distribution and the flow counterclockwise direction; LPM and the notochord. Also, the structures close as the somites. **(B)** Symmetry breaking. *spaw* is first symmetrically expressed at the KV, *dand5* is the first asymmetric gene expressed at the KV. Dand5, a Spaw inhibitor, will bind to Spaw and avoid its diffusion to the right LPM. Gut endoderm precursors are present close to the KV at 10 ss and can be affected by Dand5 asymmetric inhibitory role. Since Dand5 is likely inhibiting Spaw mainly on the right side, cells on the left side of the KV will be able to be affected by Spaw. **(C-D)** Asymmetric expression of *spaw* mRNA and Spaw protein (pink circles) and predicted asymmetric migration of gut endoderm cells. **(C)** Spaw will induce its own expression within the left LPM. Also, the expression of its antagonist, *lefty1,* which is already expressed at the posterior part of the notochord. *spaw* expression propagates first to the posterior and then to the anterior of the LPM. The gut precursor cells on the left side influenced by Spaw protein will start migrating faster than the ones on the right side. **(D)** *spaw* propagation throughout the LPM taking place as well as expression of *lefty1* to the anterior of the notochord and *pitx2* starts being expressed in the left LPM. We predict that asymmetric migration of gut precursor cells might persist through time and that those cells on the left side will possible incorporate the gut earlier than the ones on the right side. Adapted from **[62.80]**.

1.6.1 – Objectives

The main objective of this project was to determine if LR asymmetric cues that take place in the KV cells, namely the *dand5* right-sided asymmetric expression pattern, correlate with any asymmetric migratory behaviour of gut precursor cells in wild type embryos. To do so, we aimed to characterize the

migratory behaviour of cells labelled by the *Tg(sox17:GFP)* reporter line using two photon live-imaging as well as complementary time-course fixed samples.

A secondary objective was to explore the fate of those same endodermal cells, asking if their final location corresponded to gut asymmetric organs such as, liver and pancreas. We planned to track those gut migratory cells throughout gut development using Kaede photo-convertible experiments.

2. Materials and Methods

2.1- Zebrafish line and maintenance

All experiments in this project were performed using the *Tg(sox17:GFP)* zebrafish transgenic line. Adults were maintained at 28 ºC in a tailored zebrafish aquatic re-circulating system (techniplast) with a 14 h light /10 h dark photoperiod. Homozygous individuals were outcrossed with wild type (WT) and incrosses were performed with heterozygous parents so that we had different sources of transgenic fish showing *sox17:GFP*$^{+}$ cells. The collected embryos were raised in embryonic medium (E3) at 25 ºC before manipulations and were kept at 28 ºC after manipulations until reaching the desired developmental stage, according to Kimmel et al.,1995 **[108]**. The compound 1-phenyl-2-thiourea (PTU) was added at 24-26 hpf so that the embryos did not show pigmented melanocytes that could compromise the imaging protocol. All experiments were performed during the embryonic stages (8 ss - 48 hpf). When needed for image acquisition embryos were anesthetized with 3-6 drops of Tricaine 25x using a 2 mL.

2.2 – Molecular Techniques

2.2.1 - TUNEL Assay

To detect and quantify apoptosis, a terminal deoxynucleotidyl transferase dUTP nick end labelling assay (TUNEL) was performed using the *In Situ* Cell Death Detection Kit (Roche Applied Sciences).

At 13 and 14 ss embryos were fixed with paraformaldehyde (PFA) 4% and washed for a few days in a PBS solution in the dark at 4 ºC. Embryos were then submitted to two additional washes in PBS Triton 0.1% and manually dechorionated in the same solution. Samples were incubated in acetone for 7 min at -20 ºC and treated with Proteinase K (1:1000) for 1 and 3 min, for 13 ss and 14 ss respectively. Embryos were then post-fixed in PFA 4% during 20 min at RT, followed by several washes in PBS and then incubated in TUNEL reaction solution ON at 4 ºC. Control samples were supplied only with Label Solution. In the second day, the embryos were submitted to 3 washes with PBS and incubated ON at 4 ºC in a solution of 4',6-diamidino-2-phenylindole (DAPI) diluted 1:1 in PBS. The third day consisted of 3 washes in PBS followed by mounting for image acquisition. For a more detailed protocol see section 6.2.1.

2.2.2 - Immunostaining: PCNA

To detect the presence of Proliferating Cell Nuclear Antigen (PCNA), an immunostaining protocol (section 6.2.2) was performed with the antibody anti-PCNA; after several trials, we were unable to obtain reliable staining.

2.2.3 – Kaede microinjection

In order to follow the fate of the desired groups of cells a subset of *Tg*(*sox17*:GFP) zebrafish embryos were collected and aligned to a microscope glass slide and injected at one cell-stage with 100 pg of Kaede mRNA. Using a pressure injector (850V Pneumatic PicoPump) (hold pressure= 3 psi; eject pressure= 20 psi) the injection needle was previously calibrated to a consistent volume of 1,4 nL per embryo.

2.3 - Microscopy and Image Acquisition

2.3.1 - Kaede photoconversion

The injected embryos were kept in the dark in E3 at 25 ºC, and mounted for imaging in 1% low-melting agarose (LMA). The photoconversion of Kaede was performed on a Leica TCS SP5 confocal laser scanning microscope, using a 40x 0.8NA water-immersion objective controlled by the LAS AF software. Two different groups of ROIs were targeted: At 8-9 ss we selected the cluster of *sox17*:GFP^{+} cells localized posterior to the KV and we named it "Cluster ROI". At 13-14 ss, the L and R groups of *sox17*:GFP^{+} cells were selected and named "Bilateral ROIs". A fluorescence recovery after photobleaching (FRAP) application was used to perform the conversion using the 405 nm laser. By setting an optical zoom of 1.5x, the desired ROIs were selected and subjected to a 9 s exposure of 50% 405 nm UV laser in "Fly mode" and scanning speed of 400 Hz. Images before, during and post UV exposure of the entire region and "Bilateral ROIs" were acquired using the FRAP application. Z-series stacks were acquired after the photoconversion in a 1024×1024 pixel matrix; z-step size ranged from 1-2 μm.

2.3.1.1 – Screening of photoconverted Kaede injected embryos and whole embryo imaging

In a first step, confirmation of photoconversion was performed by acquiring images of embryos with 5 and 10 h after the photoconversion and also at 26, 40 and 48 hpf looking for cells positive for red *Kaede* using a Zeiss STereo LUMAR stereoscope, equipped with a Hamamatsu Orca-ER CCD camera, controlled with the MicroManager v1.14 software. Photoconverted embryos were kept at 28 ºC and in the dark to avoid further photoconversion of non-target cells, and later assessment of red photoconverted Kaede was performed through live imaging (section 2.3.2.2).

2.3.2 - Two-photon microscopy imaging.

In order to image *sox17:GFP*$^{+}$ cells in motion in whole zebrafish embryos, time-lapse sequences of live embryos were acquired with a Praire Ultima two-photon system (2p), equipped with a Coherent Chameleon Ti:Sa pulsed laser, mounted on a Olympus BX60 upright microscope using a 20x 1.0NA water-immersion objective and either MultiAlkali or GaAsP detectors (an upgrade was performed during our experiments); the system was controlled with the Praire View software v4.6 and (later) v5.3.

2.3.2.1 Live embryos: migration of *sox17:*GFP^{+} cells

At developmental stages of 7 and 10 ss, embryos were mounted in 1% LMA in a petri dish with dorsal side upwards facing the objective and fully submerged in E3. Only one embryo with the highest expression and best orientation was chosen for imaging, while the others were monitored only at the end of the imaging session and compared to confirm that exposure to laser radiation did not cause malformations or developmental arrest. The 1% concentration of LMA proved to be the best compromise between efficient immobilization of the embryo and normal morphological development. The microscope was equipped with a PECON temperature-controlled chamber set to 28 ºC. For all embryos, the optical slices were acquired at a 2 μm step intervals and each z-stack acquisition was performed in cycles of 3 or 6 min of duration and optical zoom set to 1.5x. Z-stacks for each cycle were acquired in a 1024×512 pixel format to minimize photo damage (different resolution in x and y) skipping every other line. The 2p laser was tuned to wavelengths 890-920 nm. The number of cycles varied between embryos as well as the number of z-stacks (50-70 optical slices).

2.3.2.2 Live embryos: photoconverted *Kaede*

After photoconversion on the LeicaSP5 confocal, embryos were transferred to the 2p system for live-imaging. Z-stacks were acquired at 5 and 10 h after the photoconversion and also at 26, 40 and 48 hpf. The embryos were mounted in 1% LMA with the tail in a dorsal position and for the 48hpf the whole embryo was mounted in a dorsal position. The Z-step interval was set to 2.3 µm and z-stacks were acquired in a 1024×512 anisotropic pixel format. During the imaging acquisition process, the embryos remained in constant anaesthesia as described in section 2.3.1.2. The chamber temperature was set to 28 ºC.

2.3.2.3 - Fixed embryos: migration of *sox17:*GFP$^+$ cells and TUNEL and PCNA analysis

Embryos with 10 and 12-15 ss were fixed in PFA 4% ON and stored for a few days in PBS at 4 ºC. The embryos were then mounted in 1.5% LMA in the same position as for live imaging to preserve uniformity between analysis. Z-stacks were acquired at a 1µm step intervals in a 1024 × 1024 pixel format skipping every other line with a 920 nm wavelength and the optical zoom set to 2x. embryos submitted to the TUNEL assay and PCNA immunostaining, z-stacks were acquired in the same manner, except for the wavelength that was defined to 850 nm. The optical zoom was set to 1.5x.

2.4 - Image analysis

2.4.1 - Live embryos: migration of *sox17:*GFP$^+$ cells

Z-stacks of 2p images were first positioned using Fiji software **[109]**. Embryo drift was corrected semi-automatically by using the ImageStabilizer (2D) plus a macro for 3D, or manually using the Amira V5.3 software (FEI), trying to "immobilise" the KV. Using Imaris v6.4 software (Bitplane), the z-stacks were reconstructed in 3D and reiterated through time to produce an accelerated 3D movie of *sox17:*GFP$^+$ cells migration. The cell tracking was manually performed for two different ROIs: one for the Left and another for the Right side. This 4D cell tracking analysis identified the x, y, and z coordinates for each cell at each given time point. We extracted the minimum, maximum and average values of the overall track length, *i.e.,* the measurements of total distance covered by the cells; track displacement; track speed; and track straightness index, a measure of directional persistence (displacement/track length). All measurements presented in this work were in relation to a "stationary" KV and vertical embryonic mid-axis. For a more detailed explanation of the procedure to immobilise the KV see section 6.2.3.

2.4.2 - Fixed embryos: location of *sox17:*GFP$^+$ cells

Z-stacks of 2p images were first were first positioned using Fiji software. Using Imaris v6.4 (Bitplane) software, z-stacks were reconstructed into 3D images and we extracted x, y, and z coordinates for the centre point of the lumen of the KV for every embryo. Cells were counted in 4 different defined ROIs: (a) Left Migrating; (b) Left Non-Migrating; (c) Right Migrating and (d) Right Non-Migrating. Although this part of the study used fixed embryos (*i.e.*, we had no information about migratory behaviour of those cells), we classified cells from the aggregate in the vicinity of the KV as "migrating" or 'non-migrating' if they showed or not a clearly polarised morphology with the nucleus closer to the KV, and large protrusions facing away from the KV (Fig.6.2 (A-B)). A MATLAB 2016a script was written (Section 6.2.4.1) to calculate LR migration parameters and represent the distribution of the cells from the exported x, y, and z coordinates. The "number of cells" was given by the number of cells for which

the position was noted and the volume (μm^3) relative to the 3D distribution of the cells was calculated from the shape described by the cells 3D coordinates (*i.e.*, the volume of the "cloud" of 3D coordinates). The cell density (cells.μm^{-3}) was also determined. Regarding the coordinates obtained for the centroid of the KV, average, maximum and minimum distance of cells to KV centroid (μm) were calculated for all cells; the same parameters were calculated just for the y coordinate, average, maximum and minimum anterior distance of cells in to KV (μm) respectively, as a measure of the displacement along the embryos AP axis. The average, maximum and minimum distance between cells (μm) was also calculated. For a more detailed procedure see section 6.2.4.1.

2.4.3 - Fixed Embryos: cell proliferation and TUNEL analysis

Z-stacks of 2p images were first processed using Fiji software for embryo alignment as previous described. The selection of the ROIs and cell counting was performed using the same approach described in previous section, except that we only defined Left and Right regions regarding the KV position. Red cells marked by the TUNEL kit, were counted using Fiji software by examining every z-slice to supplement Maximum Intensity Projections. Since PCNA immunostaining did not work, we performed cell proliferation analysis by counting cells seen undergoing mitosis, in the same embryos processed for TUNEL using Fiji software as well (Fig.6.3 (A-B)). This was possible because the embryos were stained for DAPI.

2.4.4 - Photoconverted embryos

The z-stacks acquired were first processed using Fiji software, embryo position was corrected as previously described for the other analysis. Bin transformation was applied using the same parameter previously described for the live imaging migratory study. For 48 hpf embryos, z-tacks of the tail were acquired in different sections to cover the tail extension. Z-stacks were all joined to produce one image of the tail using the 3D Stitching plug-in. All the embryos were analysed in a composite view of the two channels in order to detect the presence of yellow cells, cells where *sox17*:GFP co-localizes with red photoconverted *Kaede.* We searched for yellow cells as described in the previous section.

2.5 - Statistical analysis and image processing

All graphs were done using Prism (Graphpad) software v6c and statistical significant differences between Left and Right for all parameters was determined by paired, non-parametric comparisons, using the Wilcoxon test. Comparisons between consecutive developmental stages were determined by unpaired, non-parametric comparisons, using the Mann-Whitney test. Both statistical tests are present in the referred software. Only p-values < 0,05 were considered statistically significant. Images were processed using the Affinity Designer software.

3. Results

3.1 – *sox17:GFP*$^{+}$ cells form a cluster posterior to the KV

To characterize the migratory behaviour of the *sox17:GFP*$^{+}$ cells known to be located close to the KV, we performed time-lapse imaging using *Tg*(*sox17:GFP*) embryos. During an initial approach, this was performed in different but adjoining developmental stages to understand the dynamics regarding the timing of the migration onset. We observed that around 10 ss (N=4) in an adjacent posterior region to the KV there was an unreported aggregate of *sox17:GFP*$^{+}$ that we that we call "the cluster" (Fig. 3.1 (A); video 1 in supplemental) which we imaged in detail in fixed embryos (N=9; Fig. 3.1 (E)). The "cluster" cells were easily distinguishable from adjacent *sox17:GFP*$^{+}$ cells because they were arranged as compact aggregate rather than a more dispersed arrangement typical of the other *sox17:GFP* cells (Fig. 3.1 (A), (E)).

As normal development proceeded, the tail underwent elongation and the KV acquired a more posterior localization. During this elongation, the KV moved over the cluster (Fig. 3.1 (B)), and while passing over it we observed that cells from the cluster started migrating away from the cluster, now positioned ventral to the KV. Initially, only a few cells moved away from the KV (Fig. 3.1 (C)) heading laterally, *i.e.*, moving along the X axis when the embryo's AP axis is oriented vertically (Y axis); we called this "lateral migration". As time passed, more cells were seen migrating away from the KV and a different migratory behaviour was observed, with cells appearing to turn towards the anterior region on both the left and right sides, which we called 'anterior migration' (Fig. 3.1 (D)). To properly understand and measure these movements we processed the movies by semi-automatically translating each frame in order to "immobilise" the KV, *i.e.,* in the movies analysed and presented the KV was kept stationary; note that this does not reflect the natural overall movements of embryonic structures, where the intrinsic KV drifts posteriorly due to tail elongation. This allowed us to understand better the movements of individual cells in relation to the KV, which we considered to be their "point of origin", in other words, cells' movements are reported relative to the location of the KV.

These movies also allowed us to observe the formation of the primordial gut. A cell-free space was observed in the midline which, together with the centre of KV lumen, we considered to be the embryo's mid axis. This region corresponds to the notochord located in a more dorsal position and the gut is known to be formed below the notochord at this midline region. As we reviewed in section 1.4.1, the two sheets of endodermal cells migrate towards the midline and then the ones closest to the borders rearrange to start forming the gut. This was indeed observed throughout the time-window covered in the videos (Fig. 3.1 (A-D)). By tracking the cells migrating anteriorly we were able to determine if those cells located close to the KV, and migrating from the cluster, would incorporate the gut and contribute to asymmetric digestive accessory organ specification.

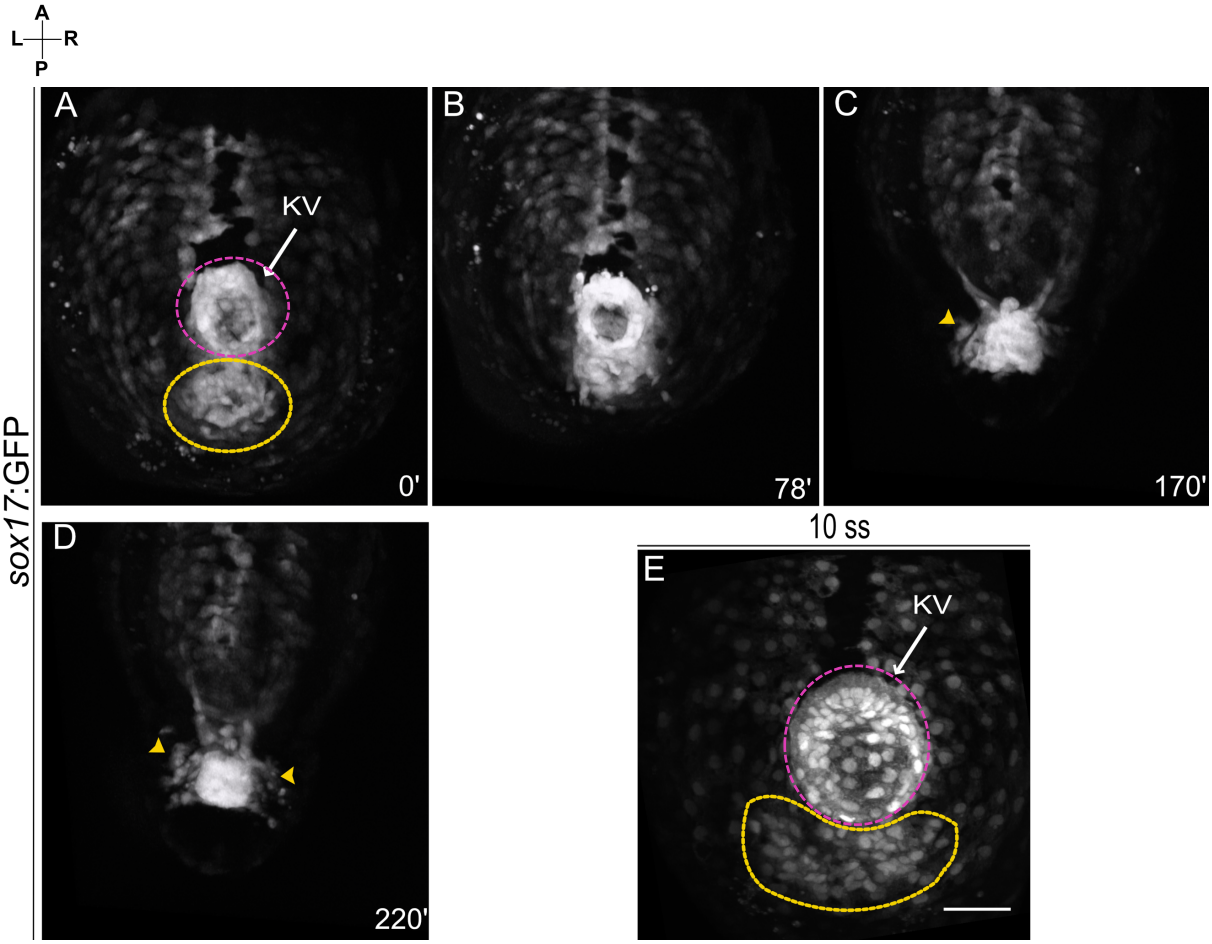

Figure 3.1 – Imaging of *sox17:GFP*$^+$ cells revealed an unreported cluster of cells posterior to the KV. (A-D) Time-lapse imaging from two-photon z-stacks of a *Tg*(*sox17:GFP*) embryo, starting at 10 ss. **(A)** A cluster formed by *sox17:GFP*$^+$ cells (yellow dashed region) is visible in an immediately posterior region to the KV (magenta dashed region and pointed by a white arrow). **(B)** Later, around 78 min after, the KV is seen to start passing over this cluster due to typical tail elongation. **(C)** Right after the KV reaches the whole cluster, a few cells start migrating away from the cluster (yellow arrowhead) and later more cells are seen performing the same migratory behaviour (yellow arrowheads) on both left and right sides **(D)**. KV is maintained stationary by image processing in the time-lapse video and the elapsed time is indicated in minutes (‘) at bottom right. **(E)** Two-photon z-stacks are displayed as a MIP of a 10 ss *Tg*(*sox17:GFP*) fixed embryo, where the cluster of cells (yellow dashed region) can be observed, located posteriorly to the KV (magenta dashed region). Scale bar = 50 μm. Axes are indicated: A, anterior; P, posterior; L, left; R, right.

3.1.1 *sox17:GFP*$^+$ cell cluster

To understand better the fate of the cell cluster we tracked the behaviour of those *sox17:GFP*$^+$ cells located posteriorly to the KV in a period of development prior to 10 ss where the cluster is well established already. By performing time-lapse imaging starting at 7 ss (N=1) (Fig. 3.2 (A-C); video 2 in supplemental) we observed that the cluster was formed progressively; it was not evident at 7ss (Fig. 3.2 (A)) but gradually cells converged towards the midline (Fig. 3.2 (B-C)). This can clearly be seen by displaying the associated tracks and displacement vectors (lines and arrows in Figs. 3.2 B, C)), beginning when individual cells were first visualized and ending when they left the imaging space or the imaging terminated. In short, this cluster was formed after 7 ss but prior to 10 ss by *sox17:GFP*$^+$ cells migrating towards the midline in a posterior region to the KV. At 10 ss the cluster was already a compact aggregate. The number of cells comprising this cluster was also counted (N=9) in fixed embryos at 10 ss (Fig. 3.2 (D-E)) and we determined that this cluster is constituted by an average of 42 cells ($\bar{x}$ = 42,33; σ = 8,41) (Fig. 3.2 (E)).

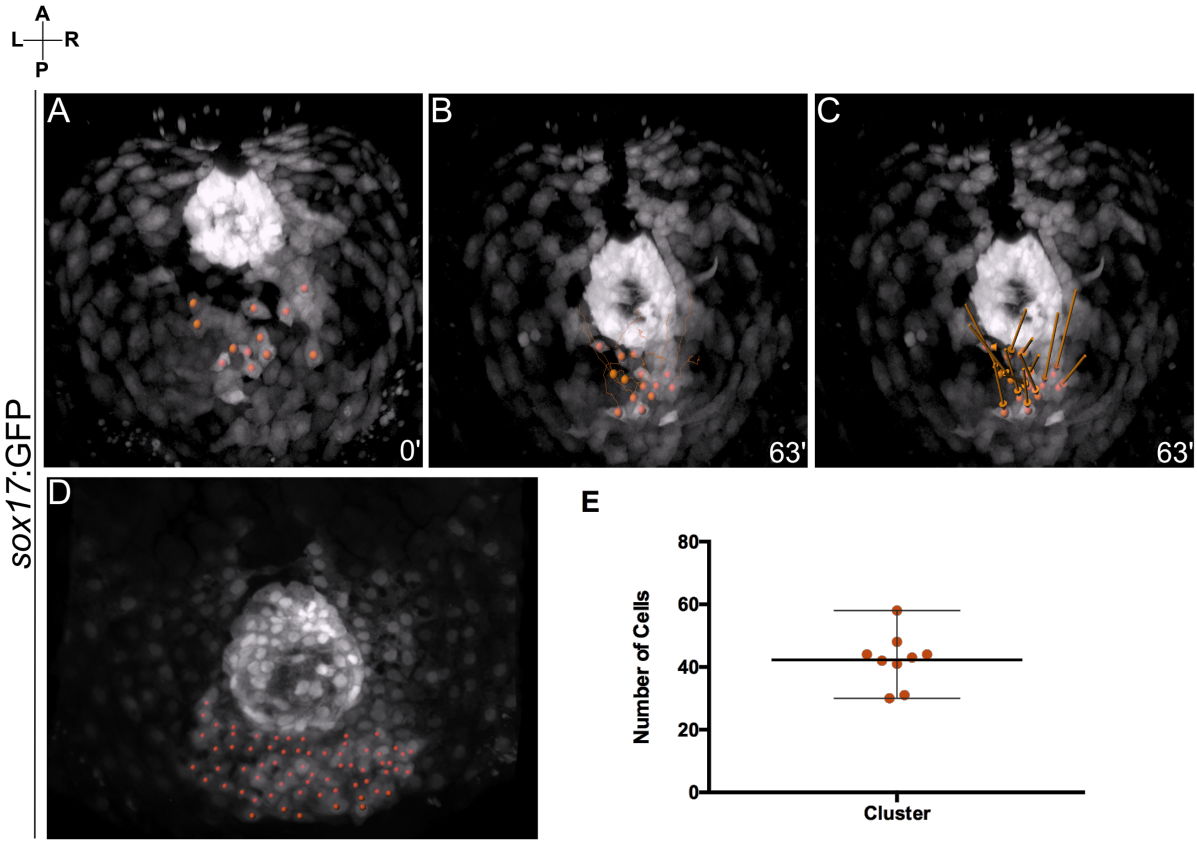

Figure 3.2 –*sox17:GFP*$^+$ cells cluster characterization. (A-C) Representative tracking of individual migratory cells posterior to the KV. Cells were manually tracked in a 3D time-lapse of two-photon z-stacks of a *Tg*(*sox17:GFP*) embryo starting at 7 ss. Tracked cells are marked with orange spots. **(A)** *sox17:GFP*$^+$ cells show a relative dispersed distribution posteriorly to the KV at 7 ss. **(B-C)** Later at 63 min, those cells have migrated and aggregated. Associated tracks **(B)** and displacement vectors **(C)** are shown. **(D)** Illustrative representation of cell counting process at 10 ss in *Tg*(*sox17:GFP*) embryos (N=9). Axes indicate: A, anterior; P, posterior; L, left; R, right. **(D)** Graphical representation of the number of cells forming the cluster (N=9); whiskers are extended to the most extreme data point that is no more than 1.5 × interquartile range from the edge of the box (Tukey style).

3.1.2 Migration pattern characterized by live-imaging

The main objective of this work was to characterize the migratory behaviours of the cells that migrated from the cluster described above. These cells were seen migrating away from the back of the KV on both left and right sides and we proceeded to test whether there were any asymmetric differences in their migratory behaviours. Even though we have acquired 16 time-lapse videos to address the migratory pattern of *sox17:GFP*$^+$ cells, we were only able to perform cell tracking analysis in 7 of those. This was mainly because while we were testing and optimizing the conditions to acquire the videos, several had problems that precluded the possibility of properly analysing cells movements; *e.g.*, some embryos grew with a curly tail which compromises the embryo normal development as well as the quality of the acquired video because the unnatural curvature affects the normal morphogenetic tissue movements, others were not properly attached to the LMA and ended up detaching from it, thus losing their fixed position. These difficulties were bypassed by trial-end-error trying to achieve the best LMA concentration (1%) required for an optimal mounting procedure, providing enough space for the embryo growth, while keeping it in a fixed position. Another obstacle we faced in order to acquire a suitable time-lapse video, was the timing in which the embryo needed to be anesthetized, since between 18-20 ss embryos start moving their tails which completely compromises the process of acquiring z-stacks over consecutive time cycles. Anaesthesia should not be used throughout development because its prolonged use is known to cause abnormal development.

The suitable time-lapse videos were analysed and cell tracking was performed by detecting individual cells over consecutive time points and associated tracks (Fig. 3.3 (A-C); video 3 in supplemental). We wanted to cover the first cells migrating away from the cluster and from and from our previous experience with the first videos

and the knowledge gained from observing fixed embryos (section 3.2), we started analysing videos starting at 11-13 ss with an average duration is of 3h. Longer time-lapse image acquisition would have be extremely interesting to a better understanding of these *sox17:GFP*$^{+}$ cells migratory pattern, however, as previous mentioned, due to growth and anaesthesia constrains, a different approach was required.

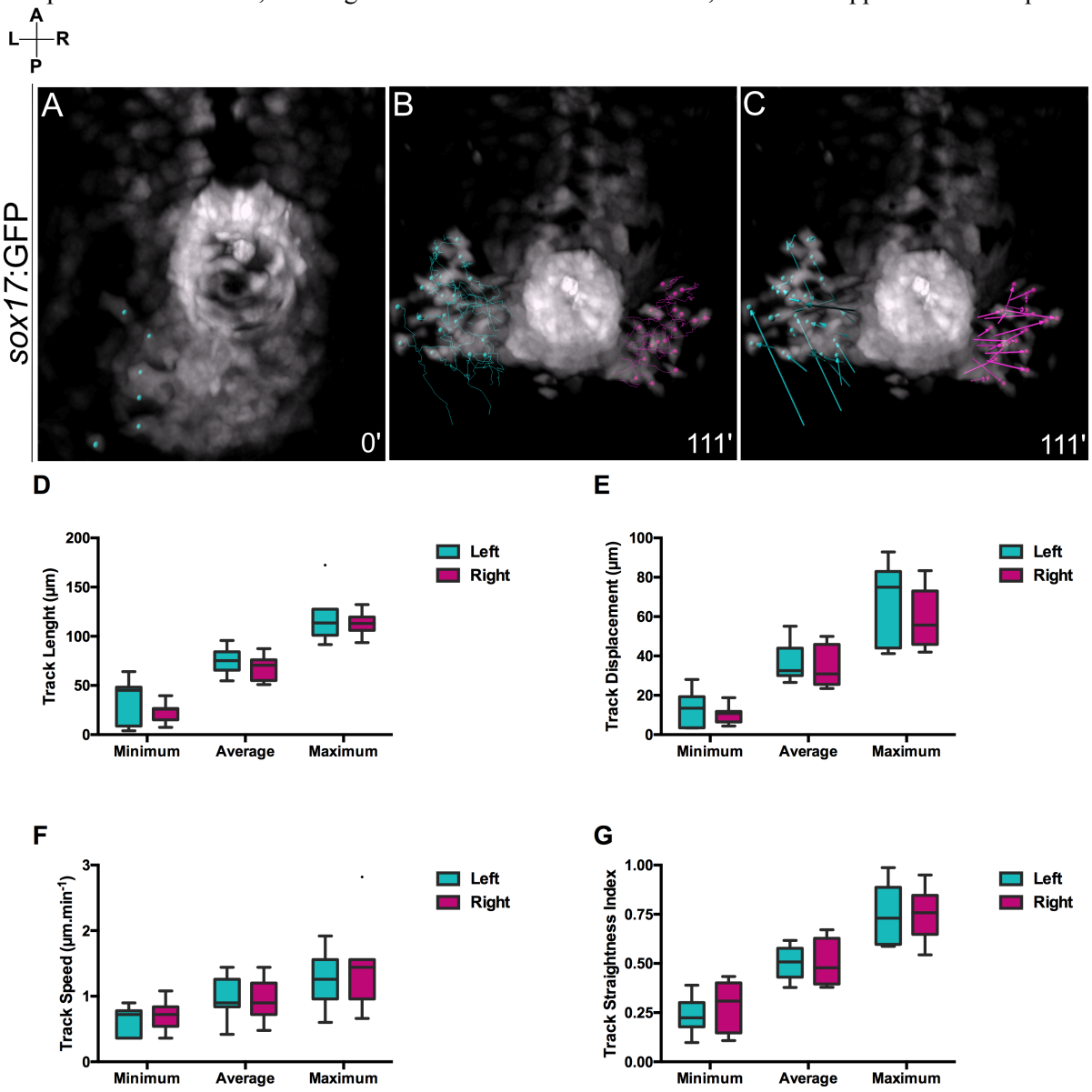

Figure 3.3 –*sox17:GFP*$^{+}$ cell migration characterized by live-imaging. (A-C) Representative tracking of individual cells. Migrating cells nearby the KV were manually tracked in a time-lapse of two-photon z-stacks of a *Tg*(*sox17:GFP*) embryo staring at 11 ss. Tracked cells are marked by cyan and magenta spots, on the left and right side, respectively. **(A)** at the starting point, spots mark the cells which start migrating in the consecutive time point. Cells on the left side start migrating prior to the ones on the right side. **(B-C)** Later, cells were seen migrating and cell tracking was performed. Associated tracks **(B)** and displacement vectors **(C)** are shown. Axes are indicated: A, anterior; P, posterior; L, left; R, right. **(D-G)** The LR Migration parameters extracted from the tracking data show no significant difference between left and right sides. Those parameters include: **(D)** The track length; (Minimum p-value= 0,2188; Average p-value= 0,2188; Maximum p-value= 0,3750); **(E)** track displacement (Minimum p-value= 0,375; Average p-value= 0,1563; Maximum p-value= 0,1563); **(F)** track speed (Minimum p-value= 0,4375; Average p-value>0.9999; Maximum p-value= 0,6875) and **(G)** track straightness index (Minimum p-value= 0,2969; Average p-value= 0,9375; Maximum p-value= 0,9375).

From the tracking data, we extracted the minimum, maximum and average values of the overall track length (Fig. 3.3 (D)). We measured also track displacement (Fig.3.3 (E)); track speed (Fig. 3.3 (F)); and track straightness index (Fig. 3.3 (G)). Associated tracks and displacement vectors are shown by lines (Fig. 3.3 (B)) and arrows (Fig. 3.3 (C)), respectively, beginning when individual cells were first visualized and ending when they left the imaging space or the imaging terminated.

The results showed that left-sided cells generally started migrating prior to the ones on the right side in 5 embryos out of 7 (Fig. 3.3 (A)). However, based on the analysis of the live movies, no significant differences were found when comparing left and right sides in any of the parameters analysed. This result suggests that there is no asymmetry regarding those parameters or the number of videos analysed is not large enough to reduce the level of uncertainty. Despite that no LR comparisons could be assessed, these data revealed significant findings regarding the studied parameters, since we had no previous knowledge about the behaviour of these *sox17:GFP*$^{+}$ cells. We learned that these cells migrate with an average speed of near 1 μm.min^{-1} (Fig. 3.3 (F)), and the minimum and maximum values range from 1 to 2 μm.min^{-1} (Fig. 3.3 (F)). Regarding the track length, it was observed that these values ranged from near 0 to close to 200 μm (Fig. 3.3 (D)) and track displacement varied from 0 to close to 100 μm (Fig. 3.3 (E)). Although no significant differences were found; these values appear to be greater on the left than on the right side. The track straightness index, measuring the directional persistence of migration, ranged from values close to 0 to 1, and the average for both sides stands close to 0.5 (Fig. 3.3 (G)). These values reflect the differences found between the total track length and displacement, and indicate that the behaviour of these cells is highly variable and perform a more rambling path than a directional one.

3.2.- Fixed embryos revealed left-sided asymmetry of *sox17:GFP*$^{+}$ migratory cells

Live-imaging studies require a faster scanning and therefore a small number of z-stacks to allow a representation over sequential cycles in small periods of time. To a better complementary characterization of the behaviour of these cells, we performed analysis using fixed embryos, which permitted the acquisition of images with a higher resolution in depth. We used fixed embryos from 11 ss to 15 ss (Fig. 3.4 (A-D)) to characterize the behaviour of these cells during development. Time-lapse videos had shown us that these cells start migrating at around 11 ss. However, due to intrinsic variance in development between embryos we chose to begin the analysis in a time point of active migratory behaviour for all the embryos, which was consistently observed at 12 ss (Fig. 3.4 (A)), therefore this was the starting point for this analysis. At 16 ss we observed that the KV starts to close, the lumen disappears becoming a compact group of cells, as the centre of the lumen is the primary symmetry axis chosen in this study for this early migration, embryos from somite stages later than 15 ss were excluded from this analysis.

Fixed embryos between 12 and 15 ss were analysed in 3D projections and four groups of cells were defined left migrating cells; right migrating cells; left non-migrating cells and right non-migrating cells (Fig. 3.4 (E)). As previously justified in section 2.4.2, this is a study using fixed embryos, for which we could not directly address the migratory behaviour of the cells. Thus, we established criteria (section 6.2.4.1) based on the acquired knowledge from the time-lapse videos to classify the cells as ‘migrating’ or ‘non-migrating’. Several migratory parameters, which were described in section 2.4.2, were calculated for both migrating and non-migrating cells concerning the left and right side. However, only the ones which showed LR asymmetries are referred below (Fig. 6.4 (A-G)).

Regarding the migrating cells, left-sided asymmetries were found for some of the parameters calculated. At 13 and 14 ss the number of cells is significantly higher on the left side (Fig. 3.4 (A)). The number of cells appears to increase from 12 ss to 13 ss and then starts to decrease until 15 ss, where significant differences can no longer be found. Another significant difference found during those somite stages was the average anterior distance of cells to KV, which was higher in the left side (Fig. 3.4 (H)). This measurement accounts for the migration in the y axis, *i.e.*, the migration from the posterior to the anterior side of the embryo by measuring the distance of the cells from the centroid of the KV. At 14 ss other asymmetries were observed, the volume of the surface described by the position of the cells (Fig. 3.3 (G)) was significantly higher on the left-side, meaning these cells present a broader distribution in 3D space besides being more numerous. These results are consistent with the other asymmetries found for average and maximum distance between cells (Fig. 3.4 (I-J)), a measurement for cell dispersion, for which the values are significantly higher on the left side. In summary, there are more cells migrating at 13 and 14 ss on the left side and these cells migrate further towards the anterior side of the embryo and exhibit a larger spatial distribution by being more dispersed at 14 ss.

No significant LR differences were found for the non-migrating cells (Fig. 6.5 (A-H)) except for the number of cells. We found that at 14 ss and 15 ss the number of cells was significantly superior on the left-side as well (Fig. 3.5 (A)).

Because the number of cells was the parameter with stronger statistical results for the left-side in both migrating and non-migrating, we decided to analyse the ratio of the number of migrating cells per total number of cells over the studied somite stages. The analysis was performed for left vs right cells per somite stage. LR comparison per somite stage, showed that only at 13 ss significant differences existed, being the ratio higher on the left side (Fig. 3.5 (B)). At 13 ss the number of migrating cells was significantly superior on the left side as well as the ratio per total number of cells, when compared to the other somite stages and to the right side at the same stage. Consequently, 13 ss was the time point when most active migratory behaviour occurred and it was higher on the left side of the KV.

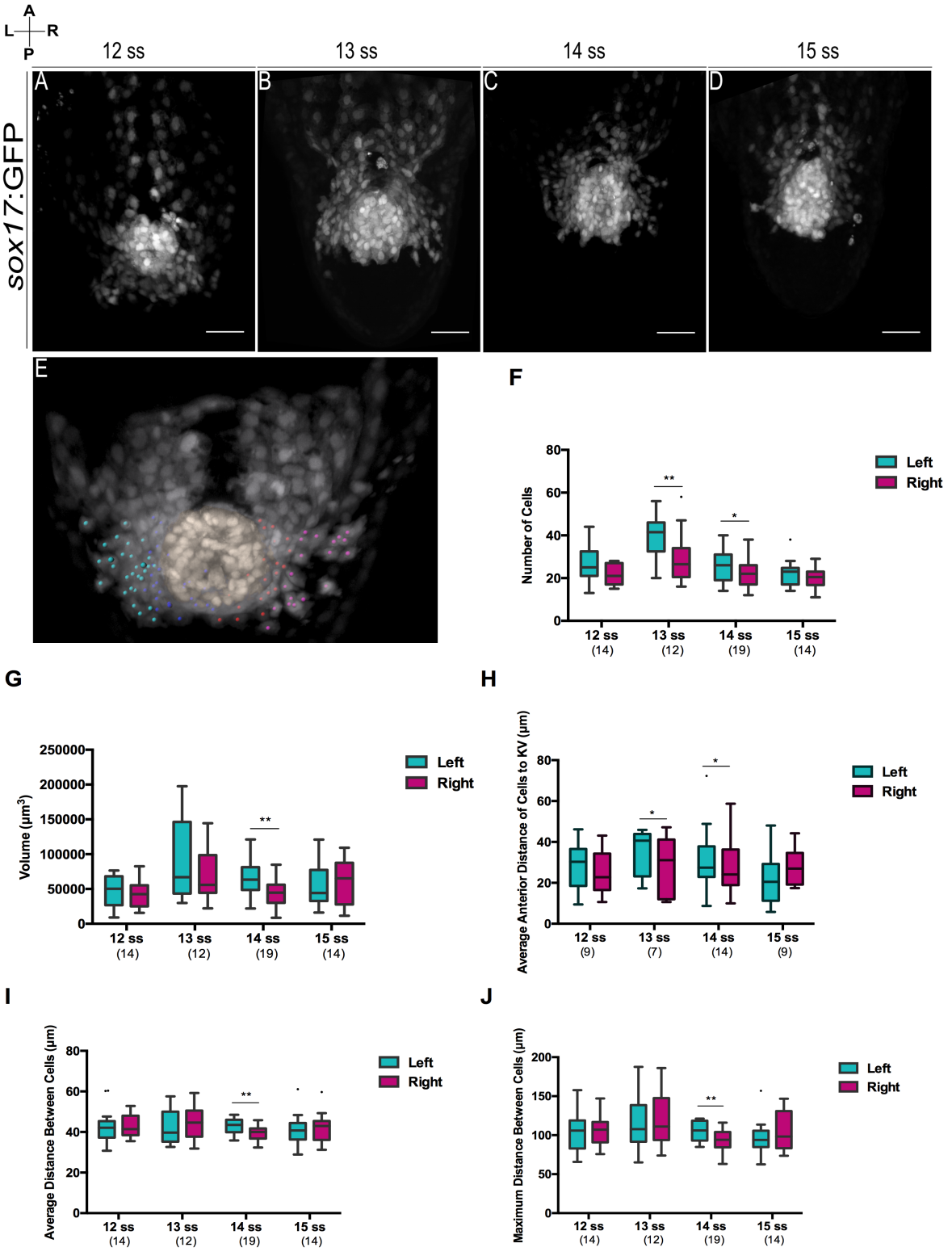

Figure 3.4 –Time course studies using fixed embryos revealed LR asymmetries. (A-D) Illustrative example of the ss covered in this analysis. MIPs of two-photon z-stacks of 12 ss **(A)**; 13 ss **(B)**; 14 ss **(C)** and 15 ss **(D)** *Tg*(*sox17:GFP*) fixed embryos. Scale bar = 100 µm. Axes are indicated: A, anterior; P, posterior; L, left; R, right. **(E)** Illustrative example of cell classification and counting using a 3D projection of a 13 ss *Tg*(*sox17:GFP*) fixed embryo. Cyan spots: Left Migrating Cells; magenta spots: Right Migrating Cells; dark blue spots: Left Non-Migrating Cells and red spots: Right Non-Migrating Cells. **(F-J)** The LR Migration parameters calculated for fixed embryos which present significant differences. Those parameters include: **(F)** The number of cells; volume occupied by the cells **(G)**; average anterior distance of the cells to the KV **(H)**; average **(I)** and maximum **(J)** distance between cells. The number of embryos analysed (N) is shown between parentheses for each somite stage. * corresponds to a p-value<0,05 and ** to a p-value<0,005. Whiskers are extended using Tukey style.

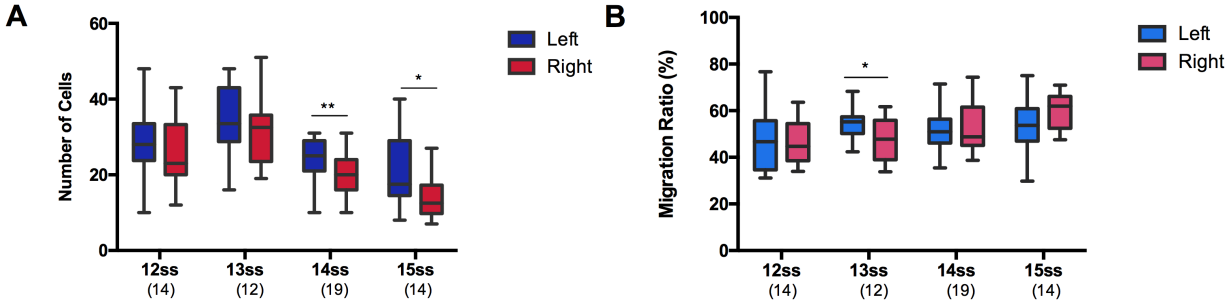

Figure 3.5 –Time course studies using fixed embryos revealed LR asymmetries in non-migrating cells. (A) Number of cells for the non-migrating cells. **(B)** The calculated migration ratio (number of migrating cells/total number of cells) is significantly higher on the left side at 13 ss. The number of embryos analysed (N) is shown between parentheses for each somite stage. * corresponds to a p-value<0,05 and ** to a p-value<0,005. Whiskers are extended using Tukey style.

3.3 - Proliferation and Cell Death Dynamics of *sox17:GFP*$^+$ cells close to the KV

When studying migratory patterns, it is important to characterize the proliferation versus apoptosis dynamics along the process. Since LR asymmetries were observed at 13 ss and 14 ss, namely the number of migrating cells, we decided to explore more about these dynamics during these developmental stages.

3.3.1 - *sox17:GFP*$^+$ cells show low levels of apoptosis and cell proliferation

To understand the LR differences in the number of cells, we analysed cell death of *sox17:GFP*$^+$ cells and specifically in the migratory region close to the KV, by performing a TUNEL assay which marks the nicked DNA, characteristic of apoptotic cells. This was done in embryos at stages 13 and 14 ss. This analysis allowed a clear visualization of the red marked apoptotic cells and co-localization to understand which *sox17:GFP*$^+$ cells were dying in the studied stages.

For both 13 (Fig. 3.6 (A-A’’’)) and 14 ss (Fig .3.6 (B-B’’’)) embryos, the number of apoptotic cells was variable as well as the number the *sox17:GFP*$^+$ cells in the region under study. The apoptotic rate was calculated as the number of total TUNEL marked cells in *sox17:GFP*$^+$ cells per the total number of *sox17:GFP*$^+$ cells. This apoptotic rate was calculated for the total number of *sox17:GFP*$^+$ cells over the studied region, and for the left and right side of the same embryo. Overall, the apoptotic rates (%) calculated for all cells, left-sided, and right-sided were quite low (Fig. 3.6 (C)), the maximum values being around the 5%, nevertheless at 13 ss this value was significantly superior on the right side (Fig. 3.5 (C)). When comparing the same sides and the category of ‘all cells’ between the two somite stages, no significant differences were found (Fig. 3.6 (D)).
In short, the percentage of apoptosis that *sox17:GFP*$^+$ cells are undergoing is considerably low and LR differences were only found at 13 ss, being greater on the right side. Even though the overall percentage of apoptosis is low, this asymmetry is interesting when considering that at 13 ss the major left-sided asymmetry was found for the number of cells. Which possibly translates in cell death being one mechanism contributing for this LR asymmetry.

Since the immunostaining for PCNA did not work despite several trials, we attempted an alternative methodology to evaluate the cell proliferation dynamics regarding these somite stages by counting the number of cells undergoing mitosis, which is described in section 2.4.3. The mitotic index, which is the ratio between the number of *sox17:GFP*$^+$ cells undergoing mitosis and the total number of *sox17:GFP*$^+$

cells, was calculated for the total number of *sox17:GFP*$^{+}$ cells over the studied region for the left and right sides in the same embryo.

The number of cells undergoing mitosis was variable. The calculated mitotic index values had a maximum of 20% (Fig. 3.6 (E)). So, when comparing with the apoptotic ratio, these are greater values, and we can infer that these *sox17:GFP*$^{+}$ cells are experiencing more proliferation than apoptosis. Regarding asymmetries, no significant differences were found between left and right sides at both 13 and 14 ss (Fig. 3.6 (E)). However, when comparing the same side between the two somite stages (Fig. 3.6 (D)), the mitotic index was higher at 13 ss than a 14 ss for the right side, for the category of 'all cells' (left sided cells plus the ones on the right side). In summary, there are more cells proliferating at 13 ss than at 14 ss, which could explain the observed diminished number of cells from 13 until 15 ss.

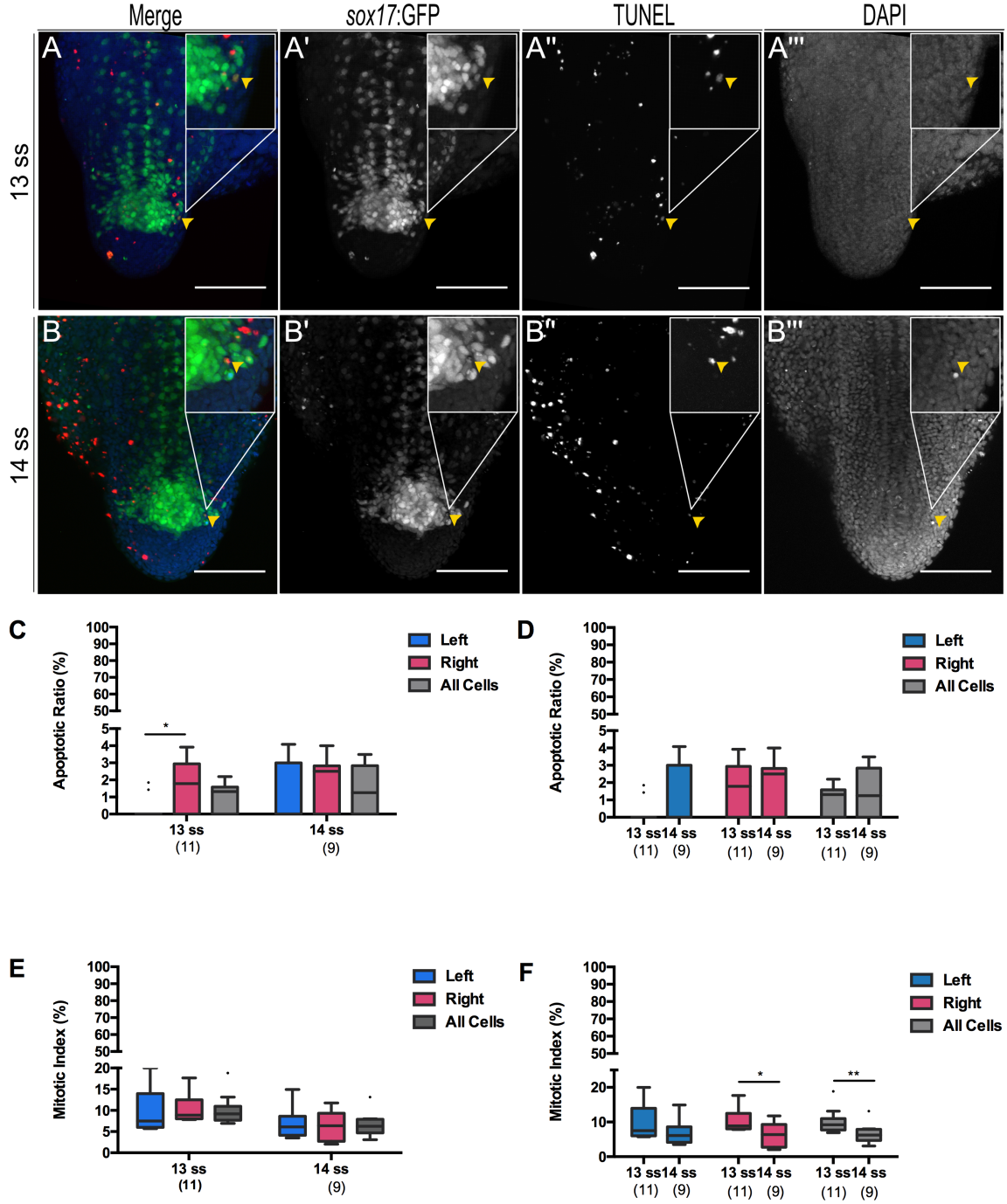

Figure 3.6 – Cell death and proliferation characterization at 13 and 14 ss. Representative two-photon z-stacks of TUNEL assays performed in 13 (A-A''') and 14 ss (B-B''') *Tg*(*sox17:GFP*) embryos. Close-up exposing cells where GFP and TUNEL overlapped (yellow arrowhead), translating in a yellow cell. **(A, B)** Blue: DAPI; green: *sox17:GFP*; red: TUNEL. DAPI **(A''', B''')**; TUNEL **(A'', B'')**; *sox17:GFP* **(A', B')**. Scale bar = 100 μm. Axes are indicated: A, anterior; P, posterior; L, left; R, right. **(C-D)** Apoptotic ratio (number of cells which are both *sox17:GFP* and TUNEL positive/ number of *sox17:GFP*$^+$ cells) calculated for left and right sides and for all cells (left plus right). Comparisons between left and right sides **(C)** and between 13 and 14 ss for the same side **(D)**. **(E-F)** Mitotic index (number of *sox17:GFP*$^+$ cells undergoing mitosis/ number of *sox17:GFP*$^+$ cells) calculated for left and right sides and for all cells (left plus right). Comparisons between left and right sides **(E)** and between 13 and 14 ss for the same side **(F)** * corresponds to a p-value<0,05 and ** to a p-value<0,005. Whiskers are extended using Tukey style.

3.4 The fate of *sox17:GFP*$^+$ cells: Kaede photoconversion and cell tracking

After assessing the migratory behaviour of the studied *sox17:GFP*$^+$ cells, and after finding that those cells showed LR asymmetries for some of the calculated migratory parameters, we then aimed to explore the fate of those cells. To do so, we injected Kaede mRNA in 1-cell *Tg(sox17:GFP)* embryos and followed the photoconverted cells throughout development until the primordial pancreatic and liver buds emerged. Kaede is a protein that acts as a green chromophore and can be irreversible converted to red by UV or violet light, being the red fluorescence intensity similar to the green one [110]. As described in section 2.3.1, we chose to perform the photoconversion in target regions defined as 'Cluster ROI' for the 8 ss embryos (Fig. 3.7 (A, B)), this region corresponds to the cluster previously reported in this study, in a time point prior to the beginning of cell migration. At 14 ss embryos, when we know that cells were actively migrating and showed some LR asymmetries, we defined two target regions, called the 'Bilateral ROIs', regarding the two groups of cells seen migrating from each side of the KV (Fig. 3.7 (A, D)). As a control for this fate assessment, we decided to photoconvert the cells of the KV (Fig. 3.7 (C)), which express *sox17:GFP* as well and were reported to incorporate the notochord, hypochord, floor plate and tail mesenchyme (Bordalo, 2015).
The images of photoconverted embryos (Fig. 3.7 (A, B)) are single confocal optical slices from several confocal z-stacks acquired right after the photoconversion. *sox17:GFP*$^+$ cells were the targeted cells for the photoconversion, so due to Kaede mRNA injection, the majority of cells presented a green fluorescence signal despite some degree of mosaicism. Sometimes green Kaede cells showing a stronger fluorescence signal were identifiable as *sox17:GFP*$^+$ cells, but this was not always the case. Consequently, even defining the targeted position, photoconvertion of some adjacent cells was expected and inevitable. Nevertheless, our assay allowed us to identify the correct cells because only the resulting yellow cells were the targeted *sox17:GFP*$^{+.}$, all the others turning red. Also, since this procedure was performed in different Z positions using a confocal microscope, cells located above and below the plane of focus were also reached by the UV laser. This is the reason why many photoconverted red cells were seen in the referred images and in the subsequent analysed time points after photoconversion.

At 48 hpf it is described that LR asymmetry is established, with the liver located on the left side and the pancreas on the right side. So, to check if at 48 hpf, any photoconverted *sox17:GFP*$^+$ cell was present at those organs we looked for yellow cells, *i.e.*, yellow cells due to expressing *sox17:GFP* and green Kaede converted to red. However, we could not observe any yellow cells there (Fig. 6.6 (A-B)) (N=10) or in any other region throughout the whole larvae (Fig. 6.6 (C-D)). We noticed that the red fluorescent signal was considerable low when compared to green one or even absent in some of the analysed larvae. Moreover, after three attempts, we concluded that the red fluorescent signal was lost in the majority of the cases when the samples were fixed prior to imaging, making it not a reliable approach, thus we decided to perform imaging with live anesthetised samples. Consequently, we changed our approach and attempted to monitor photoconverted embryos over small periods of time, such as, 5h (N=3) and 10h (N=4) after conversion (Fig. 3.7 (E-E'', F-F'')), which we succeeded since yellow cells are observed

in both time points and red fluorescence signal is still strong. Regarding these analysed samples, we did not find any yellow cells at the gut tube, as these yellow cells were only located at the tail of the embryos (Fig. 3.7 (E-E'', F-F'')), in final positions suggesting somite localization.

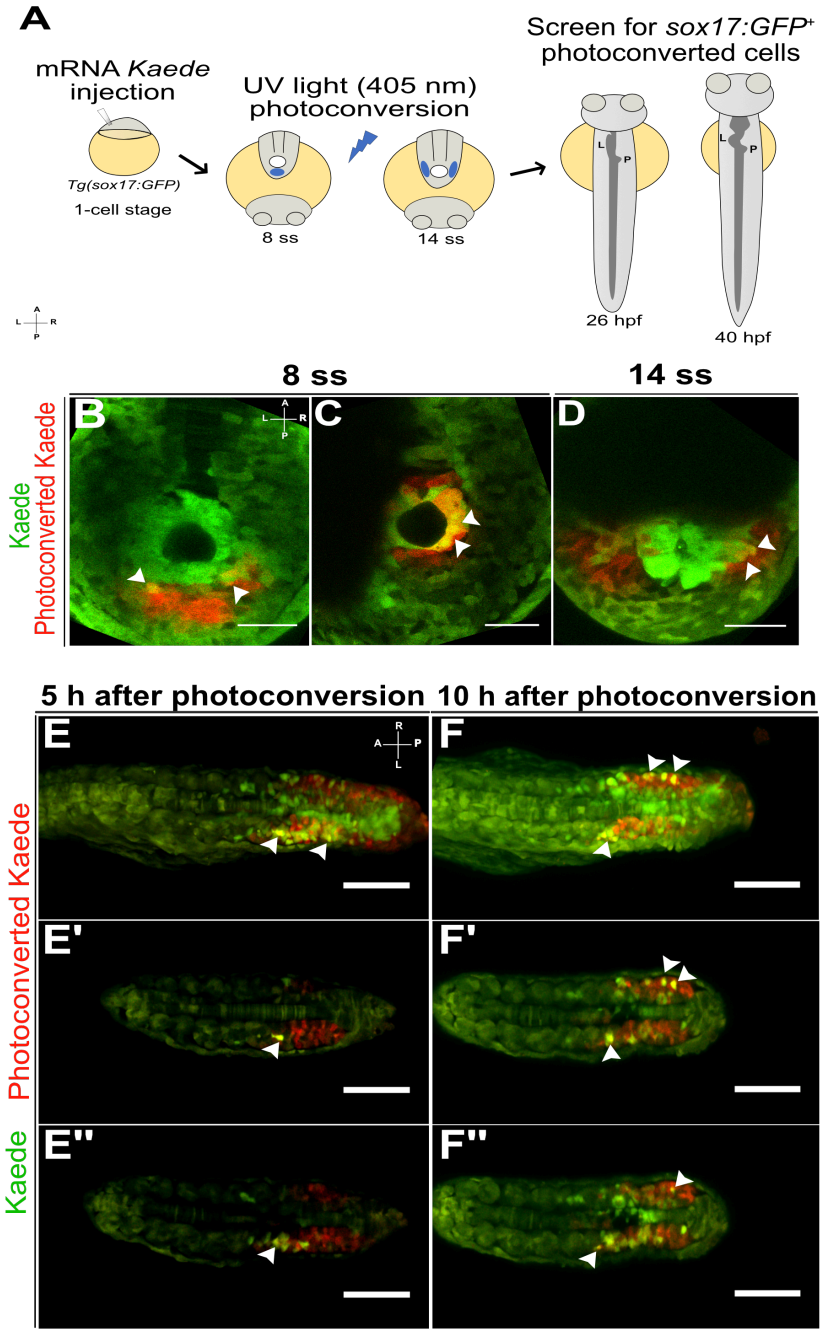

Figure 3.7 – Following *sox17:GFP*⁺ cells fate using *Kaede* photoconversion. **(A)** Schematic illustration of the experimental outline of the *Kaede* mRNA microinjection, photoconversion and screen for photoconverted cells at 26 hpf and 40 hpf. *Kaede* mRNA was injected in one-cell stage *Tg*(*sox17:GFP*) embryos. At 8 and 14 ss, target regions (blue regions) defined as 'Cluster ROI' and 'Bilateral ROIs' for 8 and 14 ss, respectively. were photoconverted using a UV laser, the 'cluster' and 'bilateral clusters', respectively. Later the embryos were screened for the localization of yellow cells, which correspond to *sox17:GFP*⁺ photoconverted *Kaede* cells. **(B-D)** Confocal optical sections of *Tg*(*sox17:GFP*) embryos injected with *Kaede* mRNA right after photoconversion at 8 ss **(B-C)** and 14 ss **(D).** As a control, KV cells were photoconverted as well **(C)**, since their fate is already known. Yellow cells correspond to *sox17:GFP*⁺ and photoconverted *Kaede* cells. Scale bar = 50 µm. **(E-F)** Assessment for photoconverted cells presence and position at 5 **(E-E'')** and 10 h **(F-F'')** after photoconversion. Two-photon Z projections **(E, F)**, and representative optical sections from two-photon z-stacks of the tails, where red and yellow cells are present **(E'-E'', F'-F'')**. White arrowheads: yellow cells, *sox17:GFP*⁺and photoconverted *Kaede* cells. Scale bar = 100 µm. Axes are indicated: A, anterior; P, posterior; L, left; R, right.

Continuing using live samples, we wanted to assess if red fluorescence signal and yellow cells were still present at 26 hpf, where the first pancreatic bud has already emerged although the liver has not, but a thickness is already present in the region where it will emerge. Additionally, this is a developmental stage prior to the onset of the gut looping, thus a good timing to check if the converted *sox17:GFP*$^{+}$ cells had incorporated the formed gut.

However, this was not the case, since we could not observe any yellow cells at the first pancreatic bud or the gut thickness from where the liver bud would start emerging at 26 hpf (Fig. 3.8 (G)). For illustrative purposes, the same region is shown for a 26 hpf *Tg(sox17:GFP).* As observed in prior time points, the yellow cells only appear confined to the region of the tail (Fig.3.8 (I-I'')). The same is observed for the red photoconverted cells, meaning that any other cells we had photoconverted appeared to stay located at this region. Regarding the control performed by photoconverting the KV cells (Fig. 3.6 (C)), at 26 hpf, we could tell yellow cells were present at the notochord (Fig. 3.8 (J-J'')), one of the known fates of these cells, translating in a positive control for this assay.

We attempted to test if the scenario could be different when imaging the larva at 40 hpf, which could have been interesting, because the liver bud would already be present as well. Nonetheless, the results were similar as the one obtained for 26 hpf, meaning no yellow cells were present at the analysed embryos (N=11) (images not shown). Notwithstanding, we could still observe red fluorescence signal and even yellow cells at the tail (Fig. 3.8 (K-K'''')). Surprisingly, in one of the analysed embryos, we identified two yellow cells, which by using orthogonal views (Fig. 3.8 (K''')) appeared to be located in the gut. Those cells appeared to be located bellow the notochord, in a region suggestive of the gut tube structure. Yet, these results are inconclusive and further analysis and replication of this procedure is required. Again, for illustrative purposes, the tail region is shown for a 40 hpf *Tg(sox17:GFP)* (Fig. 3.8 (L-L'')), where even cells located at the notochord were observed, which is in agreement with the results of Bordalo (2015) **[111]** as well as with our results obtained for the KV photoconversion control.

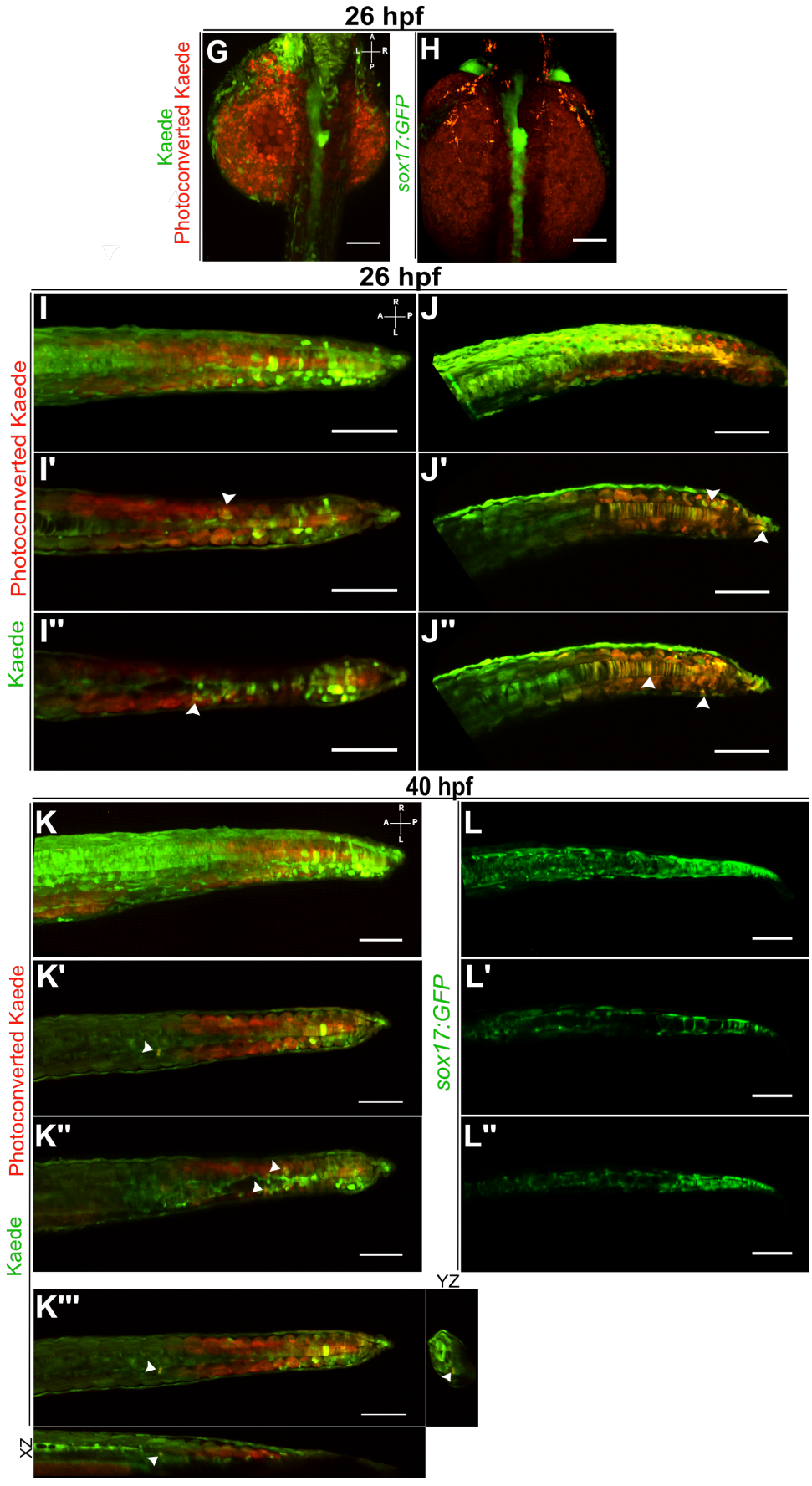
26 hpf
G
H
Kaede
Photoconverted Kaede
sox17:GFP
26 hpf
I
J
I'
J'
I''
J''
Photoconverted Kaede
Kaede
40 hpf
K
L
K'
L'
K''
L''
K'''
YZ
XZ
Photoconverted Kaede
Kaede
sox17:GFP

Figure 3.8 – Following *sox17:GFP*$^{+}$ cell fate using *Kaede* photoconversion at 26 hpf and 40 hpf. Assessment for photoconverted cells presence and position at 26 **(G; I-J'')** and 40 h **(K-K''')** after photoconversion. **(G)** Two-photon Z projection of a dorsal view of the pancreas dorsal bud and the thick region where the liver bud will emerge from on the left side in photoconverted *Tg*(*sox17:GFP*) embryo. No yellow or red cells were found in at 26 hpf in this region**. (H)** Two-photon Z projection of the same region in a not injected *Tg*(*sox17:GFP*) embryo. Two-photon Z projections (**I; J**), and representative optical sections from two-photon z-stacks of the tails, where red and yellow cells are present **(I'-I'', J'-J'')**. **(J-J'')** Tail of one of the control embryos, where the KV cells were photoconverted. As expected, yellow cells are present at the notochord **(J'')** one of the fates of the once KV cells. White arrowheads: yellow cells, *sox17:GFP*$^{+}$ and photoconverted *Kaede* cells. **(K)** Two-photon Z projection from a dorsal view of the tail region of a 40 hpf photoconverted *Tg*(*sox17:GFP*). and representative optical sections from two-photon z-stacks of the tails, where red and yellow cells are present **(K'-K''). (K''')** Orthogonal views XY and XZ, suggest the yellow cells seen in the **(K')** optical section may be located in the gut tube. **(L-L'')** Imaging of a *Tg*(*sox17:GFP*) embryo tail with 40 hpf. **(L)** Two-photon Z projection of a dorsal view of the tail and representative two-photon optical sections **(L'-L'')** where the gut tube is observed in **(L'')**. Scale bar = 100 μm. Axes are indicated: A, anterior; P, posterior; L, left; R, right.

4. Discussion

Understanding LR patterning in vertebrates provides interesting knowledge both in a developmental and evolutionary biology perspectives. The mechanisms involved in anomalies of LR axis determination lead to a spectrum of congenital disorders in humans that affect both arrangement and morphology of the heart and visceral organs. Thus, a clinical relevance is present when studying LR determination. Still, the molecular mechanisms proposed to explain laterality remain patchy and do not fully explain the whole process from fluid-flow biophysical cues to final positioning of the organs.

In this dissertation, we aimed to study a possible yet alternative mechanism in which LR asymmetric cues that take place in the KV cells could affect gut formation. Namely, we wanted to investigate if *dand5* right-sided asymmetric expression pattern could be affecting the neighbouring gut precursor cells by influencing their migratory behaviour in a potential asymmetric way. So, first, we needed to test whether there was an asymmetric migration of gut precursor cells with a left-right bias.

4.1 – *sox17:GFP*$^{+}$ cells form a cluster located posteriorly to the KV

We reported the formation of an aggregate of *sox17:GFP*$^{+}$ cells that we called 'the cluster' located posterior to the KV. This cluster was the origin from which *sox17:GFP*$^{+}$ cells later migrated towards the anterior side of the embryo. This finding is in agreement with the current knowledge that gut endoderm cells merge at the midline, a migration that is completed around 18 ss to form the gut tube **[84]**. However the question remains why this cluster is formed and why the cells seem to migrate only when the KV moves over the cluster, instead of just rearranging in the medial region like the other *sox17:GFP*$^{+}$ involved in establishing the gut. We were able to estimate the average number of 42 cells composing the cluster at 10 ss, a developmental stage immediately before migration initiation. This finding is interesting when comparing to the number of cells on each side of the KV during later migratory stages. For example, at 13 ss, the time point that presented the largest number of migrating cells and with a greater statistical significance regarding the asymmetric L>R distribution, we counted the presence of 40 and 30 cells, on the left and right sides, respectively. This suggests that if we assume that all the migrating cells came from the cluster, several cell divisions must have occurred between the two time points. Additionally, taking into account that the average number of non-migrating cells was 30 cells on each side, the number of cell divisions needed to occur increases even more. Since no cell proliferation assay was performed between the two events, the cluster presence prior to migration; and migration onset, we cannot demonstrate it.

4.2 – Characterization of *sox17:GFP*$^{+}$ cells migration pattern

Unfortunately, as indicated in section 3.1.2, we could not infer any asymmetric differences in *sox17:GFP*$^{+}$ cells migratory behaviours by live imaging. Since the p-values were large our data did not allow a significant conclusion that the overall medians differ. It is possible that in fact no differences were present, however a more plausible explanation can reside in the fact that our sample size was too small, and the Wilcoxon test has little power to detect small differences in small sample size cases, a sample size at least equal to 10 is recommended and ours was equal to 7 (despite having filmed 16 embryos). Nonetheless, we extracted important measurements from the tracking data, since we had no previous knowledge concerning these cells migratory behaviour. Although not significant, our measurements appeared to detect a left-sided asymmetry, by presenting larger values for track displacement, length and speed. Still, we cannot exclude the possibility of not having performed a

complete drift correction of intrinsic embryo movements additional to the KV movement. Together with the small number of suitable videos for cell tracking, we suggest that this analysis should be repeated with the required tools, such as using the 1% LMA concentration and the use of anaesthesia in advance to prevent unwanted movements, to produce suitable videos for cell tracking, allowing to increase the sample size.

In contrast, the analysis of fixed embryos yielded reliable results because the number of embryos analysed for each somite stage corresponded to a good sample size required to perform statistical analysis. In addition, the higher resolution in Z, compared to the time-lapse videos, allowed a good characterization of cell positions thereby permitting to calculate many distance parameters. These same parameters would have not been possible by live-imaging, at least with the same degree of resolution, since we were able to cover every *sox17:GFP*$^{+}$ cell at the studied region on each fixed embryo. Moreover, we were able to identify LR asymmetries. These results suggested that at 13 ss, more cells were migrating on the left side, which is supported by the difference in detected apoptosis between left and right sides. At 14 ss the same asymmetry concerning the number of cells, together with a larger dispersion of cells and Posterior-Anterior distance to KV was observed on the left side. Even though using consecutive developmental stages of fixed embryos yielded consistent information to infer about migration live imaging should not be disregarded but instead it should be taken together as both studies are complementary. Once again, we emphasize the importance of repeating live studies.

4.3 – Assessing the fate of *sox17:GFP*$^{+}$ cells

Our aim with the photoconversion experiments was to test if the migratory *sox17:GFP*$^{+}$ cells we were studying, were in fact incorporating the gut tube later in development. However, our attempts to assess *sox17:GFP*$^{+}$ cell fate using Kaede photoconversion did not yield results that allow us to take such conclusions. Mainly because this study required optimization of numerous parameters, and after several trials attempting to overcome various problems, the overall N for each experiment was not large enough. Nevertheless, we did locate yellow cells over time, and it was possible to validate the technique by confirming the known fate of KV cells. Still, by time-lapse imaging we did observe a few migrating cells incorporating the arising gut. So, a possible explanation for the rarity of this event resides in the fact that cell proliferation can dilute photoconverted Kaede with newly synthetized non photoconverted Kaede, making it difficult to detect red fluorescence after few cell divisions **[112]**. Given that we detected cell proliferation between 13 and 14 stages we can infer that between the photoconversion and the analysed subsequent developmental stages, (total of 13-27 hours) many more *sox17:GFP*$^{+}$ cell divisions might have occurred. In summary, we can conclude the strategy designed to detect yellow cells worked well, but that unforeseen cell divisions diluted the red Kaede in a way that was no longer possible to follow the desired target cells because they were no longer yellow.
We do not discard the possibility of performing future studies using photoconvertible proteins (FPs), to understand the fate of these cells. Thus, we suggest using other FP, the Kikume (KikGR) **[113]**. Kikume can be photoconverted from green to red by multiphoton excitation with a 750 nm wavelength, avoiding the confocal drawbacks we previously referred and in a much brighter way than Kaede **[114]**.

The origin of liver progenitor cells in zebrafish could be explained by the information provided by two key hepatoblast markers, the transcription factors *hhex* **[115]** and *prox1* **[116,117]**. These are detectable in the endodermal region that later will give rise to the liver bud, suggesting that the liver progenitor cells come from the endoderm cells, which later differentiate to form the liver in that region after the endoderm rod formation takes place. This idea is supported by data from anatomic studies **[87,86]** plus by studies regarding mutants associated to the liver development **[117,118]**. However, another

perspective was stated by Korzh, *et al.*, 2001 **[119]** hypothesizing that liver progenitors could be differentiated before gut tube morphogenesis and that the liver bud would be formed later by migration and aggregation of these liver differentiated cells. This idea relied in the fact that the liver specific marker *cp* is detected in the endoderm as early as 16 hpf (14 ss), which is earlier than the beginning of the liver morphogenesis around 28 hpf. However, solid evidence that early *cp* positive cells do contribute to the formation of liver bud was never demonstrated **[99]**.

In contrast to Korzh *et al.*, (2001)**[119]** theory, we were not testing if the liver differentiated cells emerged before or after the liver bud formation, instead, we were hypothesizing that the endoderm cells present on the left side of the KV, the same ones that we found to be more anteriorly positioned than their right-sided counterparts, could be the ones that upon incorporating the arising gut, would become the liver or the pancreatic bud, these being the two asymmetric gut organs.

4.4– Final remarks and future studies

We conclude that we have fulfilled our main objective of characterizing asymmetric positions of *sox17:GFP*$^{+}$ cells. We showed the presence of LR asymmetries by time-course analysis on fixed embryos. Therefore, this work validates our initial hypothesis of migration being affected asymmetrically. The explanation we reasoned for this asymmetry was based on the asymmetric *dand5* expression, which allegedly is responsible for the asymmetric expression of Spaw protein in cells surrounding the KV and later in the LPM. This Spaw asymmetry was hypothesized to interfere with the cell motility of the studied cells, since previous studies showed its role in manipulating migration speed, namely in endodermal cells **[100,102,105]**. Indeed, it was reported before that endodermal cells that are exposed to more Nodal tend to migrate faster **[105]**. So, we reason that the more anteriorly positioned left sided cells we detected here in this study were more exposed to Spaw due to less inhibition by Dand5 protein on the left side. Therefore, the next step in future studies is to manipulate LR signals within the KV in order to test if the observed asymmetries are indeed originated from R>L *dand5* asymmetric expression. One way to test it would be to inject a Pkd2 Morpholino (MO) in the *Tg(sox17:GFP)* reporter line embryos and replicate the methodology used in this thesis project, using both fixed and live embryos, to asses for differences. This Pkd2 MO leads to 62% of symmetrical *dand5* expression, 23 % of normal R>L and 15 % of inverted asymmetry L>R, confirmed by our recent results (unpublished results from Raquel Jacinto). Similar published results were also seen before by Bisgrove *et al*., (2005) **[58]** and Schottenfeld *et al.*, (2007) **[57]**. So, we would expect to find around 60% of embryos without asymmetric LR differences regarding migratory *sox17:GFP*$^{+}$ cells.

5. References

1. Levin M, Klar AJS, Ramsdell AF, Levin M, Ramsdell AF. Introduction to provocative questions in left – right asymmetry. 2016; doi:10.1098/rstb.2015.0399
2. Hamada H. Breakthroughs and future challenges in left-right patterning. Dev Growth Differ. 2008;50. doi:10.1111/j.1440-169X.2008.01008.x
3. Grimes DT, Burdine RD. Left-Right Patterning: Breaking Symmetry to Asymmetric Morphogenesis. Trends Genet. Elsevier Ltd; 2017;33: 616–628. doi:10.1016/j.tig.2017.06.004
4. Blum M, Feistel K, Thumberger T, Schweickert A. The evolution and conservation of left-right patterning mechanisms. Development. 2014;141: 1603–1613. doi:10.1242/dev.100560
5. Kilner PJ, Yang GZ, Wilkes AJ, Mohiaddin RH, Firmin DN, Yacoub MH. Asymmetric redirection of flow through the heart. Nature. 2000;404: 759–61. doi:10.1038/35008075
6. Pedrizzetti G. Nature Optimizes the Swirling Flow in the Human Left Ventricle. 2005;108101: 1–4. doi:10.1103/PhysRevLett.95.108101
7. Levin M. Is the early left-right axis like a plant, a kidney, or a neuron? The integration of physiological signals in embryonic asymmetry. Birth Defects Res Part C - Embryo Today Rev. 2006;78: 191–223. doi:10.1002/bdrc.20078
8. Lin AE, Ticho BS, Houde K, Westgate M-N, Holmes LB. Heterotaxy: Associated conditions and hospital-based prevalence in newborns. Genet Med. 2000;2: 157–172. doi:10.1097/00125817-200005000-00002
9. Fliegauf M, Benzing T, Omran H. When cilia go bad : cilia defects and ciliopathies. 2007;8. doi:10.1038/nrm2278
10. Fakhro KA, Choi M, Ware SM, Belmont JW, Towbin JA, Lifton RP. Rare copy number variations in congenital heart disease patients identify unique genes in left-right patterning. 2011; doi:10.1073/pnas.1019645108
11. Levin M, Johnson RL, Sterna CD, Kuehn M, Tabin C. A molecular pathway determining left-right asymmetry in chick embryogenesis. Cell. 1995;82: 803–814. doi:10.1016/0092-8674(95)90477-8
12. Collignon J, Varlet I, Robertson EJ. Relationship between asymmetric nodal expression and the direction of embryonic turning [Internet]. Nature. 1996. pp. 155–158. doi:10.1038/381155a0
13. Schweickert A, Weber T, Beyer T, Vick P, Bogusch S, Feistel K, et al. Report Cilia-Driven Leftward Flow Determines Laterality in Xenopus. 2007; 60–66. doi:10.1016/j.cub.2006.10.067
14. Hojo M, Takashima S, Kobayashi D, Sumeragi A, Shimada A, Tsukahara T, et al. Right-elevated expression of charon is regulated by fluid flow in medaka Kupffer ' s vesicle. 2007; 395–405. doi:10.1111/j.1440-169x.2007.00937.x
15. Essner JJ. Kupffer's vesicle is a ciliated organ of asymmetry in the zebrafish embryo that initiates left-right development of the brain, heart and gut. Development. 2005;132: 1247–1260. doi:10.1242/dev.01663
16. Schröder SS, Weizbauer A. Paraxial Nodal Expression Reveals a Novel Conserved Structure of the Left-Right Organizer in Four Mammalian Species. 2016; 77–87. doi:10.1159/000440951
17. Bangs F, Antonio N, Thongnuek P, Welten M, Davey MG, Briscoe J. Generation of mice with functional inactivation of talpid3 , a gene first identified in chicken. 2011;3272: 3261–3272. doi:10.1242/dev.063602
18. Stephen LA, Davis GM, Katie EMC, James J, Lynn MC, Kierans M, et al. Failure of Centrosome Migration Causes a Loss of Motile Cilia in talpid 3 Mutants. 2013; 923–931. doi:10.1002/dvdy.23980
19. Yin Y, Bangs F, Paton IR, Prescott A, James J, Davey MG, et al. The Talpid3 gene (KIAA0586) encodes a centrosomal protein that is essential for primary cilia formation. 2009;664: 655–664. doi:10.1242/dev.028464
20. Gros J, Feistel K, Viebahn C, Blum M, Tabin CJ. Cell movements at Hensen's node establish left/right asymmetric gene expression in the chick. Science (80-). American Association for the Advancement of Science; 2009;324: 941–944.
21. Aw S, Koster JC, Pearson W, Nichols CG, Shi N, Carneiro K, et al. The ATP-sensitive K + -channel (K ATP) controls early left – right patterning in Xenopus and chick embryos. Dev Biol.

Elsevier Inc.; 2010;346: 39–53. doi:10.1016/j.ydbio.2010.07.011
22. Dasgupta A, Amack JD. Cilia in vertebrate left?right patterning. Philos Trans R Soc B Biol Sci. 2016;371: 20150410. doi:10.1098/rstb.2015.0410
23. Pedersen H, Mygind N. Absence of axonemal arms in nasal mucosa cilia in Kartagener's syndrome. Nature. 1976;262: 494–5. doi:10.1038/262494a0
24. Afzelius BA. A human syndrome caused by immotile cilia. Science (80-). American Association for the Advancement of Science; 1976;193: 317–319.
25. Li Y, Yagi H, Onuoha EO, Damerla RR, Francis R, Furutani Y, et al. DNAH6 and Its Interactions with PCD Genes in Heterotaxy and Primary Ciliary Dyskinesia. PLoS Genet. 2016;12: 1–20. doi:10.1371/journal.pgen.1005821
26. Kennedy MP, Omran H, Leigh MW, Dell S, Morgan L, Molina PL, et al. Congenital heart disease and other heterotaxic defects in a large cohort of patients with primary ciliary dyskinesia. Circulation. 2007;115: 2814–2821. doi:10.1161/CIRCULATIONAHA.106.649038
27. Sutherland MJ, Ware SM. Disorders of left-right asymmetry: Heterotaxy and situs inversus. Am J Med Genet Part C Semin Med Genet. 2009;151: 307–317. doi:10.1002/ajmg.c.30228
28. Knowles MR, Daniels LA, Davis SD, Zariwala MA, Leigh MW. Primary ciliary dyskinesia. Recent advances in diagnostics, genetics, and characterization of clinical disease. Am J Respir Crit Care Med. Am Thoracic Soc; 2013;188: 913–922.
29. Praveen K, Davis EE, Katsanis N. Unique among ciliopathies: primary ciliary dyskinesia, a motile cilia disorder. F1000Prime Rep. Faculty of 1000 Ltd; 2015;7.
30. Amack JD, Yost HJ. The T Box Transcription Factor No Tail in Ciliated Cells Controls Zebrafish Left-Right Asymmetry. 2004;14: 685–690. doi:10.1016/j
31. Cooper MS, Amico LAD. A Cluster of Noninvoluting Endocytic Cells at the Margin of the Zebrafish Blastoderm Marks the Site of Embryonic Shield Formation. 1996;198: 184–198.
32. Oteíza P, Köppen M, Concha ML, Heisenberg C-P. Origin and shaping of the laterality organ in zebrafish. Development. 2008;135: 2807–13. doi:10.1242/dev.022228
33. Matsui T, Ishikawa H, Bessho Y. Cell collectivity regulation within migrating cell cluster during Kupffer's vesicle formation in zebrafish. Front cell Dev Biol. 2015;3: 27. doi:10.3389/fcell.2015.00027
34. Gokey JJ, Ji Y, Tay HG, Litts B, Amack JD. Kupffer's vesicle size threshold for robust left-right patterning of the zebrafish embryo. Dev Dyn. 2016;245: 22–33. doi:10.1002/dvdy.24355
35. Lin C, Tsai M, Liu Y, Lu Y, Chen Y, Lai Y, et al. Klf8 regulates left-right asymmetric patterning through modulation of Kupffer ' s vesicle morphogenesis and spaw expression. Journal of Biomedical Science; 2017; 1–14. doi:10.1186/s12929-017-0351-y
36. Navis A, Marjoram L, Bagnat M. Cftr controls lumen expansion and function of Kupffer ' s vesicle in zebrafish. 2013;1712: 1703–1712. doi:10.1242/dev.091819
37. Roxo-rosa M, Jacinto R, Sampaio P, Lopes SS. The zebrafish Kupffer ' s vesicle as a model system for the molecular mechanisms by which the lack of Polycystin-2 leads to stimulation of CFTR. 2015; 1356–1366. doi:10.1242/bio.014076
38. Callol-massot C, Izpisu JC. Regulation of primary cilia formation and left-right patterning in zebrafish by a noncanonical Wnt signaling mediator , duboraya. 2006;38: 1316–1322. doi:10.1038/ng1892
39. Kim J, Bae S, Lee HS, Park J, Kim K. Claudin5a is required for proper inflation of Kupffer ' s vesicle lumen and organ laterality. 2017; 1–18.
40. Kreiling JA, Prabhat, Williams G, Creton R. Analysis of Kupffer's vesicle in zebrafish embryos using a cave automated virtual environment. Dev Dyn. 2007;236: 1963–1969. doi:10.1002/dvdy.21191
41. Compagnon J, Barone V, Rajshekar S, Kottmeier R, Pranjic-ferscha K, Behrndt M, et al. Short Article The Notochord Breaks Bilateral Symmetry by Controlling Cell Shapes in the Zebrafish Laterality Organ. Dev Cell. Elsevier Inc.; 2014;31: 774–783. doi:10.1016/j.devcel.2014.11.003
42. Wang G, Manning ML, Amack JD. Regional cell shape changes control form and function of Kupffer ' s vesicle in the zebrafish embryo. Dev Biol. Elsevier; 2012;370: 52–62. doi:10.1016/j.ydbio.2012.07.019
43. Wang G, Cadwallader AB, Jang DS, Tsang M, Yost HJ, Amack JD. The Rho kinase Rock2b establishes anteroposterior asymmetry of the ciliated Kupffer ' s vesicle in zebrafish. 2011;54:

45–54. doi:10.1242/dev.052985
44. Cartwright JHE, Piro O, Tuval I. Fluid-dynamical basis of the embryonic development of left-right asymmetry in vertebrates. Proc Natl Acad Sci. 2004;101: 7234–7239. doi:10.1073/pnas.0402001101
45. Cartwright JHE, Piro N, Piro O, Tuval I. Embryonic nodal flow and the dynamics of nodal vesicular parcels. J R Soc Interface. 2007;4: 49–55. doi:10.1098/rsif.2006.0155
46. Nonaka S, Yoshiba S, Watanabe D, Ikeuchi S, Goto T, Marshall WF, et al. De novo formation of left-right asymmetry by posterior tilt of nodal cilia. PLoS Biol. 2005;3. doi:10.1371/journal.pbio.0030268
47. Supatto W, Fraser SE, Vermot J. An All-Optical Approach for Probing Microscopic Flows in Living Embryos. Biophys J. Elsevier; 2008;95: L29–L31. doi:10.1529/biophysj.108.137786
48. Smith DJ, Montenegro-Johnson TD, Lopes SS. Organized chaos in Kupffer's vesicle: how a heterogeneous structure achieves consistent left-right patterning. Bioarchitecture. 2014;4: 119–125. doi:10.4161/19490992.2014.956593
49. Sampaio P, Ferreira RR, Guerrero A, Pintado P, Tavares B, Amaro J, et al. Left-right organizer flow dynamics: How much cilia activity reliably yields laterality? Dev Cell. 2014;29: 716–728. doi:10.1016/j.devcel.2014.04.030
50. Tavares B, Jacinto R, Sampaio P, Pestana S, Gardner R, Lopes T, et al. Notch / Her12 signalling modulates , motile / immotile cilia ratio downstream of Foxj1a in zebrafish left-right organizer. 2017;5: 1–26.
51. Yoshiba S, Shiratori H, Kuo IY, Kawasumi A, Shinohara K, Nonaka S, et al. Cilia at the node of mouse embryos sense fluid flow for left-right determination via Pkd2. Science (80-). American Association for the Advancement of Science; 2012;338: 226–231.
52. Pintado P, Sampaio P, Tavares B, Smith DJ, Lopes SS. Dynamics of cilia length in left – right development. 2017;
53. Lopes SS, Lourenco R, Pacheco L, Moreno N, Kreiling J, Saude L. Notch signalling regulates left-right asymmetry through ciliary length control. Development. 2010;137: 3625–3632. doi:10.1242/dev.054452
54. Ferreira RR, Vermot J. The balancing roles of mechanical forces during left-right patterning and asymmetric morphogenesis. Mech Dev. Elsevier B.V.; 2017;144: 71–80. doi:10.1016/j.mod.2016.11.001
55. Francescatto L, Rothschild SC, Myers AL, Tombes RM, Amack JD, Wang X, et al. The activation of membrane targeted CaMK-II in the zebrafish Kupffer's vesicle is required for left-right asymmetry. Development. 2010;137: 2753–62. doi:10.1242/dev.049627
56. Sarmah B, Latimer AJ, Appel B, Wente SR. Inositol polyphosphates regulate zebrafish left-right asymmetry. Dev Cell. 2005;9: 133–145. doi:10.1016/j.devcel.2005.05.002
57. Schottenfeld J, Sullivan-brown J, Burdine RD. Zebrafish curly up encodes a Pkd2 ortholog that restricts left- side-specific expression of southpaw. 2007;1615: 1605–1615. doi:10.1242/dev.02827
58. Bisgrove BW, Snarr BS, Emrazian A, Yost HJ. Polaris and Polycystin-2 in dorsal forerunner cells and Kupffer's vesicle are required for specification of the zebrafish left-right axis. Dev Biol. 2005;287: 274–288. doi:10.1016/j.ydbio.2005.08.047
59. Yuan S, Zhao L, Brueckner M, Sun Z. Intraciliary calcium oscillations initiate vertebrate left-right asymmetry. Curr Biol. Elsevier Ltd; 2015;25: 556–567. doi:10.1016/j.cub.2014.12.051
60. Huang S, Xu W, Su B, Luo L. Distinct mechanisms determine organ left-right asymmetry patterning in an uncoupled way. BioEssays. 2014;36: 293–304. doi:10.1002/bies.201300128
61. Schier AF. Nodal Signaling in Vertebrate Development. Annu Rev Cell Dev Biol. 2003;19: 589–621. doi:10.1146/annurev.cellbio.19.041603.094522
62. Zinski J, Tajer B, Mullins MC. TGF-β Family Signaling in Early Vertebrate Development. Cold Spring Harb Perspect Biol. Cold Spring Harbor Lab; 2017; a033274.
63. Schier AF, Shen MM. Nodal signalling in vertebrate development. Nature. 2000;403: 385–389. doi:10.1038/35000126
64. Long S. The zebrafish nodal-related gene southpaw is required for visceral and diencephalic left-right asymmetry. Development. 2003;130: 2303–2316. doi:10.1242/dev.00436
65. Hashimoto H, Rebagliati M, Ahmad N, Muraoka O, Kurokawa T, Hibi M, et al. The

Cerberus/Dan-family protein Charon is a negative regulator of Nodal signaling during left-right patterning in zebrafish. Development. 2004;131: 1741–53. doi:10.1242/dev.01070
66. Peterson AG, Wang X, Joseph Yost H. Dvr1 transfers left-right asymmetric signals from Kupffer's vesicle to lateral plate mesoderm in zebrafish. Dev Biol. Elsevier; 2013;382: 198–208. doi:10.1016/j.ydbio.2013.06.011
67. Wang X, Yost HJ. Initiation and propagation of posterior to anterior (PA) waves in zebrafish left–right development. Dev Dyn. Wiley Online Library; 2008;237: 3640–3647.
68. Yoshioka H, Meno C, Koshiba K, Sugihara M, Itoh H, Ishimaru Y, et al. Pitx2, a bicoid-type homeobox gene, is involved in a lefty-signaling pathway in determination of left-right asymmetry. Cell. 1998;94: 299–305. doi:10.1016/S0092-8674(00)81473-7
69. Ji Y, Buel SM, Amack JD. Mutations in zebrafish pitx2 model congenital malformations in Axenfeld-Rieger syndrome but do not disrupt left-right placement of visceral organs. Dev Biol. Elsevier; 2016;416: 69–81. doi:10.1016/j.ydbio.2016.06.010
70. Piedra ME, Icardo JM, Albajar M, Rodriguez-rey JC, Ros MA. Pitx2 Participates in the Late Phase of the Pathway Controlling Left-Right Asymmetry. 1998;94: 319–324.
71. Campione M, Steinbeisser H, Schweickert A, Deissler K, Bebber F Van, Lowe LA, et al. The homeobox gene Pitx2 : mediator of asymmetric left-right signaling in vertebrate heart and gut looping. 1999;1234: 1225–1234.
72. Yonei-tamura S, Tamura K, Ryan AK, Blumberg B, Sabbagh W, Greenwald J, et al. Pitx2 determines left – right asymmetry of internal organs in vertebrates. 1998; 545–551.
73. Cheng SK, Olale F, Brivanlou AH, Schier AF. Lefty blocks a subset of TGFβ signals by antagonizing EGF-CFC coreceptors. PLoS Biol. 2004;2. doi:10.1371/journal.pbio.0020030
74. Reissmann E, Jörnvall H, Blokzijl A, Andersson O, Chang C, Minchiotti G, et al. The orphan receptor ALK7 and the Activin receptor ALK4 mediate signaling by Nodal proteins during vertebrate development. Genes Dev. 2001;15: 2010–2022. doi:10.1101/gad.201801
75. Yeo CY, Whitman M. Nodal signals to Smads through Cripto-dependent and Cripto-independent mechanisms. Mol Cell. 2001;7: 949–957. doi:10.1016/S1097-2765(01)00249-0
76. Chocron S, Verhoeven MC, Rentzsch F, Hammerschmidt M, Bakkers J. Zebrafish Bmp4 regulates left – right asymmetry at two distinct developmental time points. 2007;305: 577–588. doi:10.1016/j.ydbio.2007.03.001
77. Thurlings I, Rehmann H, Chocron S, Bakkers J, Smith KA, Noe E. Bmp and Nodal Independently Regulate lefty1 Expression to Maintain Unilateral Nodal Activity during Left-Right Axis Specification in Zebrafish. 2011;7. doi:10.1371/journal.pgen.1002289
78. Meno C, Saijoh Y, Fujii H, Ikeda M, Yokoyama T, Yokoyama M, et al. Left–right asymmetric expression of the TGFβ-family member lefty in mouse embryos [Internet]. Nature. 1996. pp. 151–155. doi:10.1038/381151a0
79. Cheng AMS, Thisse B, Thisse C, Wright CVE. The lefty-related factor Xatv acts as a feedback inhibitor of Nodal signaling in mesoderm induction and L-R axis development in Xenopus. 2000;1061: 1049–1061.
80. Lenhart KF, Lin S, Titus TA, Postlethwait JH, Burdine RD. Two additional midline barriers function with midline lefty1 expression to maintain asymmetric Nodal signaling during left-right axis specification in zebrafish INTRODUCTION. 2011;4410: 4405–4410. doi:10.1242/dev.071092
81. Burdine RD, Grimes DT. Antagonistic interactions in the zebrafish midline prior to the emergence of asymmetric gene expression are important for left–right patterning. Philos Trans R Soc B Biol Sci. 2016; doi:10.1098/rstb.2015.0402
82. Ocaña OH, Coskun H, Minguillón C, Murawala P, Tanaka EM, Galcerán J, et al. A right-handed signalling pathway drives heart looping in vertebrates. Nature. Nature Publishing Group; 2017;549: 86–90. doi:10.1038/nature23454
83. Ober EA, Field HA, Stainier DYR. From endoderm formation to liver and pancreas development in zebrafish. Mech Dev. 2003;120: 5–18. doi:10.1016/S0925-4773(02)00327-1
84. Warga RM, Nüsslein-Volhard C. Origin and development of the zebrafish endoderm. Development. 1999;126: 827–838.
85. Bally-Cuif L, Goutel C, Wassef M, Wurst W, Rosa F. Coregulation of anterior and posterior mesendodermal development by a hairy-related transcriptional repressor. Genes Dev. 2000;14:

1664–1677. doi:10.1101/gad.14.13.1664
86. Field HA, Si Dong PD, Beis D, Stainier DYR. Formation of the digestive system in zebrafish. II. Pancreas morphogenesis. Dev Biol. 2003;261: 197–208. doi:10.1016/S0012-1606(03)00308-7
87. Wallace KN, Pack M. Unique and conserved aspects of gut development in zebrafish. Dev Biol. 2003;255: 12–29. doi:10.1016/S0012-1606(02)00034-9
88. Stainier DYR. A glimpse into the molecular entrails of endoderm formation. Genes Dev. 2002;16: 893–907. doi:10.1101/gad.974902
89. Goessling W, Stainier DY. Endoderm specification and liver development [Internet]. Methods in Cell Biology. Elsevier Ltd; 2016. doi:10.1016/bs.mcb.2016.03.042
90. Dickmeis T, Mourrain P, Saint-Etienne L, Fischer N, Aanstad P, Clark M, et al. A crucial component of the endoderm formation pathway, casanova, is encoded by a novel sox-related gene. Genes Dev. 2001;15: 1487–1492. doi:10.1101/gad.196901
91. Bagnat M, Cheung ID, Mostov KE, Stainier DYR. Genetic control of single lumen formation in the zebrafish gut. Nat Cell Biol. 2007;9: 954–960. doi:10.1038/ncb1621
92. Horne-Badovinac S. A Cellular Framework for Gut-Looping Morphogenesis in Zebrafish. Science (80-). 2003;302: 662–665. doi:10.1126/science.1085397
93. Yin C, Kikuchi K, Hochgreb T, Poss KD, Stainier DYR. Hand2 regulates extracellular matrix remodeling essential for gut-looping morphogenesis in zebrafish. Dev Cell. Elsevier Inc.; 2010;18: 973–984. doi:10.1016/j.devcel.2010.05.009
94. Tiso N, Moro E, Argenton F. Zebrafish pancreas development. Mol Cell Endocrinol. 2009;312: 24–30. doi:10.1016/j.mce.2009.04.018
95. Ward AB, Warga RM, Prince VE. Origin of the zebrafish endocrine and exocrine pancreas. Dev Dyn. 2007;236: 1558–1569. doi:10.1002/dvdy.21168
96. Zecchin E, Mavropoulos A, Devos N, Filippi A, Tiso N, Meyer D, et al. Evolutionary conserved role of ptf1a in the specification of exocrine pancreatic fates. Dev Biol. 2004;268: 174–184. doi:10.1016/j.ydbio.2003.12.016
97. Wendik B, Maier E, Meyer D. Zebrafish mnx genes in endocrine and exocrine pancreas formation. Dev Biol. 2004;268: 372–383. doi:10.1016/j.ydbio.2003.12.026
98. Tehrani Z, Lin S. Endocrine pancreas development in zebrafish. Cell Cycle. 2011;10: 3466–3472. doi:10.4161/cc.10.20.17764
99. Tao T, Peng J. Liver development in zebrafish (Danio rerio). J Genet Genomics. Institute of Genetics and Developmental Biology and the Genetics Society of China; 2009;36: 325–334. doi:10.1016/S1673-8527(08)60121-6
100. de Campos-Baptista MIM, Holtzman NG, Yelon D, Schier AF. Nodal signaling promotes the speed and directional movement of cardiomyocytes in zebrafish. Dev Dyn. Wiley Online Library; 2008;237: 3624–3633.
101. Lenhart KF, Holtzman NG, Williams JR, Burdine RD. Integration of Nodal and BMP Signals in the Heart Requires FoxH1 to Create Left – Right Differences in Cell Migration Rates That Direct Cardiac Asymmetry. 2013;9. doi:10.1371/journal.pgen.1003109
102. Williams JR. Nodal directs asymmetric cardiac morphogenesis through regulation of the actin cytoskeleton. Princeton University; 2015.
103. Yokota C. A novel role for a nodal-related protein; Xnr3 regulates convergent extension movements via the FGF receptor. Development. 2003;130: 2199–2212. doi:10.1242/dev.00434
104. Pézeron G, Mourrain P, Courty S, Ghislain J, Becker TS, Rosa FM, et al. Live Analysis of Endodermal Layer Formation Identifies Random Walk as a Novel Gastrulation Movement. Curr Biol. 2008;18: 276–281. doi:10.1016/j.cub.2008.01.028
105. Woo S, Housley MP, Weiner OD, Stainier DYR. Nodal signaling regulates endodermal cell motility and actin dynamics via Rac1 and Prex1. J Cell Biol. 2012;198: 941–952. doi:10.1083/jcb.201203012
106. Viotti M, Niu L, Shi SH, Hadjantonakis AK. Role of the gut endoderm in relaying left-right patterning in mice. PLoS Biol. 2012;10. doi:10.1371/journal.pbio.1001276
107. Saund RS, Kanai-Azuma M, Kanai Y, Kim I, Lucero MT, Saijoh Y. Gut endoderm is involved in the transfer of left-right asymmetry from the node to the lateral plate mesoderm in the mouse embryo. Development. 2012;139: 2426–35. doi:10.1242/dev.079921

108. Kimmel CB, Ballard WW, Kimmel SR, Ullmann B, Schilling TF. Stages of embryonic development of the zebrafish. Dev Dyn. 1995;203: 253–310. doi:10.1002/aja.1002030302
109. Schindelin J, Arganda-Carreras I, Frise E, Kaynig V, Longair M, Pietzsch T, et al. Fiji: an open-source platform for biological-image analysis. Nat Methods. Nature Research; 2012;9: 676–682.
110. Ando R, Hama H, Yamamoto-Hino M, Mizuno H, Miyawaki A. An optical marker based on the UV-induced green-to-red photoconversion of a fluorescent protein. Proc Natl Acad Sci. 2002;99: 12651–12656. doi:10.1073/pnas.202320599
111. Bordalo DM. Fate map of zebrafish left-right organizer. 2015.
112. Tomura M, Yoshida N, Tanaka J, Karasawa S, Miwa Y, Miyawaki A, et al. Monitoring cellular movement in vivo with photoconvertible fluorescence protein "Kaede" transgenic mice. Proc Natl Acad Sci. 2008;105: 10871–10876. doi:10.1073/pnas.0802278105
113. Tsutsui H, Karasawa S, Shimizu H, Nukina N, Miyawaki A. Semi-rational engineering of a coral fluorescent protein into an efficient highlighter. EMBO Rep. 2005;6: 233–238. doi:10.1038/sj.embor.7400361
114. Lombardo VA, Sporbert A, Abdelilah-Seyfried S. Cell Tracking Using Photoconvertible Proteins During Zebrafish Development. J Vis Exp. 2012; 4–9. doi:10.3791/4350
115. Wallace KN, Yusuff S, Sonntag JM, Chin AJ, Pack M. Zebrafish hhex regulates liver development and digestive organ chirality. Genesis. 2001;30: 141–143. doi:10.1002/gene.1050
116. Burke Z, Oliver G. Prox1 is an early specific marker for the developing liver and pancreas in the mammalian foregut endoderm. Mech Dev. 2002;118: 147–155. doi:10.1016/S0925-4773(02)00240-X
117. Ober EA, Verkade H, Field HA, Stainier DYR. Mesodermal Wnt2b signalling positively regulates liver specification. Nature. 2006;442: 688–691. doi:10.1038/nature04888
118. Shin D, Shin CH, Tucker J, Ober EA, Rentzsch F, Poss KD, et al. Bmp and Fgf signaling are essential for liver specification in zebrafish. Development. 2007;134: 2041–2050. doi:10.1242/dev.000281
119. Korzh S, Emelyanov A, Korzh V. Developmental analysis of ceruloplasmin gene and liver formation in zebrafish. Mech Dev. 2001;103: 137–139. doi:10.1016/S0925-4773(01)00330-6
120. Shen MM. Nodal signaling: developmental roles and regulation. Development. 2007;134: 1023–1034. doi:10.1242/dev.000166

6. Appendices

6.1 – Supplementary Figures

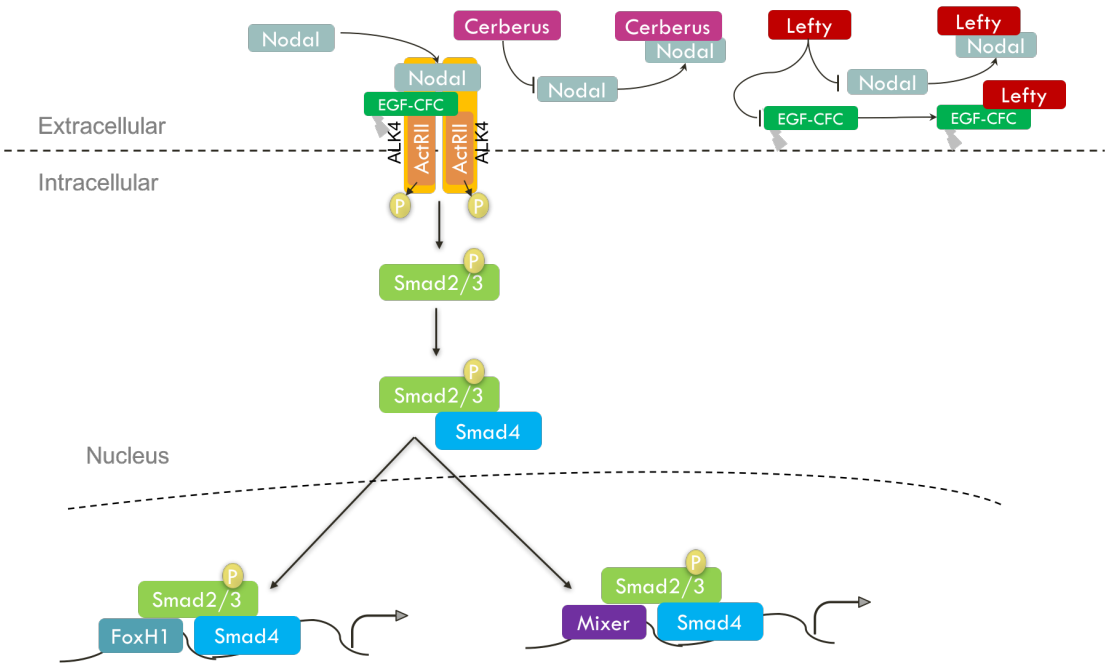

Figure 6.1 – Schematic outline of the simplified Nodal signalling pathway. Nodal pathway ligands belong to the TGFβ superfamily and include mouse Nodal; Cyclops, Squint and Southpaw in zebrafish; Xnr1, 2, 4, 5 and 6 in Xenopus. EGF-CFC proteins, small cysteine-rich extracellular proteins attached to the plasma membrane through a glycosyl-phosphatidylinositol (GPI) linkage, such as zebrafish one-eyed pinhead (*oep*); mouse Cripto and human Cryptic are required for Nodal signalling, acting as coreceptors for Nodals. Nodal ligands bind to type I, and type II serine-threonine kinase receptors. Activation of the receptor leads to the phosphorylation of the type I receptor by the type II kinase also the phosphorylation of Smad2/3. Then, the activated Smad2/3 associates with Smad4 and is translocated to the nucleus. Inside the nucleus, the activated Smad2/3-Smad4 complexes interact with the transcription factor FoxH1 or Mixer on target promoters. The function of the Nodal pathway is highly affected by the activities of the transcription factors such FoxH1 and the Mixer subclass of homeodomain proteins that contain Smad-interaction motifs required for interacting with Smad2/3. Cerberus and Lefty proteins are antagonists that can interact with Nodal ligands; also, Lefty proteins can interact with EGF-CFC coreceptors inhibiting their function. Adapted from **[63,120]**.

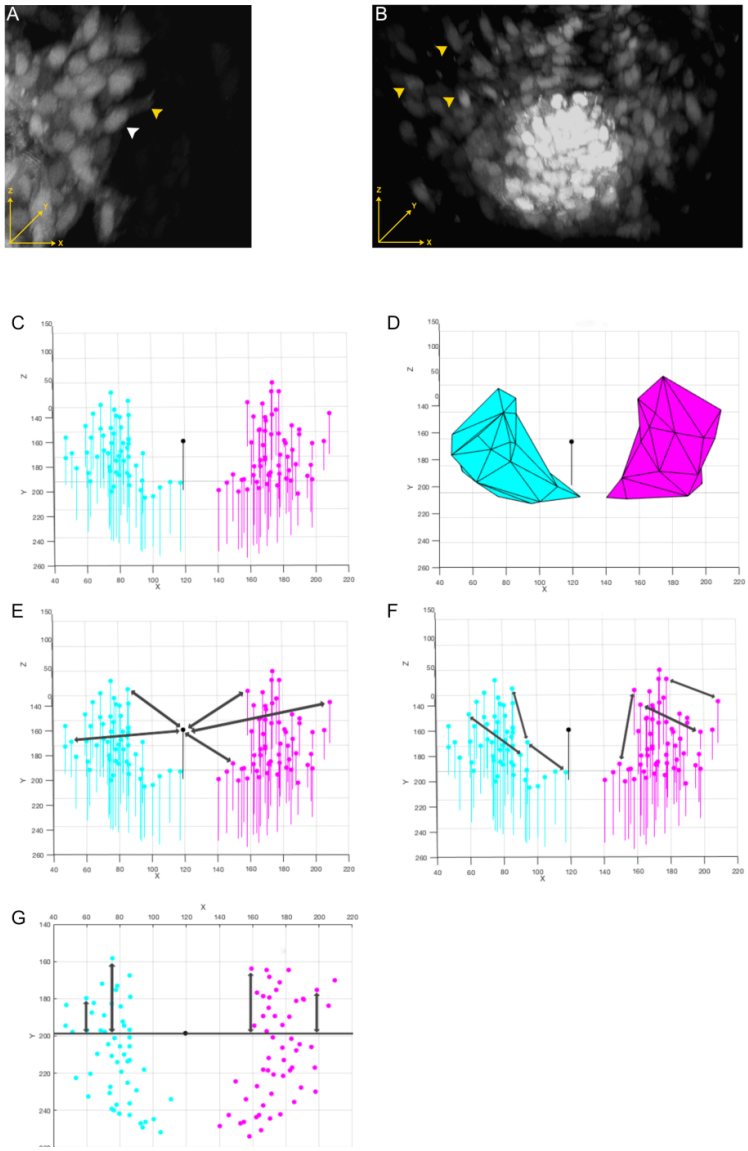

Figure 6.2 – Fixed embryos analysis. (A-B) Illustrative images of migration criteria. **(A)** white arrowhead: nucleus position; yellow arrowhead: cell protrusions. **(B)** yellow arrowheads: examples of migratory cells position in x, y and z. (**C-G**) Graphic representation of cell distribution. Cyan dots and polygon: left cells; Magenta dots and polygon: right cells; Black dot: KV centroid. **(C)** 3D distribution of left and right cells in a 13ss embryo and the centroid of the KV. **(D)** Shape described by the 3D points of cell distribution. The volume was calculated for this structure. **(E)** Schematic representation of Distance of cells to KV in 3D calculation. **(F)** Schematic representation of Distance Between Cells in 3D calculation. **(G)** Schematic representation of Distance of cells to KV in y axis calculation.

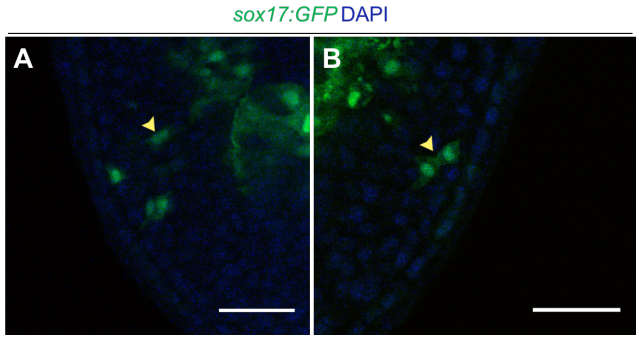

Figure 6.3 – Cell proliferation analysis. (A-B) Illustrative images of cells undergoing mitosis, used for the cell proliferation study. yellow arrowhead: dividing cells. Scale bar = 50 μm

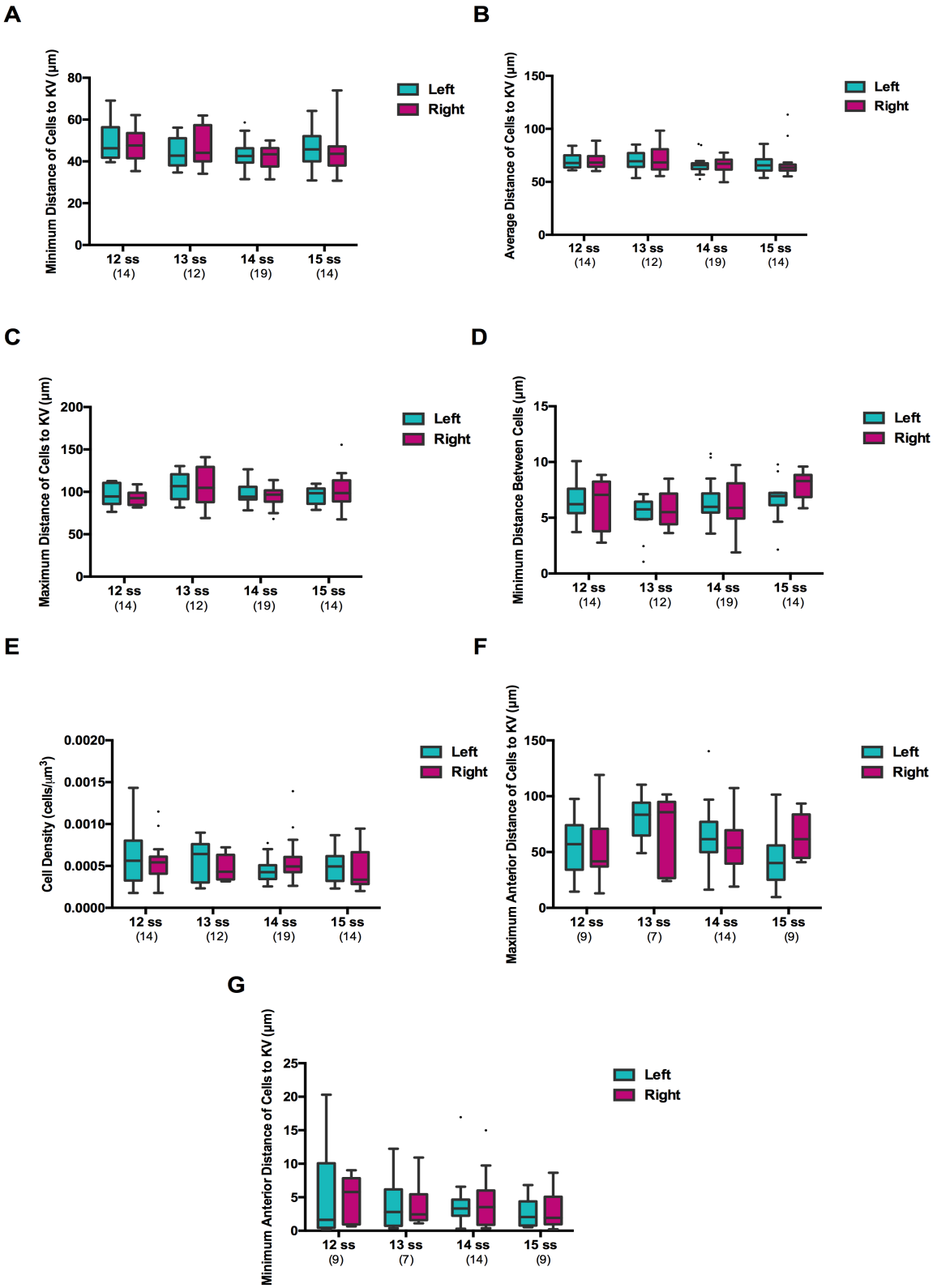

Figure 6.4 –Time course studies using fixed embryos: calculated parameters for which no LR differences were found in migrating cells. **(A-G)** The LR Migration parameters calculated for fixed embryos which did not present significant differences. Those parameters include: Minimum **(A)**, average **(B)** and maximum **(C)** overall distance of cells to KV. **(D)** Minimum distance between cells **(E)** Cell density. Maximum **(F)** and minimum **(G)** anterior distance of cells to KV. The number of embryos analysed (N) is shown between parentheses for each somite stage.

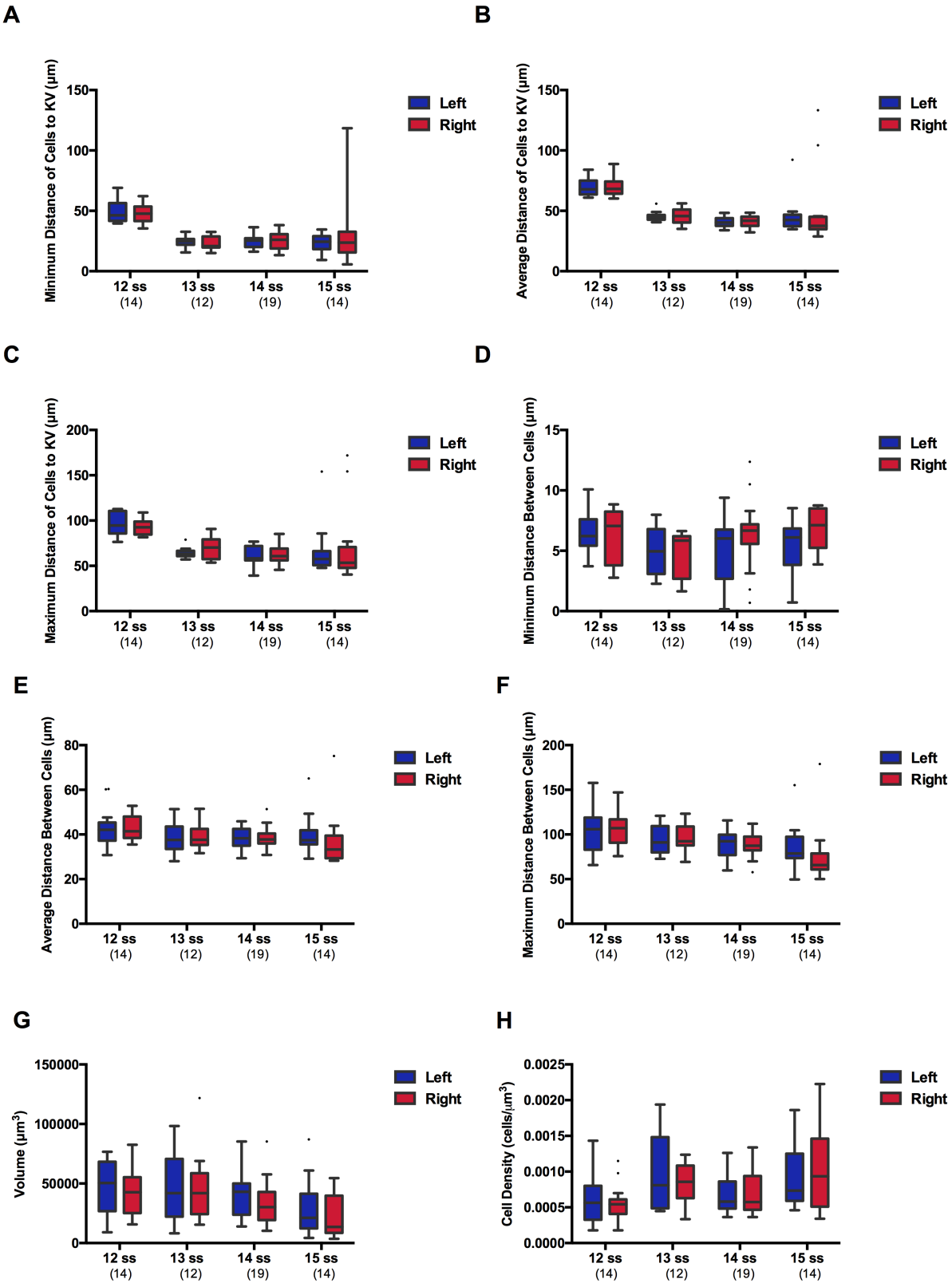

Figure 6.5 –Time course studies using fixed embryos: calculated parameters for which no LR differences were found in non-migrating cells. **(A-F)** The LR parameters calculated for fixed embryos which did not present significant differences. Those parameters include: Minimum **(A)**, average **(B)** and maximum **(C)** overall distance of cells to KV. Minimum **(D)**, average **(E)** and maximum **(F)** overall distance between cells. **(G)** Volume and **(C)** Cell density. The number of embryos analysed (N) is shown between parentheses for each somite stage.

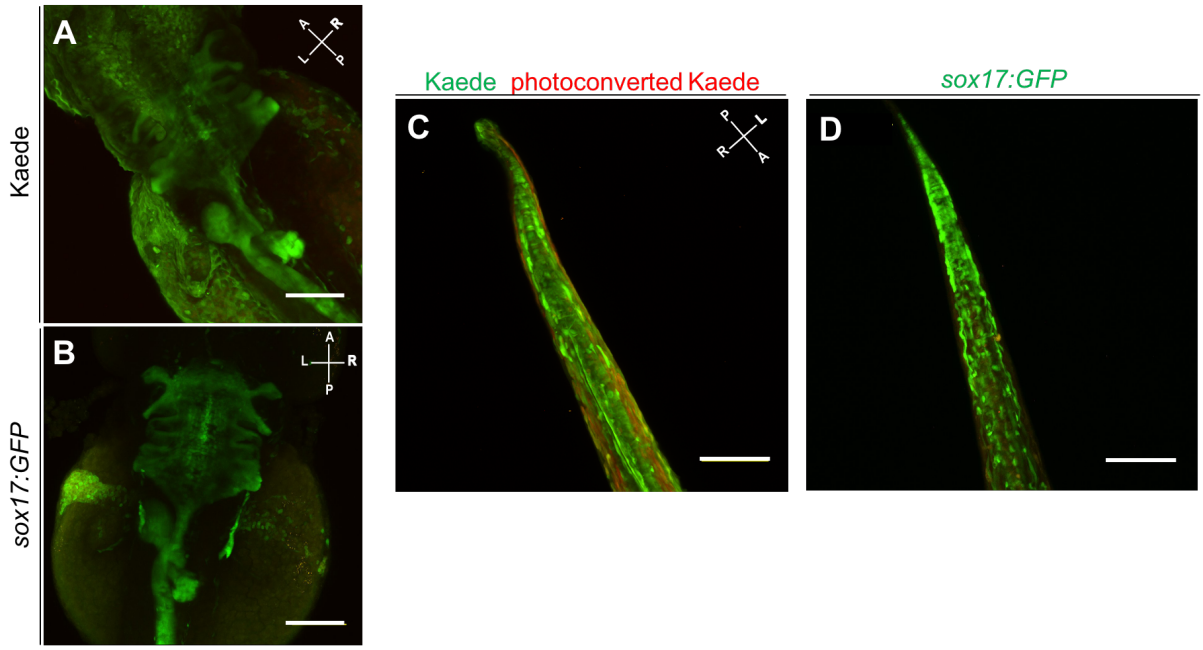

Figure 6.6 – Following *sox17:GFP*$^{+}$ cell fate using *Kaede* photoconversion at 48 hpf. Assessment for photoconverted cells presence and position at 48 hpf **(A-B)**. **(A)** Two-photon Z projection of a dorsal view of the pancreatic and liver buds in photoconverted *Tg*(*sox17:GFP*) **(A)** and a not injected *Tg*(*sox17:GFP*) **(B)** larvae. No yellow or red cells were found 48 hpf in this region**.** (**C-D**) Two-photon Z projections of the tails in 48 hpf photoconverted *Tg*(*sox17:GFP*) **(C)** and a not injected *Tg*(*sox17:GFP*) **(D)** larvae, where red but no yellow cells are present **(C)**. Scale bar = 100 µm. Axes are indicated: A, anterior; P, posterior; L, left; R, right.

6.2 – Detailed Procedures

6.2.1 - TUNEL Assay Protocol

This method detects DNA fragmentation by labelling the 3'- hydroxyl termini of the double-strand DNA breaks generated during apoptosis with fluorescein-dUTP.
Embryos were previously fixed with PFA 4% and washed for a few days in a PBS 1x solution in the dark at 4ºC. Embryos were then submitted to two additional washes of 5min each in PBS Triton 0.1% (50 mL PBS, 50 µL Triton X-100 10%) and manually dechorionated in the same solution. Afterwards, the samples were rinsed in MilliQ deionized water and incubated in acetone for 7 min at -20 ºC. After a wash in PBS 1X, digestion with Proteinase K (1:1000) diluted in PBS Triton 0.1% was performed for 1 and 3min, for 13ss and 14ss respectively. Embryos were then post-fixed in PFA 4% during 20 min at RT. The embryos were washed during 5 min in PBS 1x and TUNEL reaction solution (1:10 dilution of the enzyme in Label Solution) was added and incubated ON at 4ºC. Control samples were supplied only with Label Solution. In the second day, the embryos were submitted to three washes of 5min with PBS 1x and incubated ON at 4ºC in a solution of 4',6-diamidino-2-phenylindole (DAPI) diluted 1:1 in PBS 1X. The third day consisted of 3 washes in PBS 1X during 5min followed by the mounting of the embryos for image acquisition.

6.2.2 - Immunostaining: PCNA Protocol

To detect the presence of Proliferating Cell Nuclear Antigen (PCNA), an immunostaining protocol was performed with the antibody anti-PCNA.
Previously fixed embryos with 13 and 14ss were kept for a few days in a PBS 1x solution in the dark and were first manually dechorionated in a PBSX 1% (50 mL PBS, 500 µL Triton X-100 10%) solution. Afterwards, digestion with Proteinase K (1:1000) diluted in PBSX1% was performed for 1 and 3min, for 13ss and 14ss respectively, and then fixed in PFA 4% during 20 min at RT. The embryos were submitted to five washes of 5min each in PBSX 1% and then rinsed in MilliQ deionized water. The anti-PCNA antibody staining required that the embryos be subjected to an antigen retrieval step, which consisted in an incubation for 1min at 95ºC in Sodium Citrate Buffer (10mM citric acid with 0,05% Tween20, pH6). After this step, the embryos were rinsed in PBSX 1% and then blocked in a solution of PBDX (5 mL PBS 10X, 0,5 g BSA, 500 µL DMSO, 500 µL Triton X-100 10%, 44 mL MilliQ deionized water) plus fetal bovine serum (FBS - 15 µL of serum per mL of PBDX to use). Lastly, the embryos were incubated ON at 4ºC with rabbit (polyclonal anti-PCNA (1:400) (Santa Cruz Biotechnology?) primary antibody diluted in PBDX. In the second day, the embryos were submitted to 6 washes of 30min each in PBDX at RT and then incubated ON at 4ºC with Alexa Fluor 546-conjugated goat anti-rabbit (1:500) (Invitrogen) secondary antibody diluted in PBDX and in DAPI solution (1:1). On the third day, two washes in PBDX for 10min each followed by one wash for 30min in PBSX 1% were initially performed. Next, the embryos were fixed in PFA 4% for 5min and then washed three times for 5min each in PBSX 1%. When finished these last steps, the embryos were stored in PBSX 1% ON at 4ºC and mounted for image acquisition in the next day.

6.2.3 – Image Analysis: live embryos

Z-stacks of two-photon images were first processed using Fiji software to view as Hyperstack (default order: xyczt) and the Z-stack repositioned by applying rotational transformations to ensure that the embryo was aligned with the AP-axis vertical and dorsal side facing the viewer. Since the z-stacks were acquired with 1024 × 512 pixel image format (odd lines skipped) the stack was re-scaled to obtain isometric stacks, *i.e.,* with same resolution in X and Y; this was done by applying a bin "add" transformation with a shrink factor set to 2 for the x axis (this also increased the signal-to-noise of the images, which helped during automatic detection of cells).
Minor lateral (xy) drift movements of the embryo were corrected by first applying the ImageStabilizer ImageJ plug-in; since this plugin only works on 2D movies, we first produced a Maximum Intensity Projection from which the ImageStabilizer plugin produced a "transformation matrix"; this was then used by an ImageJ macro to apply to the original hyperstack, thereby correcting the XY drift. The Bioformarts ImageJ plug-in was used to export the Hyperstack, by writing each time point ("cycle") to a separate multi-page file in ome.tif format to make it compatible with the Imaris v6.4 (Bitplane) software.
In some cases, this semi-automatic procedure could not correct major displacements, so we opted for a manual drift correction using the Amira V5.3 software (FEI). Each time-point Z-stack was positioned in 3D by using the KV and tail as fiduciary markers; this procedure resulted in the KV remaining stationary in the "undrifted" version of the stack, which does not reflect the natural morphogenetic movements of the embryos, but is necessary to allow interpretation of movements of individual cells. All measurements presented in this work were in relation to a stationary KV and vertical embryonic mid-axis.
Using Imaris v6.4 (Bitplane) software, the z-stacks were reconstructed in 3D and reiterated through time to produce a 3D movie of *sox17:*GFP^{+} cells migration. The embryos corrected for drift with

ImageStabilizer were first corrected to annul the movement of the KV (*i.e.,* make it stationary) by selecting KV cells *sox17:*GFP$^+$ using the Spots module and then applying Imaris drift correction. The cell tracking was performed again in the drift-corrected stacks using the Spots module again, this time creating two different ROIs: one for the Left and another for the Right side. Only cells seen migrating from the compact group of *sox17:*GFP$^+$ cells localized in a posterior position to KV were selected, while cells already migrating and for which we could not trace the starting point were excluded from this analysis. After selecting each ROI, a spot detection algorithm was applied with an average cell diameter set to 8μm according to several measurements previously performed. This automatic algorithm failed to select the desired cells over time points even when manually tuning the threshold for spot detection, consequently the spot detection was essentially performed by manual selection of each cell over time. Subsequently, when all Left and Right-side cells were selected the cell tracking analysis was applied, choosing an Autoregressive Motion with a Maximum Distance of a spot between consecutive time points set to 20μm and a Gap Size of one time point for which the cell could be absent. The produced tracks were displayed as dragon tail (over time) and as displacement vectors. This 4D cell tracking analysis identified the x, y, and z coordinates for each cell at each given time point. These values and statistics for average values, *i.e.*, the average values of the calculated measurements for all spots, were exported as a .csv file, which was then imported to an Excel spreadsheet We extracted the minimum, maximum and average values of the overall track length, i.e., the measurements of total distance covered by the cells; track displacement; track speed; and track straightness index, a measure of directional persistence (displacement/track length).

6.2.4 - Image Analysis: fixed embryos

Z-stacks of two-photon images were first processed using Fiji software to correct embryo position applying a rotational transformation as explained in previous section. Then, using the Imaris v6.4 (Bitplane) software, z-stacks were reconstructed into 3D images. For every embryo, the x, y, and z coordinates for the centre point of the lumen of the KV were acquired using the "Section view" mode by aligning the centre in the three planes. (XY, YZ, XZ). Using the "Surprass view" mode, the KV cells were digitally "erased" by contouring the KV in every z slice and then reconstructing it as a surface. This "KV surface volume" was then used as a mask to subtract from the original Z-stack the contents of the KV, and to create a new channel with only the contents of the KV - the KV was then displayed with a different colour, which facilitated the identification of KV boundaries for 3D rendering and spotting of cells. To count the cells, we used the "Spots module" and defined four ROIs: (a) Left Migrating; (b) Left Non-Migrating; (c) Right Migrating and (d) Right Non-Migrating. Although this part of the study used fixed embryos (*i.e.*, we had no information about migratory behaviour of the cells), we classified cells from the aggregate in the vicinity of the KV as having a "migratory behaviour" if they showed a clearly polarised morphology with the nucleus closer to the KV, and with large protrusions facing away from the KV (we had learned that this is the typical morphology of migratory cells from observing the movies of live-imaging embryos) (Fig. 6.2: (A-B)). The cells in the aggregate that lacked this "migratory morphology" were classified as "Non-Migrating". For each selected ROI, the spot detection algorithm was applied with an average cell diameter set to 8 μm, as chosen in live imaging analysis. As previously described for the time-lapse analysis, the automatic algorithm even after manually tuning the threshold for spot detection was never completely efficient to select the desired cells therefore a major part of the process was performed manually according the criteria previously mentioned.

This procedure allowed the identification of x, y, and z coordinates for each cell and these values were exported as a .csv file that was then imported to an Excel spreadsheet. A script was written using MATLAB 2016a (See Appendix) to calculate L-R Migration parameters and represent the distribution of the cells from the exported coordinates. The number of cells (NC) was given by the number of cells

for which the position was noted and the volume (V) (μm^3) relative to the 3D distribution of the cells was calculated from the shape described by the cells 3D coordinates (*i.e.,* the volume of the "cloud" of 3D coordinates). The Cell density (CD) (cells. μm^{-3}) was then calculated as the number of cells per volume. Regarding the coordinates obtained for the centroid of the KV, Average, Maximum and Minimum Distance of Cells to KV centroid (in µm) were calculated for all cells; the same parameters were calculated just for the y coordinate, Average, Maximum and Minimum Anterior Distance of Cells in to KV (µm) respectively, as a measure of the displacement along the embryos AP-axis. The average, Average, Maximum and Minimum Distance Between Cells (µm) was also calculated.

6.2.4.1 – MATLAB script for LR migratory parameters

```
close all
clc
clear all

%Count number of existing files in directory
folder = uigetdir;
allfiles = dir(folder);
txtfiles = dir(fullfile(folder, '*.txt'));
% dirname = uigetdir;
% cont_dir = dir([dirname,'./*.txt']);
no_emb = length(txtfiles);
fprintf('\nDetected %u files!\n\n',no_emb);

for n=1:no_emb
    a=txtfiles(n).name;
    str_emb{n}=a;

    C = readtable(str_emb{n},'Format','%f %f %f %
```

```
MRmean=mean(MRdistKV);
MRsigma=std(MRdistKV);


%Calculate the Distance Between Cells - Right
% calculateCellsRightDistance(szMR(1),mrx )
for w=1:(szMR(1)-1)
    for i=1:szMR(1)
        calculateDistance(MRX(w), MRX(i))
        MRdist(w,i) = sqrt((MRX(w)-MRX(i)).^2 + (MRY(w)-MRY(i)).^2 + (MRZ(w)-MRZ(i)).^2);

    end
end
MRdist=triu(MRdist);

%To Calculate the Average, Maximum and Minimum Values of the Distance
%between cells - Right
vectMRdist=MRdist(find(MRdist));
MRmeanRdist=mean(vectMRdist);
MRdistmax=max(vectMRdist);
MRdistmin=min(vectMRdist);
MRdistsigma=std(vectMRdist);


%Calculate the Distance Between Cells - Left
for w=1:(szML(1)-1)
    for i=1:szML(1)
        MLdist(w,i) = sqrt((MLX(w)-MLX(i)).^2 + (MLY(w)-MLY(i)).^2 + (MLZ(w)-MLZ(i)).^2);

    end
end
MLdist=triu(MLdist);

%To Calculate the Average, Maximum and Minimum Values of the Distance
%between cells - Left
vectMLdist=MLdist(find(MLdist));
MLmeanLdist=mean(vectMLdist);
MLdistmax=max(vectMLdist);
MLdistmin=min(vectMLdist);
MLdistsigma=std(vectMLdist);

%To Calculate the Average, Maximum and Minimum Values of the Distance
%between cells - Left
Mdistmean=[MLmeanLdist,MRmeanRdist];
Mdistsigma=[MLdistsigma,MRdistsigma];
Mdistmax=[MLdistmax,MRdistmax];
Mdistmin=[MLdistmin,MRdistmin];

%To plot the Average, Maximum and Minimum Values of the Distance
%between cells comparing Left and Right
MLmean=mean(MLdistKV);
MLsigma=std(MLdistKV);
Mmean=[MLmean,MRmean];
Msigma=[MLsigma,MRsigma];

MdistmaxKV=[MLdistKVmax,MRdistKVmax];
MdistminKV=[MLdistKVmin,MRdistKVmin];

% % Plot the cells as points (dots) in 3D
figure
stem3(KV(1),KV(2),KV(3),'k','filled')
hold on
stem3(MRX,MRY,MRZ,'m', 'filled')
hold on
stem3(MLX,MLY,MLZ, 'c', 'filled')
axis on
rotate3d on;
hold off
xlabel('X')
ylabel('Y')
zlabel('Z')
title('Migrating')

%To calculate the volume of a shape described by 3D points (by the cells in this case)

MP=[MRX,MRY,MRZ];
MQ=[MLX,MLY,MLZ];
[k1,MVR] = boundary(MP);
[k2,MVL] = boundary(MQ);
Mvolume=[MVL,MVR];
MLdensity=MLcellNum/MVL;
MRdensity=MRcellNum/MVR;
McellDensity=[MLdensity,MRdensity];
```

```
    % %The Graph of the Volume previously calculated
    figure
    trisurf(k1,MP(:,1),MP(:,2),MP(:,3),'Facecolor','magenta','FaceAlpha',1)
    hold on
    stem3(KV(1),KV(2),KV(3),'k','filled')
    hold on
    trisurf(k2,MQ(:,1),MQ(:,2),MQ(:,3),'Facecolor','cyan','FaceAlpha',1)

    axis on
    rotate3d on;
    xlabel('X')
    ylabel('Y')
    zlabel('Z')
    title('Migrating')
    hold off


    M{n,1}=[McellNum,Mmean,Msigma,MdistmaxKV,MdistminKV,Mdistmean,Mdistsigma,Mdistmax,Mdistmin,Mvolu
me,McellDensity];



    % % ---------------Non Migrating-------------

    % Define the values for Coordinates X, Y, Z for every cell

    NMLX=A(1:end,7);
    NMLY=A(1:end,8);
    NMLZ=A(1:end,9);
    NMRX=A(1:end,10);
    NMRY=A(1:end,11);
    NMRZ=A(1:end,12);

    %deletes zeros in the vectors
    NMRX=NMRX(find(NMRX),:);
    NMRY=NMRY(find(NMRY),:);
    NMRZ=NMRZ(find(NMRZ),:);
    NMLX=NMLX(find(NMLX),:);
    NMLY=NMLY(find(NMLY),:);
    NMLZ=NMLZ(find(NMLZ),:);

    % To Count and plot the number of cells on each side
    szNMR=size(NMRX);
    szNML=size(NMLX);
    NMRcellNum=(szNMR(1));
    NMLcellNum=(szNML(1));
    NMcellNum=[NMLcellNum,NMRcellNum];

    % To plot the Average, Maximum and Minimum Values of the Distance of Cells to KV comparing Left
and Right

    NMRdistKV = sqrt((KV(1)-NMRX).^2 + (KV(2)-NMRY).^2 + (KV(3)-NMRZ).^2);
    NMRdistKVmax=max(NMRdistKV);
    NMRdistKVmin=min(NMRdistKV);
    NMLdistKV = sqrt((KV(1)-NMLX).^2 + (KV(2)-NMLY).^2 + (KV(3)-NMLZ).^2);
    NMLdistKVmax=max(NMLdistKV);
    NMLdistKVmin=min(NMLdistKV);
    NMRmean=mean(NMRdistKV);
    NMRsigma=std(NMRdistKV);


    %Calculate the Distance Between Cells - Right
    for w=1:(szNMR(1)-1)
        for i=1:szNMR(1)
            NMRdist(w,i) = sqrt((NMRX(w)-NMRX(i)).^2 + (NMRY(w)-NMRY(i)).^2 + (NMRZ(w)-NMRZ(i)).^2);

        end
    end
    NMRdist=triu(NMRdist);

    %To Calculate the Average, Maximum and Minimum Values of the Distance
    %between cells - Right
    vectNMRdist=NMRdist(find(NMRdist));
    NMRmeanRdist=mean(vectNMRdist);
    NMRdistmax=max(vectNMRdist);
    NMRdistmin=min(vectNMRdist);
    NMRdistsigma=std(vectNMRdist);


    %Calculate the Distance Between Cells - Left
    for w=1:(szNML(1)-1)
        for i=1:szNML(1)
            NMLdist(w,i) = sqrt((NMLX(w)-NMLX(i)).^2 + (NMLY(w)-NMLY(i)).^2 + (NMLZ(w)-NMLZ(i)).^2);
```

```
        end
    end
    NMLdist=triu(NMLdist);

    %To Calculate the Average, Maximum and Minimum Values of the Distance
    %between cells - Left
    vectNMLdist=NMLdist(find(NMLdist));
    NMLmeanLdist=mean(vectNMLdist);
    NMLdistmax=max(vectNMLdist);
    NMLdistmin=min(vectNMLdist);
    NMLdistsigma=std(vectNMLdist);

    %To Calculate the Average, Maximum and Minimum Values of the Distance
    %between cells - Left
    NMdistmean=[NMLmeanLdist,NMRmeanRdist];
    NMdistsigma=[NMLdistsigma,NMRdistsigma];
    NMdistmax=[NMLdistmax,NMRdistmax];
    NMdistmin=[NMLdistmin,NMRdistmin];

    %To plot the Average, Maximum and Minimum Values of the Distance
    %between cells comparing Left and Right
    NMLmean=mean(NMLdistKV);
    NMLsigma=std(NMLdistKV);
    NMmean=[NMLmean,NMRmean];
    NMsigma=[NMLsigma,NMRsigma];

    NMdistmaxKV=[NMLdistKVmax,NMRdistKVmax];
    NMdistminKV=[NMLdistKVmin,NMRdistKVmin];

    % % Plot the cells as points (dots) in 3D
    figure
    stem3(KV(1),KV(2),KV(3),'k','filled')
    hold on
    stem3(NMRX,NMRY,NMRZ,'m', 'filled')
    hold on
    stem3(NMLX,NMLY,NMLZ, 'c', 'filled')
    axis on
    rotate3d on;
    hold off
    xlabel('X')
    ylabel('Y')
    zlabel('Z')
    title('Non Migrating')

    %To calculate the volume of a shape described by 3D points (by the cells in this case)

    NMP=[NMRX,NMRY,NMRZ];
    NMQ=[NMLX,NMLY,NMLZ];
    [k1,NMVR] = boundary(NMP);
    [k2,NMVL] = boundary(NMQ);
    NMvolume=[NMVL,NMVR];
    NMLdensity=NMLcellNum/NMVL;
    NMRdensity=NMRcellNum/NMVR;
    NMcellDensity=[NMLdensity,NMRdensity];

    %The Graph of the Volume previously calculated
    figure
    trisurf(k1,NMP(:,1),NMP(:,2),NMP(:,3),'Facecolor','magenta','FaceAlpha',1)
    hold on
    stem3(KV(1),KV(2),KV(3),'k','filled')
    hold on
    trisurf(k2,NMQ(:,1),NMQ(:,2),NMQ(:,3),'Facecolor','cyan','FaceAlpha',1)

    axis on
    rotate3d on;
    xlabel('X')
    ylabel('Y')
    zlabel('Z')
    title('Non Migrating')
    hold off

    NM{n,1}=[NMcellNum,NMmean,NMsigma,NMdistmaxKV,NMdistminKV,NMdistmean,NMdistsigma,NMdistmax,NMdis
tmin,NMvolume,NMcellDensity];


    % ---------------ALL Cells-------------

    % Define the values for Coordinates X, Y, Z for every cell

    ALX=A(1:end,13);
    ALY=A(1:end,14);
    ALZ=A(1:end,15);
    ARX=A(1:end,16);
    ARY=A(1:end,17);
```

```
    ARZ=A(1:end,18);

    %deletes zeros in the vectors
    ARX=ARX(find(ARX),:);
    ARY=ARY(find(ARY),:);
    ARZ=ARZ(find(ARZ),:);
    ALX=ALX(find(ALX),:);
    ALY=ALY(find(ALY),:);
    ALZ=ALZ(find(ALZ),:);

    % To Count and plot the number of cells on each side
    szAR=size(ARX);
    szAL=size(ALX);
    ARcellNum=(szAR(1));
    ALcellNum=(szAL(1));
    AcellNum=[ALcellNum,ARcellNum];

    % To plot the Average, Maximum and Minimum Values of the Distance of Cells to KV comparing Left
and Right

    ARdistKV = sqrt((KV(1)-ARX).^2 + (KV(2)-ARY).^2 + (KV(3)-ARZ).^2);
    ARdistKVmax=max(ARdistKV);
    ARdistKVmin=min(ARdistKV);
    ALdistKV = sqrt((KV(1)-ALX).^2 + (KV(2)-ALY).^2 + (KV(3)-ALZ).^2);
    ALdistKVmax=max(ALdistKV);
    ALdistKVmin=min(ALdistKV);
    ARmean=mean(ARdistKV);
    ARsigma=std(ARdistKV);


    %Calculate the Distance Between Cells - Right
    for w=1:(szAR(1)-1)
        for i=1:szAR(1)
            ARdist(w,i) = sqrt((ARX(w)-ARX(i)).^2 + (ARY(w)-ARY(i)).^2 + (ARZ(w)-ARZ(i)).^2);

        end
    end
    ARdist=triu(ARdist);

    %To Calculate the Average, Maximum and Minimum Values of the Distance
    %between cells - Right
    vectARdist=ARdist(find(ARdist));
    ARmeanRdist=mean(vectARdist);
    ARdistmax=max(vectARdist);
    ARdistmin=min(vectARdist);
    ARdistsigma=std(vectARdist);


    %Calculate the Distance Between Cells - Left
    for w=1:(szAL(1)-1)
        for i=1:szAL(1)
            ALdist(w,i) = sqrt((ALX(w)-ALX(i)).^2 + (ALY(w)-ALY(i)).^2 + (ALZ(w)-ALZ(i)).^2);

        end
    end
    ALdist=triu(ALdist);

    %To Calculate the Average, Maximum and Minimum Values of the Distance
    %between cells - Left
    vectALdist=ALdist(find(ALdist));
    ALmeanLdist=mean(vectALdist);
    ALdistmax=max(vectALdist);
    ALdistmin=min(vectALdist);
    ALdistsigma=std(vectALdist);

    %To Calculate the Average, Maximum and Minimum Values of the Distance
    %between cells - Left
    Adistmean=[ALmeanLdist,ARmeanRdist];
    Adistsigma=[ALdistsigma,ARdistsigma];
    Adistmax=[ALdistmax,ARdistmax];
    Adistmin=[ALdistmin,ARdistmin];

    %To plot the Average, Maximum and Minimum Values of the Distance
    %between cells comparing Left and Right
    ALmean=mean(ALdistKV);
    ALsigma=std(ALdistKV);
    Amean=[ALmean,ARmean];
    Asigma=[ALsigma,ARsigma];

    AdistmaxKV=[ALdistKVmax,ARdistKVmax];
    AdistminKV=[ALdistKVmin,ARdistKVmin];

    % Plot the cells as points (dots) in 3D
    figure
```

```
    stem3(KV(1),KV(2),KV(3),'k','filled')
    hold on
    stem3(ARX,ARY,ARZ,'m', 'filled')
    hold on
    stem3(ALX,ALY,ALZ, 'c', 'filled')
    axis on
    rotate3d on;
    hold off
    xlabel('X')
    ylabel('Y')
    zlabel('Z')
    title('All Cells')

    %To calculate the volume of a shape described by 3D points (by the cells in this case)

    AP=[ARX,ARY,ARZ];
    AQ=[ALX,ALY,ALZ];
    [k1,AVR] = boundary(AP);
    [k2,AVL] = boundary(AQ);
    Avolume=[AVL,AVR];
    ALdensity=ALcellNum/AVL;
    ARdensity=ARcellNum/AVR;
    AcellDensity=[ALdensity,ARdensity];

     %The Graph of the Volume previously calculated
    figure
    trisurf(k1,AP(:,1),AP(:,2),AP(:,3),'Facecolor','magenta','FaceAlpha',1)
    hold on
    stem3(KV(1),KV(2),KV(3),'k','filled')
    hold on
    trisurf(k2,AQ(:,1),AQ(:,2),AQ(:,3),'Facecolor','cyan','FaceAlpha',1)

    axis on
    rotate3d on;
    xlabel('X')
    ylabel('Y')
    zlabel('Z')
    title('All Cells')
    hold off

    All{n,1}=[AcellNum,Amean,Asigma,AdistmaxKV,AdistminKV,Adistmean,Adistsigma,Adistmax,Adistmin,Avo
lume,AcellDensity];

end


Mtable=cell2mat(M);
TM=array2table(Mtable);
NMtable=cell2mat(NM);
TNM=array2table(NMtable);
Alltable=cell2mat(All);
Tall=array2table(Alltable);

column={'NumberCellsL' 'NumberCellsR' 'AvrDistKVL' 'AvrDistKVR' 'stdDistKVL' 'stdDistKVR'
'maxDistKVL' 'maxDistKVR' 'minDistKVL' 'minDistKVR' 'AvrDistBetweCellL' 'AvrDistBetweCellR'
'stdDistBetweCellL' 'stdDistBetweCellR' 'maxDistBetweCellL' 'maxDistBetweCellR' 'minDistBetweCellL'
'minDistBetweCellR' 'volumeL' 'volumeR' 'CellDensityL' 'CellDensityR'};
% column={'NumberCells' 'Avr.dist.KV(um)' 'std.dist.KV(um)' 'maxDistKV(um)' 'minDistKV(um)'
'Avr.distBetweCell(um)' 'std.distBetweCell(um)' 'maxDistBetweCell(um)' 'minDistBetweCell(um)'
'volume(um^3)' 'CellDensity(cell/(um^3))''NumberCells' 'Avr.dist.KV(um)' 'std.dist.KV(um)'
'maxDistKV(um)' 'minDistKV(um)' 'Avr.distBetweCell(um)' 'std.distBetweCell(um)'
'maxDistBetweCell(um)' 'minDistBetweCell(um)' 'volume(um^3)' 'CellDensity(cell/(um^3))'};


TM.Properties.RowNames =str_emb;
TM.Properties.VariableNames = column;
TNM.Properties.RowNames =str_emb;
TNM.Properties.VariableNames = column;
Tall.Properties.RowNames =str_emb;
Tall.Properties.VariableNames = column;


% Gives .txt file with the Results for Migrating cells, both Left and right
% sides
FIDout=fopen('ResultsM.txt','w');
writetable(TM,'ResultsM.txt','WriteRowNames',true,'Delimiter','space');
fclose(FIDout);

% Gives .txt file with the Results for Non-Migrating cells, both Left and right
% sides
FIDout=fopen('ResultsNM.txt','w');
writetable(TNM,'ResultsNM.txt','WriteRowNames',true,'Delimiter','space');
fclose(FIDout);
```

```
% Gives .txt file with the Results for All cells (Migrating plus Non-Migrating), both Left and right
% sides
FIDout=fopen('ResultsA.txt','w');
writetable(Tall,'ResultsA.txt','WriteRowNames',true,'Delimiter','space');
fclose(FIDout);
```